On the Riemann-Hilbert approach to the numerical solution of boundary-value problems for evolution partial differential equations

Xin Yang

A dissertation
submitted in partial fulfillment of the
requirements for the degree of

Doctor of Philosophy

University of Washington

2021

Reading Committee:
Bernard Deconinck, Chair
Thomas Trogdon, Chair
Anne Greenbaum
Randall LeVeque

Program Authorized to Offer Degree:
Applied Mathematics

University of Washington

Abstract

On the Riemann-Hilbert approach to the numerical solution of boundary-value problems for evolution partial differential equations

Xin Yang

Co-Chairs of the Supervisory Committee:
Professor Bernard Deconinck
Applied Mathematics

Associate Professor Thomas Trogdon
Applied Mathematics

Integrable systems play an important role in many research areas in Mathematics and Physics. For such systems, the Inverse Scattering Transform provides an alternate way to solve the initial-value problem in terms of Riemann-Hilbert problems. The Riemann-Hilbert approach allows not only a new way for the analysis but also a new way for numerical methods. On the other hand, as an extension of the Inverse Scattering Transform, the Unified Transform Method provides an alternate way to solve initial-boundary-value problems for integrable systems in terms of Riemann-Hilbert problems. In this dissertation, I develop the Numerical Unified Transform Method as a generalization of the Numerical Inverse Scattering Transform. Compared with traditional numerical methods for evolution partial differential equations, methods based on the Riemann-Hilbert approach can give the solution at a given point in the physical domain without time-stepping and can compute the solution with fixed computational costs to reach a given accuracy.

TABLE OF CONTENTS

NOTATION AND ABBREVIATIONS

$\mathbb{C}$: the set of all complex numbers

$\mathbb{C}^{m\times n}$: the set of all m by n complex matrices

$\mathcal{C}_\Gamma$: the Cauchy transform over the contour Γ

C^m_δ: functions that decays exponentially with continuous m-th order derivative on the half-line

$$C^m_\delta = \left\{ f \in C^m([0,\infty)),\ \exists \delta' > \delta > 0,\ \text{such that} \sup_{x\in[0,\infty)} e^{\delta' x} \left| f(x) \right| < \infty \right\}$$

FCM: fixed contour method

I: the identity matrix

IST: Inverse Scattering Transform

IBVP: initial-boundary-value problem

IVP: initial-value problem

KdV: Korteweg-de Vries

mKdV: modified Korteweg-de Vries

LS: linear Schrödinger

NLS: Nonlinear Schrödinger

NIST: Numerical Inverse Scattering Transform

NUTM: Numerical Unified Transform Method

ODE: ordinary differential equation

PDE: partial differential equation

p.v.: principal value

$\mathbb{R}$: the set of all real numbers

RHP: Riemann-Hilbert problem

$\mathbb{S}$: the scattering data

$\mathcal{S}(\mathbb{R})$: Schwartz-class functions on the whole line

$\mathcal{S}(\mathbb{R}^+)$: Schwartz-class functions on the whole line restricted to the half-line

$\mathcal{S}_\delta(\mathbb{R})$: Schwartz-class functions on the whole line with exponential decay

$$\mathcal{S}_\delta(\mathbb{R}) = \left\{ f \in \mathcal{S}(\mathbb{R}) : \exists \delta' > \delta > 0, \text{ such that } |f(x)|\, e^{\delta'|x|} \to 0, \, as \, |x| \to \infty \right\}$$

$\mathcal{S}_\delta(\mathbb{R}^+)$: Schwartz-class functions on the whole line with exponential decay restricted on the half-line

SIE: singular integral equation

SG: sine-Gordon

UTM: Unified Transform Method

$\mathbb{Z}^+$: all positive integers

ACKNOWLEDGMENTS

First of all, I want to thank my supervisory committee for spending their time and efforts on my defense and thesis: Bernard Deconinck, Tom Trogdon, Anne Greenbaum and Randall LeVeque. I would especially like to thank my advisors Bernard and Tom. Their unwavering support and guidance made the completion of this fantastic project possible.

I am proud of being a member of the inspiring research group that Bernard has established at UW. I would like to thank the group members: Chris Swierczewski, Ben Segal, Jeremy Upsal, Ryan Creedon, Jorge Cisneros and Matthew Farkas as well as John Carter and Katie Oliveras from Seattle University for their valuable feedback and discussion during the weekly seminar.

I also want to thank the AMATH department for providing such a supportive environment. Thanks to Lauren, Tony and many other staff members working behind the scenes that I cannot name.

Finally I am grateful to my family for their support. Most importantly, I wish to thank my mom and my wife. Thanks for your affection and care.

DEDICATION

to my dear mom, Lin

and

to my dear wife, Yue

Chapter 1

INTRODUCTION

1.1 Integrability and solitons

For a finite-dimensional autonomous system of dimension N, integrability means that the system has $N-1$ independent conservation laws. A famous example of an integrable system is the two-body problem: two point of masses moving in three-dimensional space under Newton's law of gravitation. On the other hand, the three-body problem does not have a sufficient number of conservation laws and it is not integrable [28].

What we are interested in are infinite-dimensional integrable systems. For an infinite-dimensional system to be integrable, it will need "many" (local) conservation laws. In this dissertation, we consider the following definition of integrability.

Definition 1 (Lax pair and (local complete) integrability [21])**.** *Let X, T be a pair of linear operators that depend on a function $u(x,t)$ and its derivatives as well as on a parameter $z \in \mathbb{C}$. Assume that $u(x,t)$ solves a partial differential equation (PDE) of the form*

$$F(u, u_t, u_{tt}, u_x, u_{xx}, u_{xxx}) = 0, \tag{1.1}$$

where F is a (possibly) nonlinear function. The operators X, T give rise to the linear ordinary differential equations (ODEs),

$$\phi_x = X\phi, \tag{1.2a}$$

$$\phi_t = T\phi. \tag{1.2b}$$

If the compatibility condition of the solution, $\phi_{xt} = \phi_{tx}$, is equivalent to (1.1), then the operators X, T are called a Lax pair associated with the PDE (1.1) and the PDE (1.1) is

(locally and completely) integrable. Alternatively, It is sufficient to have the compatibility condition expressed in terms of the operators X, T by

$$X_t - T_x + XT - TX = 0.$$

This definition covers the examples discussed in this dissertation, including:

- the sine-Gordon (SG) equation in laboratory coordinates: $u_{tt} - u_{xx} + \sin(u) = 0$,
- the Nonlinear Schrödinger (NLS) equation: $iu_t + u_{xx} + 2\lambda |u|^2 u = 0$, and
- linear evolution equations such as: $u_t = u_x + u_{xxx}$.

With appropriate modifications, the definition of integrability extends to many other infinite-dimensional systems [1], for instance:

- PDEs with mixed derivatives: the SG equation in light cone coordinates,

$$u_{xt} - \sin(u) = 0,$$

- nonlocal PDEs: the Benjamin-Ono equation,

$$u_t + 2uu_x + \frac{1}{\pi} \text{ p.v.} \int_{-\infty}^{\infty} \frac{u_{xx}(\tau)}{x - \tau} d\tau = 0,$$

- PDEs of dimension 2×1: the Kadomtsev-Petviashvili equation,

$$(u_t + 6uu_x + u_{xxx})_x \pm 3u_{yy} = 0,$$

- and lattice models: the Toda lattice [12],

$$\begin{cases} \frac{d}{dt} a_n(t) = a_n(t) \left(b_{n+1}(t) - b_n(t) \right), \\ \frac{d}{dt} b_n(t) = 2 \left(a_n(t)^2 - a_{n-1}(t)^2 \right). \end{cases}$$

A consequence of a nonlinear PDE being integrable is that the PDE possesses infinitely many local conservation laws [1]. Nonlinear integrable equations may also have soliton solutions. Loosely speaking, a soliton solution is a localized solution of an integrable equation that is robust with respect to all kinds of disturbances [21]. The study of solitons goes back to the observation and experimental studies by Russell in 1834 [63]. After Zabusky and Kruskal numerically solved the Korteweg-de Vries (KdV) equation and observed interactions between solitons [78] in 1965, the modern study of integrable systems and solitons blossomed. It still draws a lot of interests nowadays.

1.2 Riemann-Hilbert problems

The history of Riemann-Hilbert problems (RHPs) goes back to the 21st problem of the famous Hilbert 23 problems at the International Congress of Mathematicians in 1901 [15]. After a century of development, RHPs are wildly used in many areas of mathematics and physics, for instance, in the fields of orthogonal polynomials and special functions. A comprehensive introduction to RHPs can be found in [73]. The following definitions are used in this dissertation.

Definition 2 (complete and admissible contours)**.** *A union of curves* Γ *in* $\mathbb{C}$ *is said to be a complete and admissible contour if:*

- Γ *consists of a finite number of straight line segments and circles,*
- Γ *does not have tangential self-intersections,*
- *Either* Γ *can be oriented in a way that* $\mathbb{C}\backslash\Gamma$ *can be decomposed into left and right components, i.e.,* $\mathbb{C}\backslash\Gamma = \Omega_+ \cup \Omega_-$, $\Omega_+ \cap \Omega_- = \emptyset$ *and* Ω_+, Ω_- *lie to the left and right of* Γ *respectively, or* Γ *can be augmented so that does, see Augmentation in [73].*

An example of a complete and admissible contour is shown in Figure 1.1.

Definition 3 (Riemann-Hilbert problems)**.** *Given*

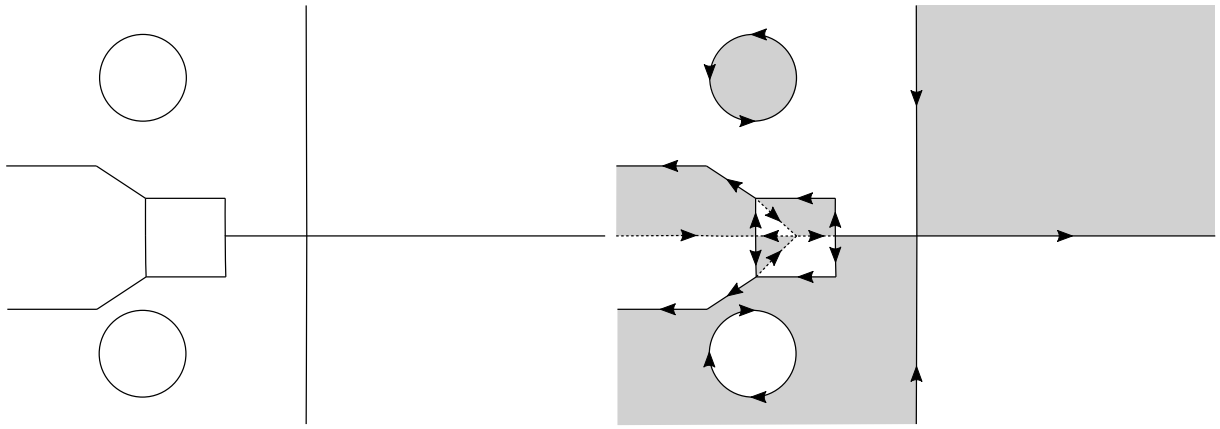

Figure 1.1: Left panel: a complete and admissible contour Γ, Right panel: the associated orientation. The solid curves denote Γ. The dashed curves are auxiliary curves introduced so that the shaded region Ω_+ lies to the left of the augmented contour and the unshaded region Ω_- lies to the right of the augmented contour.

- *an oriented, complete and admissible contour* Γ*,*
- *a multiplicative jump matrix* $G(k) \in \mathbb{C}^{m\times m}$ *and an additive jump matrix* $F(k) \in \mathbb{C}^{m\times m}$ *defined on the contour* Γ*,*
- *a finite set of points* $\{\kappa_j\}_{j=1}^s$ *in* $\mathbb{C}\backslash\Gamma$ *and matrices* $K_j \in \mathbb{C}^{m\times m}$*,* $j = 1, \ldots, s$*,*

a RHP is the problem of finding a sectionally meromorphic function $\Phi : \mathbb{C}\backslash\Gamma \to \mathbb{C}^{m\times m}$ *which is discontinuous across the contour* Γ *with the jump condition*

$$\Phi^+(k) = \Phi^-(k)G(k) + F(k), \quad \text{for } k \in \Gamma, \tag{1.3}$$

where $\Phi^+(k), \Phi^-(k)$ *are the non-tangential limit of* $\Phi(k)$ *from the left* (Ω_+) *and right* (Ω_-) *of* Γ*, respectively. At the points* $\{\kappa_j\}_1^s$*,* Φ *has simple poles with residue conditions*

$$Res_{k=\kappa_j}\Phi(k) = \lim_{k\to\kappa_j} \Phi(k)K_j, \quad j = 1, \ldots, s.$$

Moreover, $\Phi(k) = I + O(1/k)$ *as* $k \to \infty$ *uniformly where* I *is the* $m \times m$ *identity matrix.*

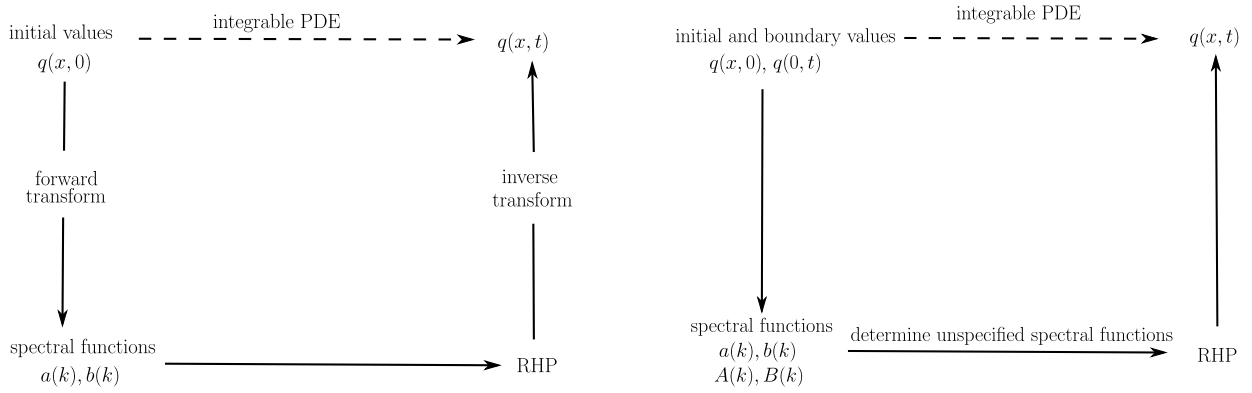

Figure 1.2: A comparison of the schematics of the IST and the UTM for the problems we consider. Panel (a) is the diagram of the solution process for the IST for solving an integrable PDE on the whole line. Panel (b) is the diagram of the solution process for the UTM for solving a linear or nonlinear integrable PDE on the half-line. The inverse problems in both the IST and the UTM are formulated as Riemann-Hilbert problems. Dashed lines denote the evolution via the integrable PDEs under consideration. Solid lines denote the steps of the IST and the UTM that can be accomplished by solving a linear problem.

The RHP is additive if $G = I$, otherwise the RHP is multiplicative. The RHP is called an analytic RHP if there are no residue conditions. The RHP is homogeneous if $F = 0$. An analytic homogeneous RHP is denoted by the pair $[G; \Gamma]$. There is a subtle question: in what sense is (1.3) satisfied? In this dissertation, most examples have jump matrix G that is analytic in a neighborhood of the contour Γ, is square-integrable on Γ and is well-behaved (see [73] for conditions on the well-posedness of RHPs) near the intersections and endpoints of Γ. As a result, classical theory applies and we do not need to worry much about the well-posedness of the problem.

1.3 The Inverse Scattering Transform

One major reason for the extensive studies on integrable equations is that they are exactly solvable by the Inverse Scattering Transform (IST) [1], as stated in [21]: "The inverse scattering method to solve the initial-value problem (IVP) for a given integrable equation

is undoubtedly *the* pinnacle of the theory of integrable systems, and one of the major achievements in nonlinear science." Figure 1.2a illustrates the schematics of the IST. Instead of solving the nonlinear integrable PDE directly, the IST uses the linear Lax pair (1.2a,1.2b). There are three mains steps in the IST:

1. **Forward transform:** Using (1.2a) with the specified initial values at $t = 0$, a set of spectral functions (scattering data) $\{a(k), b(k)\}$ is constructed. These spectral functions are nonlinear versions of the Fourier transforms of the initial values [5].

2. **Time evolution and construction of the RHP:** The benefit of using the spectral functions is that, similar to using the Fourier transform to solve linear constant-coefficient PDEs, the time evolution of the spectral functions can be explicitly determined. With some extra work on the regions of analyticity of the spectral functions, a RHP is constructed with the jump matrix defined in terms of the time-evolved spectral functions. The jump matrix depends on x and t explicitly.

3. **Inverse transform:** The solution to the nonlinear integrable equation is obtained by solving the RHP and considering large k asymptotics. The inverse transform can also be formulated in terms of the Gel'fand-Levitan-Marchenko (GLM) equation [21] but the Riemann-Hilbert approach is more suitable for asymptotics and numerics.

1.4 The Unified Transform Method

In 1997, Fokas developed the Unified Transform Method (UTM) (also known as the Method of Fokas) for nonlinear integrable PDEs on the half-line [31]. The UTM is a generalization of the IST to initial-boundary-value problems (IBVPs). It was immediately observed that the UTM provides a new way to analyze IBVPs of linear PDEs [23, 33]. Figure 1.2b illustrates the schematics of the UTM. The UTM simultaneously performs the spectral analysis of both the x part of the Lax pair (1.2a) and the t part of the Lax pair (1.2b). For linear PDEs, this

is a synthesis as opposed to a separation of variables [40]. There are four mains steps in the UTM:

1. **Forward transform:** Using (1.2a) with the specified initial values at $t = 0$, a set of spectral functions $\{a(k), b(k)\}$ is constructed. Using (1.2b) with the boundary values involved at $x = 0$, a set of spectral functions $\{A(k), B(k)\}$ is constructed. However, the well-posedness of the equation requires only a subset of the boundary values that are required in (1.2b). Computing $\{A(k), B(k)\}$ thus depends on unknown boundary values.

2. **Global relation:** An extra equation, called the global relation, is derived and extensively used in the construction of the RHP in the next step. With some special choice of the boundary conditions, the unknown boundary values can be eliminated by using the global relation. These boundary conditions are called linearizable boundary conditions. All classical boundary conditions for linear (integrable) equations are linearizable.

3. **Construction of the RHP:** With some work on the region of analyticity of the spectral functions, a RHP is constructed where the jump matrix is defined in terms of the spectral functions. The jump matrix depends on x and t explicitly.

4. **Inverse transform:** The solution to the nonlinear integrable equation is obtained by solving the RHP and considering large k asymptotics of the solution of the RHP.

1.5 The development of the Numerical Inverse Scattering Transform and the Numerical Unified transform Method

Many numerical methods have been proposed for integrable evolution equations including finite-difference methods [76], finite-element methods [7], spectral methods [41, 43] and many others (see [77]), but the property of integrability is not heavily used in these methods, if at all. These types of methods are referred to as traditional methods. In general, traditional methods work well and are efficient for small t. As t grows, the increasingly oscillatory nature

of the solution, due to dispersion and multi-scale structures in the solution, accumulation of errors and possible interaction between the solution and artificial boundaries make the problem much more expensive to solve accurately (see Figure 2.2 for a highly-oscillatory solution to the SG equation).

There are other computational approaches that rely on integrability including the Ablowitz-Ladik scheme [65] which is an integrable finite-difference scheme of the original equation, numerical computations of scattering data [14] and numerical computations of the solution to the GLM equation [45].

In 2012, Deconinck, Trogdon and Olver developed a systematic method to make the IST numerically effective for the IVPs of the KdV equation and the modified KdV (mKdV) equation [74]. This method is referred to as the Numerical Inverse Scattering Transform (NIST). The NIST has been successfully applied to integrable systems including the focusing/defocusing NLS equation [72], the Toda lattice [12] and the SG equation [25].

As a hybrid analytical-numerical method, the NIST differs in many aspects from traditional methods and other methods that use integrability. In summary, the NIST has the following features:

1. The method gives the solution at a given (x,t) **without time-stepping or spatial discretization**.

2. The method is **spectrally accurate** in the sense that the error E_{NIST} at fixed (x,t) in the domain satisfies $E_{\text{NIST}}(N,x,t) = o(1/N^l)$ for any integer l, where N is the number of arithmetic operations.

3. The method is **uniformly accurate** in the sense that the computational cost to compute the solution at a point (x,t) with given accuracy remains bounded for large x,t. Moreover, the accuracy is improved in the long-time regime.

4. The method only requires some decay and regularity assumptions on the initial and boundary data. No closed-form expressions for the scattering data are required.

5. The method does not artificially truncate the infinite physical domain.

6. The computations require only the numerical solution of linear problems.

However, the NIST has the following limitations

- The NIST can only be applied to IVPs of integrable PDEs.

- The NIST requires an understanding of the IST and adaptations are required for a particular integrable system.

- It is not efficient to use the NIST if the solution needs to be evaluated at many points (x, t) especially when t is small. But the independence between the evaluation at different points allows for trivial modification for parallel computing to account for this.

Since the UTM generalizes the IST to IBVPs, a natural question to ask is whether we can develop the Numerical Unified Transform Method (NUTM) for IBVPs with all the features that the NIST has. This is our ultimate goal. Before we get to the fully nonlinear scenario, we want to first understand if the NUTM for linear evolution PDEs maintains all the features. In fact, the related studies for linear evolution PDEs started in 2008 [30] before the NIST appeared. The answer for linear problems is positive. We develop a systematic way to apply the NUTM to linear evolution PDEs with all of the above features [26]. On the other hand, extra difficulties appear when the NUTM is applied to nonlinear integrable equations, both in the analysis of the UTM itself and in the associated numerics. As a result, we show that in the example of the focusing/defocusing NLS equation, with a certain type of boundary conditions (the linearizable boundary conditions), the NUTM applied to the half-line problem has all the features [24]. We also show that the NUTM works in additional situations with extra information provided. For instance, the inverse part of the NUTM can be systematically solved once the forward part has been worked out. Finally, we point out

that as the NIST and the NUTM perform well in the regime where traditional methods fail, they provide a benchmark for other, general purpose, numerical methods.

1.6 Organization of the dissertation

In Chapter 2, we apply the NIST to the SG equation on the whole line. In Chapter 3, we apply the NUTM to the heat equation on the half-line, the linear Schrödinger (LS) equation on the half-line and a linearized KdV equation on the half-line. In Chapter 4, we apply the NUTM to the NLS equation on the half-line. In Chapter 5, we summarize our results and discuss related topics for future work.

Chapter 2

THE NUMERICAL INVERSE SCATTERING TRANSFORM FOR THE SINE-GORDON EQUATION

In this chapter, we present the NIST applied to the SG equation in laboratory coordinates on the real line using the method developed by Trogdon, Olver and Deconinck [74].

2.1 The sine-Gordon equation

We consider the SG equation in laboratory coordinates on the real line,

$$u_{tt} - u_{xx} + \sin(u) = 0, \quad x \in \mathbb{R}, \ t \geq 0. \tag{2.1}$$

The SG equation is a nonlinear partial differential equation which appears in differential geometry and various applications such as superconductivity and Josephson junctions [8]. Many numerical methods have been developed to solve the SG equation [44, 51, 64]. Using these methods, or other more traditional but less specialized methods, it is hard to obtain the solution accurately, especially for long time [3, 4], as shown in Figures 2.1, 2.3 and 2.18. In addition, working on an unbounded domain requires special treatment since most traditional methods require domain truncation [79].

Ablowitz, Kaup, Newell and Segur [5] were the first to show that the Cauchy problem for the SG equation written in light-cone coordinates,

$$u_{xt} = \sin(u),$$

is integrable and can be solved by the IST. Kaup [53] demonstrated that (2.1) is solvable by the IST. This is important as (2.1) is the relevant form of the SG equation for most applications.

The NIST makes no domain approximation, does not require time-stepping and is uniformly accurate. As such, it provides a benchmark for other numerical methods [11]. We want to solve (2.1) for $x, t \in \mathbb{R}, t \geq 0$ using the NIST. We assume that the initial values $u(x,0),\ u_t(x,0)$ are continuous and $\sin(u(x,0)),\ u_t(x,0)$ are in $S_\delta(\mathbb{R})$, *i.e.*, Schwartz-class functions on the real line $\mathcal{S}(\mathbb{R})$ with exponential decay: For $\delta > 0$,

$$\mathcal{S}_\delta(\mathbb{R}) = \left\{ f \in \mathcal{S}(\mathbb{R}) : \exists \delta' > \delta > 0, \text{ such that } |f(x)|\, e^{\delta'|x|} \to 0, \, as \, |x| \to \infty \right\}. \tag{2.2}$$

The decay and regularity requirements are mainly for numerical convenience. The global well-posedness theory of the SG equation only assumes initial values in $L^p(\mathbb{R})$ [17].

We illustrate the complex structure and highly oscillatory behaviour of the solution. Let $k_1 = \sqrt{3/5}$, $k_2 = 1$ and define one-soliton solutions:

$$u_1(x,t) := 4 \arctan(\exp((k_1 + 1/k_1) \times x/2 + (k_1 - 1/k_1) \times t/2)), \tag{2.3a}$$

$$u_2(x,t) := 4 \arctan(\exp((k_2 + 1/k_2) \times x/2 + (k_2 - 1/k_2) \times t/2)). \tag{2.3b}$$

Using the auto-Bäcklund transformation discussed in Section 2.5.5, we obtain a two-soliton solution $v(x,t)$,

$$v(x,t) = u_{12}(x,t) = 4 \arctan((k_2 + k_1)/(k_2 - k_1) \times \tan((u_2(x,t) - u_1(x,t))/4)). \tag{2.4}$$

Figure 2.1 shows the numerical solution of (2.1) at $t = 10$ and at $t = 2000$ using the NIST with the initial values in Figure 2.1(a) given by a perturbed two-soliton solution. In Figure 2.1(b), at $t = 10$, the dispersive wave is apparent with an approximate amplitude 0.05 near $x = -10$. At $t = 2000$, the amplitude of the dispersive wave decays to 0.005 and is more oscillatory. Near $x = \pm 2000$ at $t = 2000$, the solution decays exponentially fast to 0, see Figure 2.1(c,d). The uniform accuracy of the NIST guarantees that the numerical solution does not lose accuracy for larger time and in Figure 2.1(e,f) we see that the profiles of the two solitons are preserved. In Figures 2.1 and 2.3, both $\sin(u)$ and u are shown respectively to demonstrate that the oscillations of $\sin(u)$ are not due to large growth of $|u|$.

Remark 1 (nonlinear superposition)**.** *The* 1*-solitons (2.3a) and (2.3b) are moving with speed* $1/4$ *and* 0*, respectively. These speeds are preserved in the* 2*-soliton solution obtained by the auto-Bäcklund transformation. On the other hand, as expected for nonlinear equations, after the perturbation is added, the speeds of the two solitons changes to* 0.33 *and* -0.09*, respectively. A quantitative discuss of the interaction of the solitons and dispersion is in Section 4.3.2 using the NLS equation as an example.*

2.2 The Inverse Scattering Transform for the sine-Gordon equation

Before we construct the NIST for (2.1), we work on the details of the IST for (2.1). Most of the theoretical results are from [17, 19, 53]. For consistency, we present the method using the style and notation of [73]. The SG equation is completely integrable with Lax pair [53]:

$$\psi_x = X(z, u, u_x, u_t)\psi, \tag{2.5a}$$

$$\psi_t = T(z, u, u_x, u_t)\psi, \tag{2.5b}$$

where

$$X(z,u,u_x,u_t) = \begin{pmatrix} -\frac{iz}{4} & 0 \\ 0 & \frac{iz}{4} \end{pmatrix} + \begin{pmatrix} \frac{i\cos(u)}{4z} & \frac{i\sin(u)}{4z} \\ \frac{i\sin(u)}{4z} & -\frac{i\cos(u)}{4z} \end{pmatrix} + \begin{pmatrix} 0 & -\frac{u_x+u_t}{4} \\ \frac{u_x+u_t}{4} & 0 \end{pmatrix},$$

and

$$T(z,u,u_x,u_t) = \begin{pmatrix} -\frac{iz}{4} & 0 \\ 0 & \frac{iz}{4} \end{pmatrix} - \begin{pmatrix} \frac{i\cos(u)}{4z} & \frac{i\sin(u)}{4z} \\ \frac{i\sin(u)}{4z} & -\frac{i\cos(u)}{4z} \end{pmatrix} + \begin{pmatrix} 0 & -\frac{u_x+u_t}{4} \\ \frac{u_x+u_t}{4} & 0 \end{pmatrix}.$$

The existence of a joint matrix solution ψ satisfying both equations (2.5a,b) requires the compatibility condition $\psi_{xt} = \psi_{tx}$, which is an equivalent representation of the SG equation (2.1) [53]. In this new representation, the solution to the SG equation (2.1) can be obtained by solving linear equations. In the IST method, (2.5a) determines the scattering data defined in the following section and (2.5b) determines the time evolution of this scattering data.

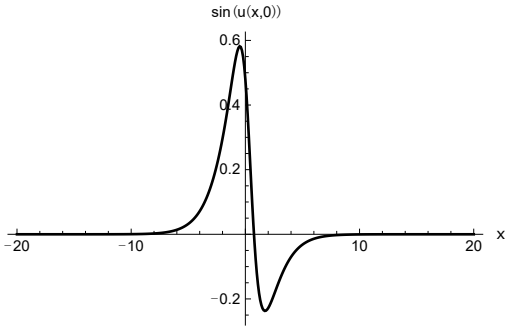

(a) The initial value $\sin(u(x,0))$ is a two-soliton solution with a sech^2 perturbation. The error is on the order of 10^{-10}.

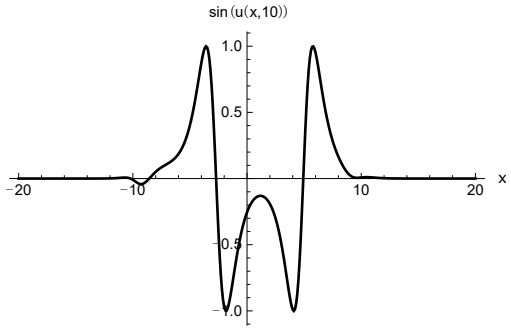

(b) Numerical solution $\sin(u(x,10))$. Two solitons separate from each other. Dispersive effects starts to appear near $x = -10$.

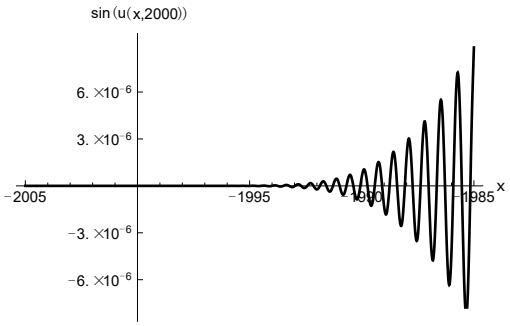

(c) The exponentially growing oscillatory solution near $x = -2000$ at $t = 2000$.

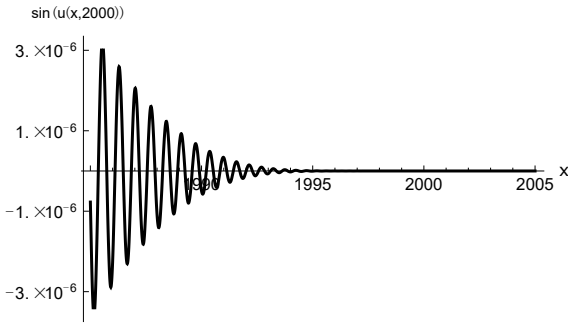

(d) The exponentially decaying oscillatory solution near $x = 2000$ at $t = 2000$.

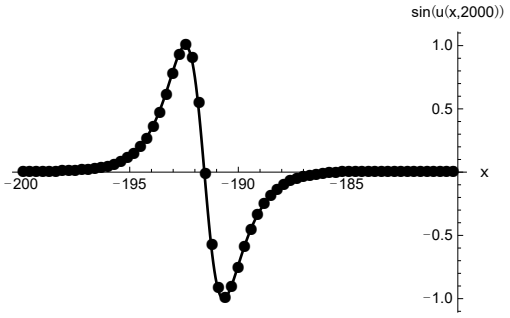

(e) The soliton near $x = -190$ at $t = 2000$. (Dots) numerical solution, and (Solid) shifted unperturbed exact solution.

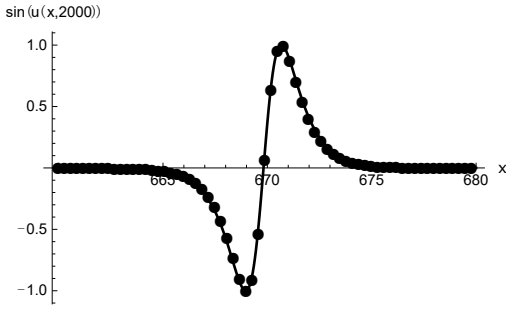

(f) The soliton near $x = 670$ at $t = 2000$. (Dots) numerical solution, and (Solid) shifted unperturbed exact solution.

Figure 2.1: The numerical solution $\sin(u(x,t))$ of (2.1). The initial value is $u(x,0) = v(x,0) + 0.5\text{sech}^2(x)$, $u_t(x,0) = v_t(x,0)$. The two-soliton solution $v(x,t)$ defined by Equation (2.4) is generated by the consistency condition (2.31) using two one-soliton solutions (2.32) with $k_1 = \sqrt{3/5}$, $k_2 = 1$ and a zero solution.

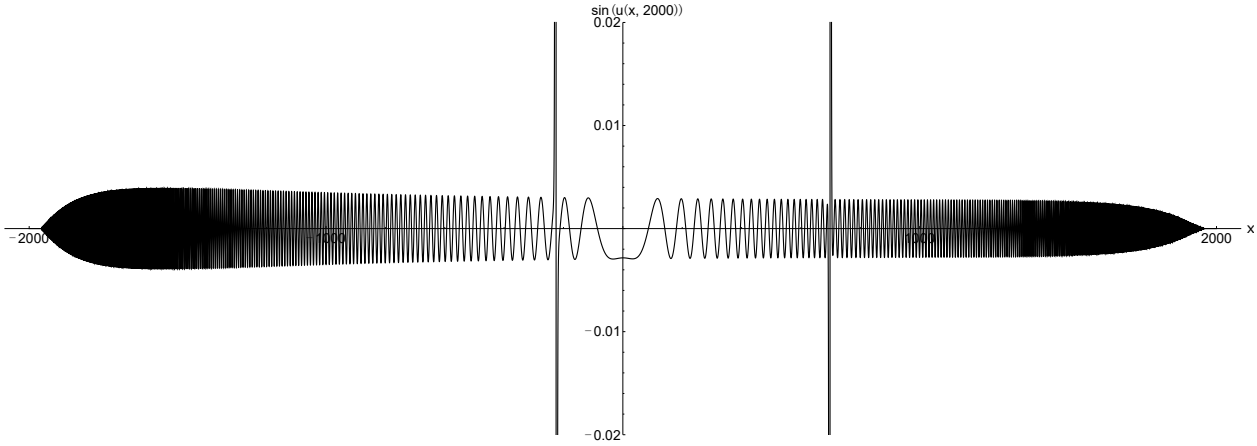

Figure 2.2: The numerical solution $\sin(u(x, 2000))$ for x from -2000 to 2000. The two spikes are the solitons with amplitude 1 while the amplitude of the dispersive waves is about 0.005.

2.2.1 Forward scattering

The process of finding the scattering data from (2.5a) is called forward scattering. Because of the compatibility condition, (2.5a) can be solved at any value of the parameter t. To obtain the scattering data, we define two matrix solutions to (2.5a) by their corresponding asymptotic behavior.

$$\psi^-(x,t,z) \sim \begin{pmatrix} e^{-ix(z-1/z)/4} & 0 \\ 0 & -e^{ix(z-1/z)/4} \end{pmatrix}, \text{ as } x \to -\infty,$$

$$\psi^+(x,t,z) \sim \begin{pmatrix} e^{-ix(z-1/z)/4} & 0 \\ 0 & e^{ix(z-1/z)/4} \end{pmatrix}, \text{ as } x \to \infty.$$

Since these two solutions are linearly dependent, there exists a scattering matrix $S(z,t)$, independent of x, relating $\psi^-(x,t,z)$ and $\psi^+(x,t,z)$:

$$\psi^+(x,t,z) = \psi^-(x,t,z)S(z,t). \tag{2.6}$$

The matrix $S(z,t)$ plays the role of the Fourier transform in linear problems [5, 53] and can be used to recover the function $u(x,t)$ by inverse scattering. In practice, different forms of

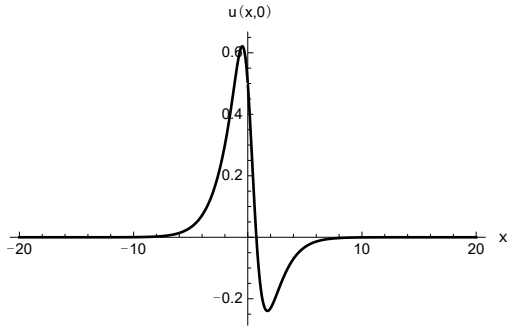

(a) The initial value $u(x,0)$ is a two-soliton solution with a sech^2 perturbation. The error is on the order of 10^{-10}.

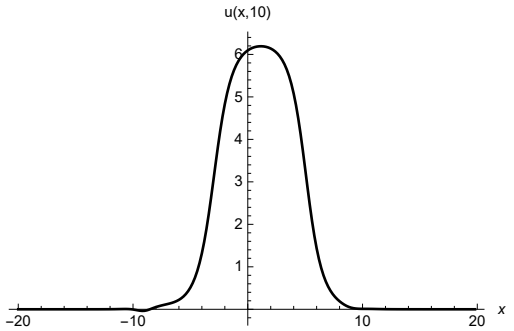

(b) The numerical solution $u(x,10)$. Two solitons separate from each other. Dispersive effects starts to appear near $x = -10$.

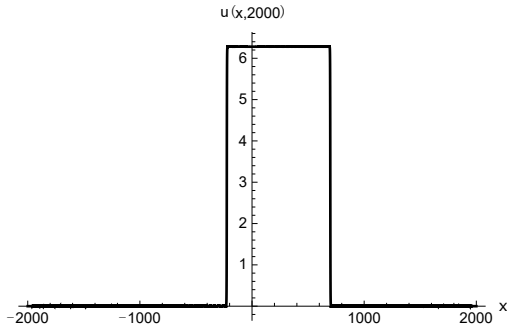

(c) The numerical solution $u(x,2000)$ for x from -2000 to 2000. The amplitude of the dispersive waves is on the order of 0.005.

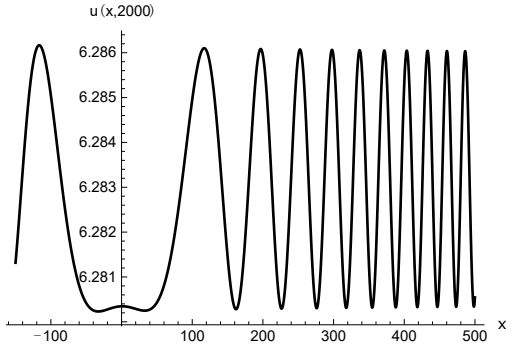

(d) The dispersive waves between the two solitons.

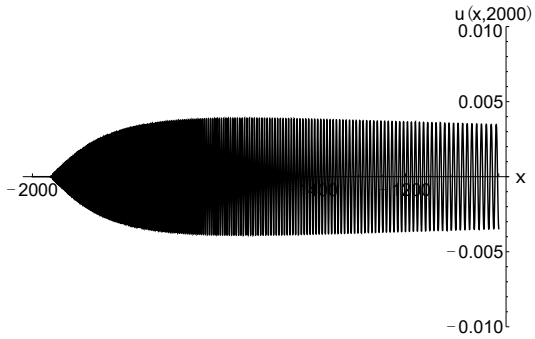

(e) The dispersive waves in $x \in (-2000, -1000)$ at $t = 2000$.

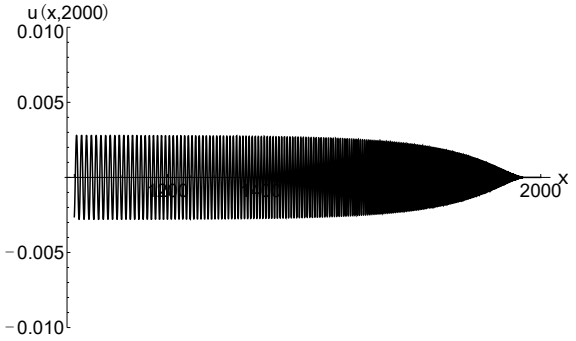

(f) The dispersive waves in $x \in (1000, 2000)$ at $t = 2000$.

Figure 2.3: The numerical solution $u(x,t)$ of (2.1). The initial values are the same as in Figure 2.1. This demonstrates that the high oscillations are not due to a rapidly growing argument of sine but are inherent to the solution itself.

the scattering matrix are used. Let

$$S(z,t) = \begin{pmatrix} a(z,t) & B(z,t) \\ b(z,t) & A(z,t) \end{pmatrix},$$

which for real initial values has the symmetry [53],

$$a(z,t) = -\overline{A(\bar{z},t)}, \quad b(z,t) = \overline{B(\bar{z},t)}, \tag{2.7}$$

and

$$a(z,t) = -A(-z,t), \quad b(z,t) = B(-z,t). \tag{2.8}$$

Moreover, with the Schwartz-class initial values, $a(z,t)$ is analytic in the upper-half z-plane and $a(z,t)$, $b(z,t)$ are bounded on the real z-axis [53]. For sufficiently large $|z|$, $a(z,t)$ is bounded away from zero [73]. The exponential decay of the initial values in $S_\delta(\mathbb{R})$ allows $a(z,t)$ and $b(z,t)$ to be analytically extended to regions defined by $\mathcal{D}_\delta := \{|\mathrm{Re}(i(z-1/z)/4)| < \delta/2\}$ which looks like a strip pinched at the origin. The boundary of $\mathcal{D}_\delta$ in the first quadrant of the complex $z-$plane is a level set of $|\mathrm{Re}(i(z-1/z)/4)|$ shown in Figure 2.5 and is symmetric with respect to the real and imaginary axes. For some $u(x,0)$ and $u_t(x,0)$, there may exists values $z = \kappa_j$, $\mathrm{Im}(\kappa_j) > 0$ such that $a(\kappa_j,0) = 0$. These correspond to bound states. The number of bound states is finite for initial values in S_δ. As in [19, 53], we assume that the zeros are simple and not real. This is guaranteed in the case of compactly supported initial values, is true in many other cases [17, 47] and in all the numerical examples we have computed. (For instance, we get non-simple or real zeros of $a(z)$ if $(\gamma(\mu)-1)/2\epsilon \in \mathbb{Z}^+$ in (2.20) [17]).

Define the reflection coefficient

$$\rho(z,t) := \frac{b(z,t)}{a(z,t)}.$$

For $z \in \mathbb{R}$, and fixed t, $\rho(z,t) \in \mathcal{S}(\mathbb{R})$ is a Schwartz-class function and therefore $|\rho(z,t)| \to 0$ faster than any power of z as $|z| \to 0$ [19]. It is important to note that $b(z,t)$ is only defined on the real line and may or may not have an analytic continuation off the real axis.

However, $b(\kappa_j, t)$ is defined at the zeros of $a(z, t)$ in the upper-half z-plane as a proportionality coefficient determined by solving (2.6) directly [73]. For instance, we can have $b(z, t) = 0$ for real z but $b(\kappa_j, t) \neq 0$ which is the corresponding scattering data for a pure soliton solution. With exponentially decaying initial values, $\rho(z, t)$ is guaranteed to have an analytic continuation near the real z-axis except at $z = 0$ and $z = \infty$. Moreover, if the initial values are compactly supported, $a(z, t)$ and $b(z, t)$ are analytic everywhere except at $z = 0$ and $z = \infty$ [53]. At the zeros of $a(z, t)$, $b(\kappa_j, t)$ is the proportionality constant between two fundamental solutions that are exponentially decaying in different directions,

$$\psi_2^+(x, t, \kappa_j) = \psi_1^-(x, t, \kappa_j) b(\kappa_j, t), \tag{2.9}$$

where subscripts refer to columns. This implies that $\psi_2^+(x, t, \kappa_j), \psi_1^-(x, t, \kappa_j)$ are eigenfunctions of the Lax operator in (2.5a). For these values of z, considering only simple zeros, the norming constants are defined as

$$C_j(t) = \frac{b(\kappa_j, t)}{a'(\kappa_j, t)}.$$

The collection

$$\mathbb{S} = \{\rho(z, t), \{(\kappa_j, C_j(t))\}_{j=1}^n\},$$

defines the scattering data.

2.2.2 Time evolution of the scattering data

The scattering data $\mathbb{S}$ has simple time dynamics. It is independent of x and its t dependence is explicit. If we choose $x \to \infty$, (2.5b) is diagonalized with constant coefficients depending only on z. Therefore we can write down the time evolution of the scattering data by plugging (2.5b) into (2.6), leading to

$$a(z, t) = a(z, 0), \tag{2.10a}$$

$$b(z, t) = \exp\left(\frac{it}{2}\left(z + \frac{1}{z}\right)\right) b(z, 0). \tag{2.10b}$$

It follows that $\{\kappa_j\}$, the zeros of $a(z,t)$, are fixed as time evolves which is an essential component of IST theory. For convenience we suppress the time dependence in a, b and ρ if $t = 0$.

2.2.3 Inverse scattering

The process of recovering the solution to the SG equation (2.1) from the scattering data $\mathbb{S}$ is called inverse scattering. We shall perform inverse scattering using Riemann-Hilbert problems (RHPs) [73]. Let

$$m(x,t,z) = \psi(x,t,z) \begin{pmatrix} e^{ix(z-1/z)/4} & 0 \\ 0 & e^{-ix(z-1/z)/4} \end{pmatrix}.$$

Then $m(x,t,z)$ satisfies the ordinary differential equation

$$m_x(x,t,z) = [J(z), m(x,t,z)] + Q(x,t,z)m(x,t,z), \tag{2.11}$$

where

$$J(z) = -\frac{i}{4}\left(z - \frac{1}{z}\right) \begin{pmatrix} 1 & 0 \\ 0 & -1 \end{pmatrix}, \tag{2.12}$$

$$Q(x,t,z) = \begin{pmatrix} \frac{i}{4z}(\cos(u(x,t)) - 1) & \frac{i}{4z}\sin(u(x,t)) - \frac{1}{4}(u_x(x,t) + u_t(x,t)) \\ \frac{i}{4z}\sin(u(x,t)) + \frac{1}{4}(u_x(x,t) + u_t(x,t)) & -\frac{i}{4z}(\cos(u(x,t)) - 1) \end{pmatrix}, \tag{2.13}$$

and $[\cdot,\cdot]$ is the matrix commutator. Let $m^+ = (m_1^+, m_2^+)$ and $m^- = (m_1^-, m_2^-)$ be the solutions corresponding to ψ^+ and ψ^-. They satisfy the asymptotic conditions

$$\lim_{x\to\infty} m^+(x,t,z) = \begin{pmatrix} 1 & 0 \\ 0 & 1 \end{pmatrix}, \lim_{x\to-\infty} m^-(x,t,z) = \begin{pmatrix} 1 & 0 \\ 0 & -1 \end{pmatrix}.$$

Two new matrices $\hat{\Phi}^+$ and $\hat{\Phi}^-$ are defined by rearranging columns of m^+ and m^-,

$$\hat{\Phi}^+(z,x,t) = (m_1^-(x,t,z), m_2^+(x,t,z)),$$

$$\hat{\Phi}^-(z,x,t) = (m_1^+(x,t,z), m_2^-(x,t,z)).$$

Let

$$\Phi^+(z,x,t) = \hat{\Phi}^+(z,x,t) \begin{pmatrix} 1/a(z,t) & 0 \\ 0 & 1 \end{pmatrix},$$

$$\Phi^-(z,x,t) = \hat{\Phi}^-(z,x,t) \begin{pmatrix} 1 & 0 \\ 0 & -1/\overline{a(\bar{z},t)} \end{pmatrix}.$$

It has been shown that Φ^+ can be analytically continued to the upper-half z-plane, while Φ^- can be analytically continued to the lower-half z- plane if u_x, u_t and $\sin(u/2)$ are integrable [53], which is true if $\sin(u(x,0))$ and $u_t(x,0)$ are continuous and in $\mathcal{S}_\delta(\mathbb{R})$. Therefore for $z \in \mathbb{R}$, there is a jump condition,

$$\Phi^+(z,x,t) = \Phi^-(z,x,t)G(z,x,t).$$

Given the jump function $G(z,x,t)$ on the contour (the real line), the problem of finding Φ^+ analytic in the upper-half z-plane and Φ^- analytic in the lower-half z-plane is an (analytic) RHP. The contour is assigned orientation and we use Φ^+ to denote the non-tangential pointwise limit from the left of the contour and Φ^- for the limit from the right of the contour. After incorporating the zeros of $a(z)$, we arrive at the following (meromorphic) RHP [19].

Theorem 1. *With the previous definitions of variables, assume that sine of the initial values of (2.1),* $\sin(u(x,0))$ *and* $\sin(u_t(x,0))$*, are in the space* $S_\delta(\mathbb{R})$*. Assume that* $a(z)$ *has only simple zeros in the open upper-half z-plane. Then there exists a unique function* $\Phi(z,x,t)$*,* $x,t \in \mathbb{R}$*,* $z \in \mathbb{C}\backslash\mathbb{R}$ *continuous up to the real axis satisfying the jump condition:*

$$\Phi^+(z,x,t) = \Phi^-(z,x,t)G(z,x,t), \quad z \in \mathbb{R}. \tag{2.14}$$

The jump matrix $G(z,x,t)$ *is defined by*

$$G(z,x,t) := \begin{pmatrix} 1+\rho(z)\overline{\rho(\bar{z})} & \overline{\rho(\bar{z})}e^{-\theta(z,x,t)} \\ \rho(z)e^{\theta(z,x,t)} & 1 \end{pmatrix}, \tag{2.15}$$

where $\rho(z)$ is the reflection coefficient and

$$\theta(z,x,t) = \frac{i}{2}\left[\left(z-\frac{1}{z}\right)x + \left(z+\frac{1}{z}\right)t\right].$$

Moreover, Φ satisfies the asymptotic condition,

$$\lim_{z\to\infty}\Phi(z,x,t) = \begin{pmatrix} 1 & 0 \\ 0 & 1 \end{pmatrix},$$

and the residue conditions at the zeros $\kappa_1, \kappa_2, \ldots, \kappa_N$ of $a(z)$ in the upper-half $z-$plane,

$$Res\{\Phi(z,x,t), z=\kappa_j\} = \lim_{z\to k_j}\Phi(z,x,t)\begin{pmatrix} 0 & 0 \\ C_j e^{\theta(\kappa_j,x,t)} & 0 \end{pmatrix},$$

$$Res\{\Phi(z,x,t), z=\overline{\kappa_j}\} = \lim_{z\to \overline{k_j}}\Phi(z,x,t)\begin{pmatrix} 0 & -\overline{C_j}e^{-\theta(\overline{\kappa_j},x,t)} \\ 0 & 0 \end{pmatrix}.$$

The solution Φ is meromorphic in the upper-half and lower-half z-plane with its pointwise limit functions on the real line Φ^+ from above and Φ^- from below that are both continuous. The corresponding solution to (2.1) is given by

$$\begin{pmatrix} \cos(u(x,t)) & \sin(u(x,t)) \\ \sin(u(x,t)) & -\cos(u(x,t)) \end{pmatrix} = \Phi(0,x,t)\begin{pmatrix} 1 & 0 \\ 0 & -1 \end{pmatrix}\Phi(0,x,t)^{-1}. \tag{2.16}$$

For the proof of Theorem 1, the reader is referred to Theorem 2,3 in [19] and [10, 80]. It should be mentioned that (2.16) is well defined because the reflection coefficient vanishes at $z=0$ implying $\Phi^+(0) = \Phi^-(0)$. In practice (see the next section), the residue conditions are replaced by jump conditions on small circles centered at each pole κ_j [74, 72].

2.3 Numerical forward scattering

2.3.1 Computing the reflection coefficient

In order to obtain the scattering data from the initial values, we need to solve (2.11) for given values of z. Let

$$I = \begin{pmatrix} 1 & 0 \\ 0 & 1 \end{pmatrix}, \quad \sigma_3 = \begin{pmatrix} 1 & 0 \\ 0 & -1 \end{pmatrix}.$$

Define

$$N^+(x,z) = m^+(x,z) - I,$$

and

$$N^-(x,z) = m^-(x,z) - \sigma_3.$$

Then (2.11) becomes

$$N_x^+ - [J, N^+] - QN^+ = Q, \tag{2.17}$$

on $[0,\infty)$ with $N^+(\infty) = 0$ and

$$N_x^- - [J, N^-] - QN^- = Q\sigma_3, \tag{2.18}$$

on $(-\infty, 0]$ with $N^-(-\infty) = 0$. The two equations (2.17-2.18) are solved column by column using a Chebyshev collocation method [9]. Equation (2.17) is solved on $[0, L]$ with a vanishing boundary condition at $x = L$ for sufficiently large L such that the initial values of (2.1) are smaller than the given tolerance. Similarly, (2.18) is solved on $[-L, 0]$ with a vanishing boundary condition at $x = -L$. With the computed solution, the scattering matrix is given by (2.6):

$$S(z) = (N^+(0,z) + I)(N^-(0,z) + \sigma_3)^{-1}.$$

To verify the spectral accuracy of the method, we test it with a known closed-form expression for the reflection coefficient [17]. Consider the initial values

$$u(x,0) = 2\arccos(\tanh(\epsilon x)),\ u_t(x,0) = 2\,\mu\,\mathrm{sech}(\epsilon x), \tag{2.19}$$

where ϵ, μ are real parameters. With proper scaling, these initial values generate solutions to the SG equation in the semiclassical limit as $\epsilon \to 0$. The reflection coefficient $\rho(z)$ is

$$\rho(z) = -\frac{z + (\gamma+\mu)i}{z - (\gamma+\mu)i}\,\frac{\Gamma\left(\frac{1}{2} + \frac{iE}{\epsilon}\right)\Gamma\left(1 - \frac{\gamma}{2\epsilon} - \frac{iE}{\epsilon}\right)\Gamma\left(\frac{\gamma}{2\epsilon} - \frac{iE}{\epsilon}\right)}{\Gamma\left(\frac{1}{2} - \frac{\gamma}{2\epsilon}\right)\Gamma\left(\frac{1}{2} + \frac{\gamma}{2\epsilon}\right)\Gamma\left(\frac{1}{2} - \frac{iE}{\epsilon}\right)}, \tag{2.20}$$

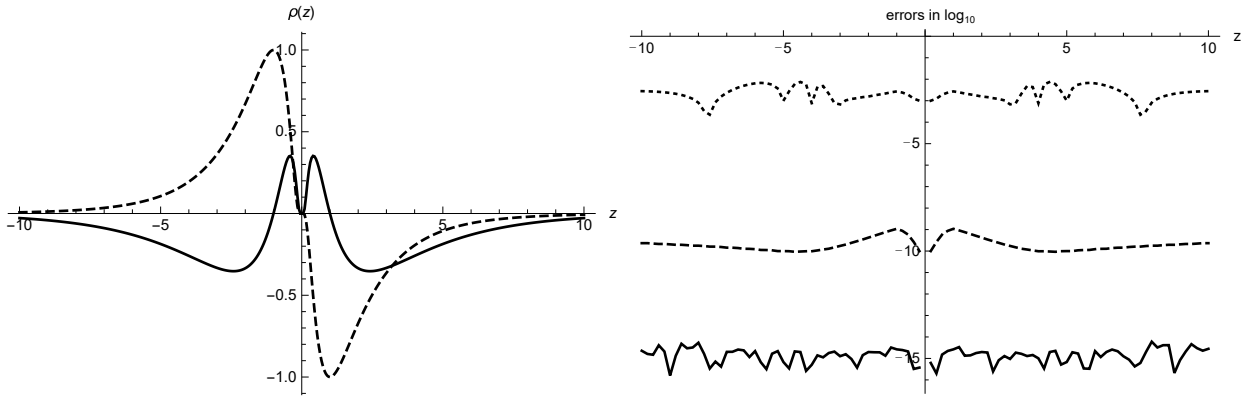

Figure 2.4: (Left) The exact reflection coefficient $\rho(z)$, $z \in [-10, 10]$ given by Equation (2.20) with $\mu = 0$, $n = 0$, $\epsilon = 2$. Solid: real part. Dashed: imaginary part. (Right) The plot of log of the absolute error for $z \in [-10, 10]$. Dotted: 20 collocation points. Dashed: 70 collocation points. Solid: 120 collocation points.

where $E = (z - 1/z)/4$, $\gamma = \sqrt{1 + \mu^2}$. $\Gamma(z)$ is the Gamma function. If $\epsilon = \gamma/(2n + 1)$ where n is a non-negative integer, then $\rho(z) \equiv 0$. We choose $\mu = 0$, $n = 0$, $\epsilon = 2$ to have $\gamma/(2n+1) = 1 \neq \epsilon$ so that $\rho(z)$ does not vanish. Figure 2.4 shows the numerically computed reflection coefficient on the interval $[-10, 10]$ and the spectral decay of the absolute error with respect to the number of collocation points used. The evaluation of the reflection coefficient off the real line is more difficult since $b(z, t)$ is only guaranteed to have analytic extension in $\mathcal{D}_\delta$. Figure 2.5 shows the condition number K when the linear system is solved using a Chebyshev collocation method in the region $0 \leq \mathrm{Re}(z), \mathrm{Im}(z) \leq 1$. The condition number grows quickly when z moves away from the real axis to the boundary of $\mathcal{D}_\delta$. Since the coefficient of the linear term contains $i(z - 1/z)/4$ in (2.17,2.18), the condition number K is also related to $|\mathrm{Re}(i(z - 1/z)/4)|$. On the other hand, with finitely many collocation points, there exists a narrow band near the origin where the condition number is moderate. The region with high condition number needs to be avoided and this determines the deformation of the contour near the origin, to be discussed in Section 4. The computation of the reflection coefficient near the origin can be improved by introducing a new system for $w(x, z)$, called

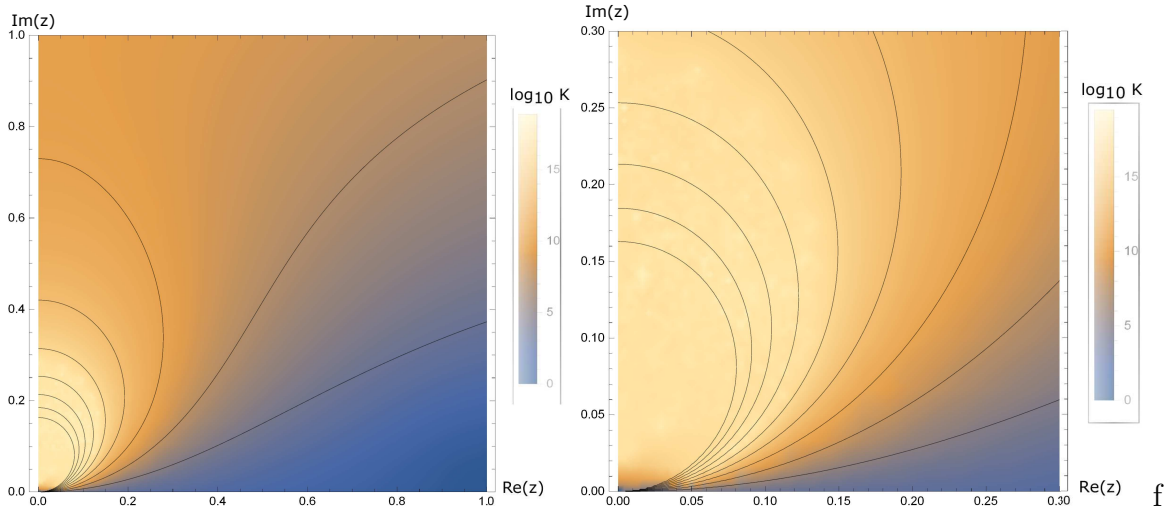

Figure 2.5: The condition number K (in $\log_{10}$ scale) for the linear system computing $\rho(z)$ given by Equation (2.20) with $\mu = 0$, $n = 0$, $\epsilon = 2$ using a Chebyshev collocation method with 120 collocation points for $0 \leq \mathrm{Re}(z), \mathrm{Im}(z) \leq 1$ (left) and for $0 \leq \mathrm{Re}(z), \mathrm{Im}(z) \leq 0.3$ (right). The contour lines are the level sets of $|\mathrm{Re}(i(z - 1/z)/4)|$. These level sets match the condition number except in a small neighbourhood of the origin where the condition number is moderate, i.e., the dark colors extend to the origin in the right panel. In this small neighbourhood we can use straight lines with nonzero slope for the deformations in Section 2.4.

the zero gauge system [17, 53], with the transformation

$$w(x,t,z) = i \begin{pmatrix} \cos(u/2) & \sin(u/2) \\ -\sin(u/2) & \cos(u/2) \end{pmatrix} m(x,t,z).$$

The name zero gauge system comes from the fact that under this transformation the $1/z$ term in (2.13) becomes order z, and the original system is referred to as infinite gauge. We use the zero gauge to solve for the reflection coefficient for $|z| \leq 1$ and the infinite gauge otherwise. On the other hand, since the reflection coefficient $\rho(z)$ has symmetry (2.7) and (2.8), we only need to compute the values of $\rho(z)$ in the upper-half $z-$plane.

2.3.2 Computing the zeros of $a(z)$

The zeros of $a(z)$ correspond to the bound states, which are square integrable solutions of (2.5a). In the KdV equation and the NLS equation, the bound states are obtained by analyzing the discrete spectrum of the Lax operator X. Finding the bound states for the SG equation, however, leads to a quadratic eigenvalue problem. It can be written as a standard eigenvalue problem by considering a system of twice the dimension [66],

$$\begin{pmatrix} 4i\partial_x & i(u_x+u_t) & \cos u & \sin u \\ i(u_x+u_t) & -4i\partial_x & -\sin u & \cos u \\ 1 & 0 & 0 & 0 \\ 0 & 1 & 0 & 0 \end{pmatrix} \begin{pmatrix} \Omega_1 \\ \Omega_2 \end{pmatrix} = z \begin{pmatrix} \Omega_1 \\ \Omega_2 \end{pmatrix}. \tag{2.21}$$

In this case, $\Omega_2 = \psi$ and $\Omega_1 = z\Omega_2$ are two vectors of size 2×1. After a change of variable $x \mapsto \tan(s/2)$, Floquet-Fourier-Hill method is applied to compute the eigenvalues of the operator with spectral accuracy [22]. We test the accuracy with the initial values in (2.19). For general initial values where the eigenvalues are not known, we can check if all the eigenvalues are captured by comparing the reconstructed solution from inverse scattering with the given initial values. Let $n = 4$, $\mu = 1$, $\gamma = \sqrt{1+\mu^2} = \sqrt{2}$, $\epsilon = \gamma/(2n+1) = \sqrt{2}/9$ in (2.19). With this form of the initial values, the eigenvalues in the upper half of the complex

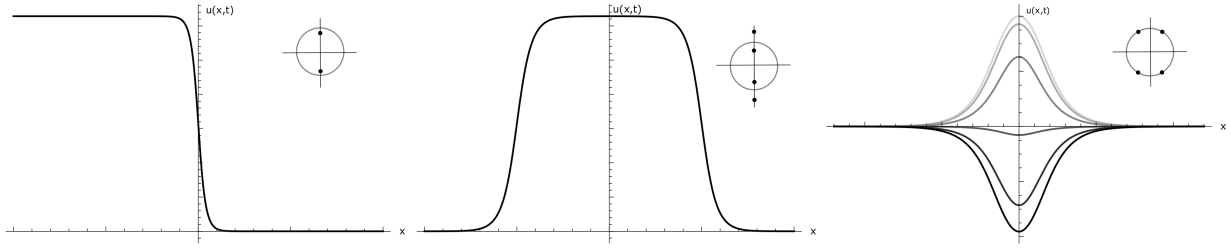

Figure 2.6: Examples of the three types of soliton solutions $u(x,t)$: (Left) An antikink solution. (Middle) A kink-antikink pair solution. (Right) A sitting breather solution oscillating from upward to downward with profiles in grayscale. The location of the corresponding eigenvalues in the complex $z-$plane is shown in the upper-right corner of each plot.

z-plane are classified into three types by the shape of the soliton solutions shown in Figure 2.6:

1. Antikink: $z = \pm\left(\gamma(\mu) - \mu\right) i$, a single eigenvalue on the positive imaginary axis with its symmetric counterpart on the negative imaginary axis.

2. Kink-antikink pair: $z = \pm i \exp\left(\pm \text{arccosh}\left(\gamma(\mu) - 2p\epsilon\right)\right)$ with $p \in \mathbb{Z}^+$ such that $1 \leq p \leq (\gamma(\mu) - 1)/2\epsilon$, a pair of eigenvalues on the positive imaginary axis with one inside and the other outside the unit circle. Two symmetric eigenvalues are on the negative imaginary axis.

3. Breather: $z = \pm \exp(i(\pi/2 \pm (\pi/2 - \arcsin(\gamma(\mu - 2p\epsilon))))$ with $p \in \mathbb{Z}^+$ such that $(\gamma(\mu) - 1)/2\epsilon < n \leq \gamma(\mu)/2\epsilon$, four points on the unit circle that are symmetric with respect to both the real and imaginary axis.

Figure 2.7 shows the distribution of the eigenvalues in the upper-half z-plane and the spectral convergence of the difference between the numerical results using Hill's method and the zeros of the known formula (2.20).

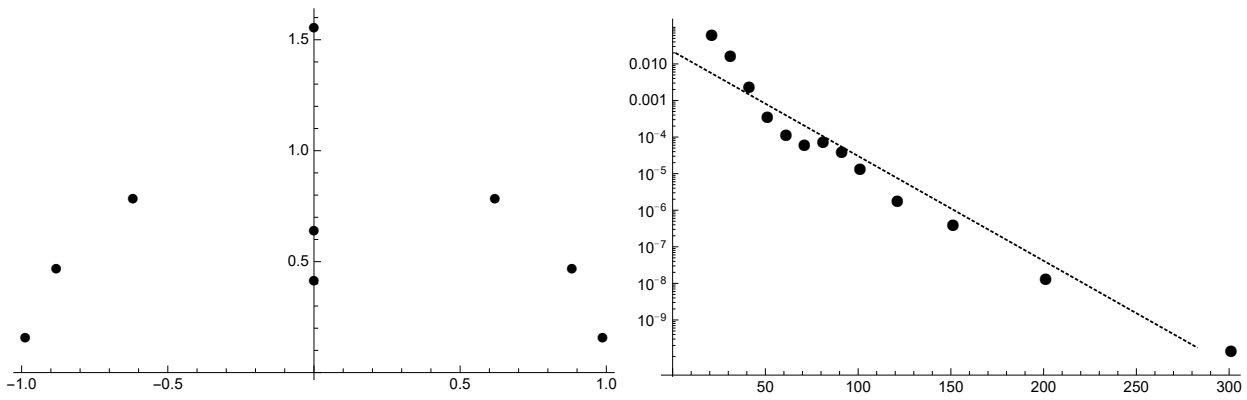

Figure 2.7: (Left) Location of the eigenvalues in the upper-half z-plane. The set consists of 1 antikink, 1 kink-antikink pair and 3 breathers. (Right) The maximum error y versus the number of collocation points x. The dashed line is a reference straight line. Initial values are given by Equation (2.19) with $n = 4$, $\mu = 1$, $\gamma = \sqrt{1+\mu^2} = \sqrt{2}$, $\epsilon = \gamma/(2n+1) = \sqrt{2}/9$.

2.4 Numerical inverse scattering

We solve the RHP (2.14) with complex variable z numerically with x, t as parameters. Once the jump matrix can be computed, the packages *RHPackage* [58] by Olver and *ISTPackage* [68] by Trogdon are used to solve (2.14). The idea of the methodology in the packages is that for an RHP denoted by $[G;\Gamma]$, where G is the jump matrix, $\Phi^+ = \Phi^- G$, defined on the contour Γ, we seek a representation of the solution Φ as

$$\Phi = I + \mathcal{C}_\Gamma q(z), \tag{2.22}$$

for $q \in L^2(\Gamma)$. Here

$$\mathcal{C}_\Gamma q(z) = \frac{1}{2\pi i}\int_\Gamma \frac{q(s)}{z-s} ds,$$

is the Cauchy transform of $q(z)$. The Plemelj formula states that $\Phi^+ - \Phi^- = q$ [2]. Therefore we obtain the singular integral equation (SIE),

$$q(s) - \mathcal{C}_\Gamma^- q(s)(G(s) - I) = G(s) - I, \ \ s \in \Gamma,$$

where $\mathcal{C}_\Gamma^- q(s)$ denotes the non-tangential pointwise limit from the right of the contour Γ. We solve the RHP by solving the SIE using the Chebyshev collocation method of Olver [59].

However, many modifications are required in order to obtain a feasible implementation. As one can see, for general x and t, the jump matrix can be highly oscillatory due to the exponential factor in the jump matrix of the RHP (2.14), $\theta(z,x,t) = \frac{i}{2}[(z-1/z)x+(z+1/z)t]$. Therefore a large number of collocation points is required to resolve the solution of the RHP. The method of nonlinear steepest descent by Deift and Zhou [27] provides a solution to this problem by deforming the contour in such a way that the oscillations are turned into exponential decay near the saddle points $\theta'(z_0) = 0$. The deformations are different for different regions of the (x,t)-plane. For the SG equation, there are four asymptotic regions showing in Figure 2.8:

1. Region 1: Outside the light cone, characterized by $x \geq t$,
2. Region 2: Outside the light cone, characterized by $x \leq -t$,
3. Region 3: Inside the light cone, characterized by $|x| < t$,
4. Region 4: Transition, inside region 3 characterized by $t(t-x) \leq 1$.

After proper deformation of the contours, the jump matrices are exponentially decaying away from the saddle points. Therefore we can truncate the contour if the jump matrix is sufficiently close to the identity matrix, within a given tolerance. In the case of large-parameter asymptotics, the contour becomes localized and the truncation makes the computations more efficient as the parameter increases.

Remark 2. *One may expect the deformations in Figure 2.8 to be symmetric with respect to $x = 0$ since the SG equation (2.1) is invariant under the transformation $x \to -x$. The asymmetry can be explained in two ways. One reason is that the Lax pair (2.5a) is not symmetric under $x \to -x$. The other reason is that the scattering matrix (2.6) can be interpreted as outputs from sending waves in from $x = -\infty$. If one chooses to define the scattering matrix $\tilde{S}$ by*

$$\psi^+(x,t,z)\tilde{S}(z,t) = \psi^-(x,t,z), \tag{2.23}$$

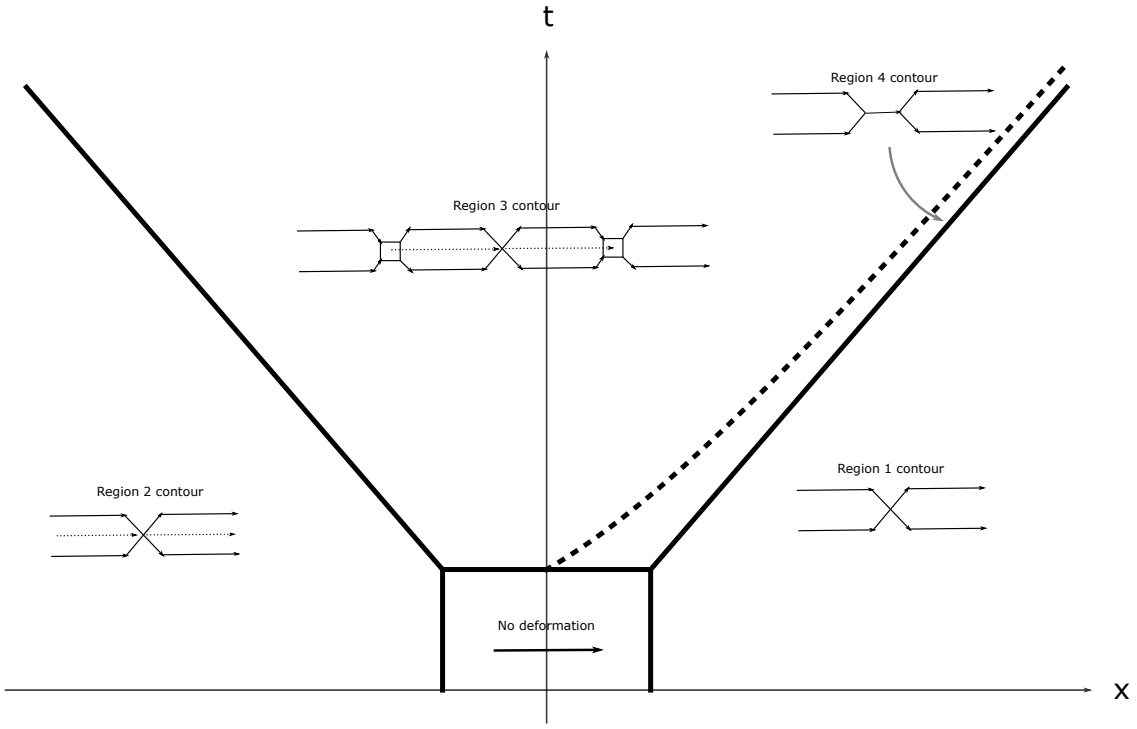

Figure 2.8: Asymptotic regions of the (x, t)-plane for the SG equation and the corresponding contour deformation for the IST. Away from the origin, the deformations are restricted in the interior of $\mathcal{D}_\delta$. Near the origin, the jump matrix converges to the identity matrix exponentially which allows us to use straight lines for the jump contour other than curves tangent to the real axis.

then the sign in the exponent in the jump matrix changes. As a result, the deformations in Region 1 and Region 2 are swapped and the deformations in Region 3 and Region 4 will be changed owing to the matrix factorization (2.24) and (2.26). We can improve the efficiency of the NIST by eliminating the Region 2 deformation, as discussed in Section 2.4.3. The machinery of the NIST does not require symmetry in the integrable equation, see the case of the KdV equation [74].

2.4.1 Region 1: Outside the light cone, characterized by $x \geq t$

This is the region where the solution $u(x,t)$ to the SG equation (2.1) decays to zero faster than any algebraic degree [19, 47]. In this region, we introduce the matrix factorization

$$G(z,x,t) = M(z,x,t)P(z,x,t), \tag{2.24}$$

where

$$M(z,x,t) = \begin{pmatrix} 1 & \overline{\rho(\overline{z})}\exp(-\theta(z,x,t)) \\ 0 & 1 \end{pmatrix},$$

$$P(z,x,t) = \begin{pmatrix} 1 & 0 \\ \rho(z)\exp(\theta(z,x,t)) & 1 \end{pmatrix}.$$

Since

$$\mathrm{Re}(\theta(z,x,t)) = -\frac{\mathrm{Im}(z)(x+t)}{2} - \frac{\mathrm{Im}(z)(x-t)}{2\left|z\right|^2} \begin{cases} < 0, & \mathrm{Im}\ z > 0, \\ > 0, & \mathrm{Im}\ z < 0, \end{cases} \tag{2.25}$$

the exponentials in M and P are bounded and decaying if P is defined in the upper-half z-plane and M is defined in the lower-half z-plane, respectively for $|z| \to 0,\ \infty$ along rays from the origin. Therefore, by a deformation using the lensing [73] from the real line to the contour in Figure 4.4, we get a new RHP,

$$\Phi^+ = \begin{cases} \Phi^- P, & z \in l_1, l_2, l_3, l_4, \\ \Phi^- M, & z \in l_5, l_6, l_7, l_8. \end{cases}$$

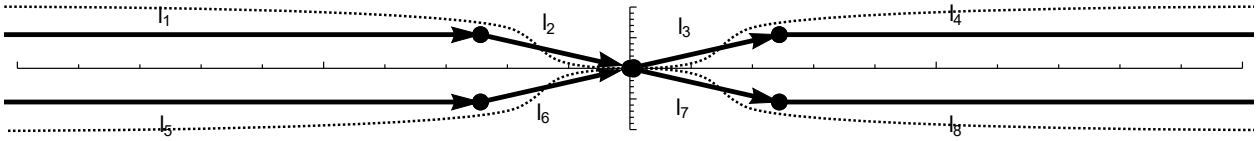

Figure 2.9: The jump contour in the complex plane in the region $x \geq t$ with the $G = MP$ decomposition. The jump contour forms an X shape at the origin. Away from the origin, deformations are inside the dashed lines which are the boundary of $\mathcal{D}_\delta$. Near the origin, the straight lines can still be used since the jump matrix is near identity. See the end of Section 2.4.1 for how to pick the four end points of the line segments.

The new contour consists of straight-line segments l_1-l_8. Since $\rho(z)$ is not entire, we are limited in where we can deform to get better decay from the exponential. Away from $z = 0$, the width of the strip of analyticity of $\rho(z)$ along the real axis is given by δ defined in (2.2). The condition number of the collocation method matrix near $z = 0$ for (2.11) is shown in Figure 2.5, the level sets are used to determine the deformation. In practice, first we pick the height $\mathrm{Im(z)} = \nu < \delta/2$ to determine the $y-$coordinate of the horizontal segments l_1, l_4, l_5, l_8. Then $|\mathrm{Re}(i(z - 1/z)/4)| = 2\nu$ determines the circle centered at $z = i/8\nu$ with radius $1/8\nu$. The points on the circle give approximately the same condition number. Therefore, we can solve for the intersections of the circle with the horizontal line $\mathrm{Im}(z) = \nu$. For convenience, the arc from $z = 0$ to the line $\mathrm{Im}(z) = \nu$ is replaced by a straight line in our experiments since $\nu < 0.4$ is small. The deformations near $z = 0$ in other asymptotic regions, with the exception of the transition region, are determined using the same method.

2.4.2 Region 2: Outside the light cone, characterized by $x \leq -t$

This is the other region where $u(x, t)$ decays to zero faster than any algebraic degree [19, 47]. In this region, the sign of the real part of θ is the opposite of (2.25). A different matrix factorization is needed:

$$G = LDU, \tag{2.26}$$

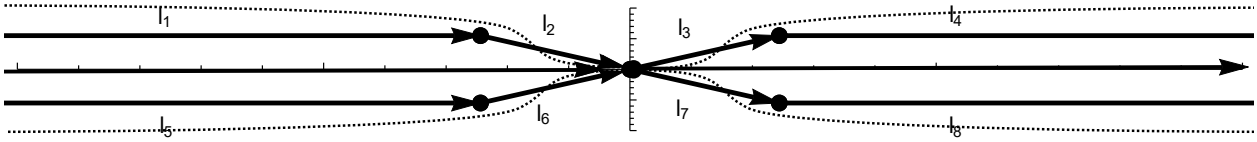

Figure 2.10: The jump contour in the complex plane in the region $x \leq -t$ with the $G = LDU$ decomposition. Away from the origin, deformations are inside the dashed lines which are the boundary of $\mathcal{D}_\delta$. Near the origin, the straight lines can still be used since the jump matrix is nearly identity. The jump on the real line introduces large oscillations in the solution and needs to be removed to obtain uniform accuracy. After the removal of the jump on the real line, the contour is of the same shape as in Figure 4.4.

where

$$L(z,x,t) = \begin{pmatrix} 1 & 0 \\ \frac{\rho(z)}{\tau(z)} \exp(\theta(z,x,t)) & 1 \end{pmatrix},$$

$$U(z,x,t) = \begin{pmatrix} 1 & \frac{\overline{\rho(\overline{z})}}{\tau(z)} \exp(-\theta(z,x,t)) \\ 0 & 1 \end{pmatrix},$$

$$D(z) = \begin{pmatrix} \tau(z) & 0 \\ 0 & \frac{1}{\tau(z)} \end{pmatrix},$$

and $\tau(z) = 1 + \overline{\rho(\overline{z})}\rho(z)$. The jump function L contains a decaying exponential if it is defined in the lower-half z-plane while the jump function U has decaying exponential if it is defined in the upper-half plane, respectively for $|z| \to 0,\ \infty$ along rays from the origin. We get an RHP as shown in Figure 2.10:

$$\Phi^+ = \begin{cases} \Phi^- U, & z \in l_1, l_2, l_3, l_4, \\ \Phi^- D, & z \in \mathbb{R}, \\ \Phi^- L, & z \in l_5, l_6, l_7, l_8. \end{cases}$$

Similar to the discussion in region 1, straight lines are used since the jump matrix converges to the identity matrix exponentially. To obtain uniform accuracy, all the jump matrices need to approach the identity matrix away from the saddle points [73]. For the diagonal jump

matrix D, we can write down the exact solution $\Delta(z)$ to the RHP,

$$\Delta^+ = \Delta^- D,\ z \in \mathbb{R},\ \lim_{z\to\infty} \Delta(z) = I,$$

where

$$\Delta(z) = \begin{pmatrix} \delta(z) & 0 \\ 0 & 1/\delta(z) \end{pmatrix},$$

and

$$\delta(z) = \exp\left(\frac{1}{2\pi i}\int_{-\infty}^{\infty} \frac{\log(\tau(s))}{s-z} ds\right).$$

Hence, using the mapping $\Phi^+ \mapsto \Phi^+\Delta^{-1}$ and $\Phi^- \mapsto \Phi^-\Delta^{-1}$ we can remove the jump D on $\mathbb{R}$ and the contour becomes the same as in Figure 4.4 with

$$\Phi^+ = \begin{cases} \Phi^-\Delta U\Delta^{-1}, & z \in l_1, l_2, l_3, l_4, \\ \Phi^-\Delta L\Delta^{-1}, & z \in l_5, l_6, l_7, l_8. \end{cases}$$

2.4.3 Region 3: Inside the light cone, characterized by $|x| < t$

The deformation in Region 3 is more complicated. Deformations similar to those for the previous two regions are used and new deformations near the saddle points are also required. For convenience, we denote the jump matrices on the contours in Figures 2.11, 2.12 and 2.13. For instance, a jump matrix G next to the oriented contour means that the solution to the RHP Φ satisfies $\Phi^+ = \Phi^- G$. When (x,t) is inside the light cone, we have two real saddle points at $\pm z_0 = \pm\sqrt{(t-x)/(t+x)}$ satisfying $\theta'(z_0, x, t) = 0$. The two saddle points are moving away from the origin and are unbounded when $x \to -t$. They approach the origin when $x \to t$. Note that in Region 1 and Region 2, $|x| \geq t$, the two saddle points are purely imaginary. Near the two real saddle points,

$$\theta(z,x,t) = \frac{i(t-x)}{\sqrt{\frac{t-x}{t+x}}} + \frac{i(t+x)\left(z - \sqrt{\frac{t-x}{t+x}}\right)^2}{2\sqrt{\frac{t-x}{t+x}}} + O\left(\left(z - \sqrt{\frac{t-x}{t+x}}\right)^3\right). \tag{2.27}$$

To get decay from the quadratic term, for $\mathrm{Re}(z) > z_0$ and $\mathrm{Re}(z) < -z_0$, we need the $G = MP$ factorization and for $-z_0 < \mathrm{Re}(z) < z_0$ we need the $G = LDU$ factorization. Figure 2.11

shows the deformation with saddle points at $\pm z_0 \approx \pm 1.1$. Furthermore, to get uniform accuracy, we need to remove the jump $D(z)$ on $(-z_0, z_0)$ by introducing the RHP,

$$\Delta^+ = \Delta^- D,\ z \in (-z_0, z_0),\ \lim_{z\to\infty} \Delta(z) = I,$$

with exact solution

$$\Delta(z; z_0) = \begin{pmatrix} \delta(z; z_0) & 0 \\ 0 & 1/\delta(z; z_0), \end{pmatrix},$$

and

$$\delta(z; z_0) = \exp\left(\frac{1}{2\pi i}\int_{-z_0}^{z_0} \frac{\log(\tau(s))}{s - z} ds\right).$$

In this case, $\delta(z; z_0)$ has singularities at $\pm z_0$. To avoid using contours passing through the singularity, we introduce a new square contour centered at the singularity as in Figure 2.12. The length of the side is on the order of $\sqrt{(t+x)^3}/\sqrt{t-x}$ determined by the coefficient of the quadratic term in (2.27). When $x \to -t$, since $\rho(z_0)$ decays to zero quickly, the contour near the saddle points may be truncated and therefore the contour degenerates to the contour in region 2. From the expansion of $\theta(z, x, t)$ (2.27), we can see that the localization depends on the absolute value of the coefficient of the quadratic term. When $t + x \approx 0$, the jump matrix may still be very oscillatory due to the insufficient decay in z. However, since the constant term in (2.27) determines the overall amplitude of the jump matrix which will be truncated if it gets too small, the oscillation cannot become arbitrarily large. Two techniques are used to deal with the intermediate oscillatory case. A technique to compute the solution for $x < 0$ is to use a reflected initial values $v(x, 0) = u(-x, 0)$ which gives a new set of scattering data but only requires the deformation of the contour in the $x > 0$ case for $v(x, t) = u(-x, t)$. The other technique is to precompute the reflection coefficient along the contour on a coarser grid and use the interpolants to construct the jump matrix. This is effective because the oscillation is mostly introduced by $\theta(z, x, t)$ but the refection coefficient itself is smooth as in Figure 2.4. On the other hand, when $x \to t$, the collision of the two saddle points $\pm z_0$ at the origin results in a contour in region 1, and the $G = LDU$ factorization is indeed not necessary in the transition region, as we now demonstrate.

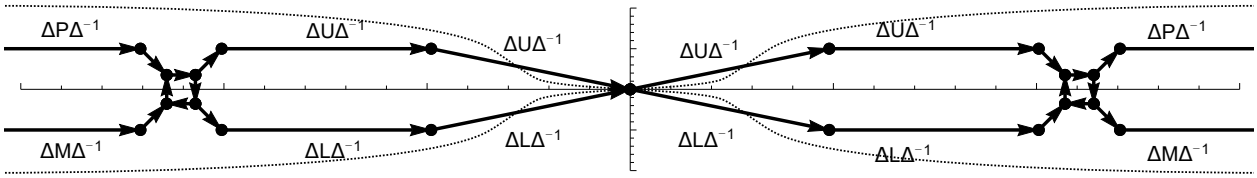

Figure 2.11: The jump contour in the complex plane in the region $|x| < t$ with the jump functions labeled to each segment. Away from the origin deformations are inside the dashed lines which are the boundary of $\mathcal{D}_\delta$. Near the origin, the straight lines can still be used since the jump matrix is nearly identity. The center of the squares are the saddle points z_0 and $-z_0$.

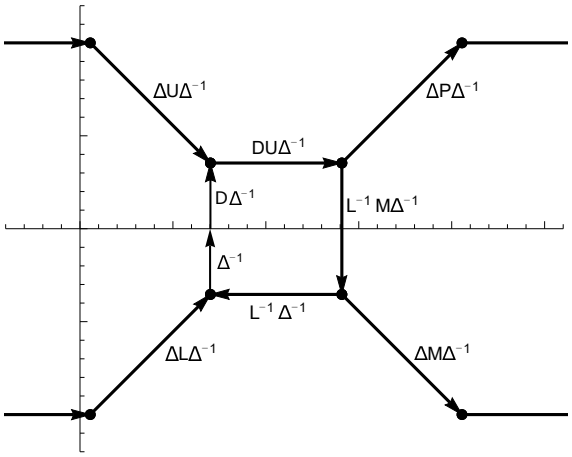

Figure 2.12: A zoom-in of the contour in Figure 2.11 at the right saddle point. The four oriented contours pointed at/from the square are along the direction of steepest descent ($\pi/4$ from real axis). The center of the square is the saddle point z_0.)

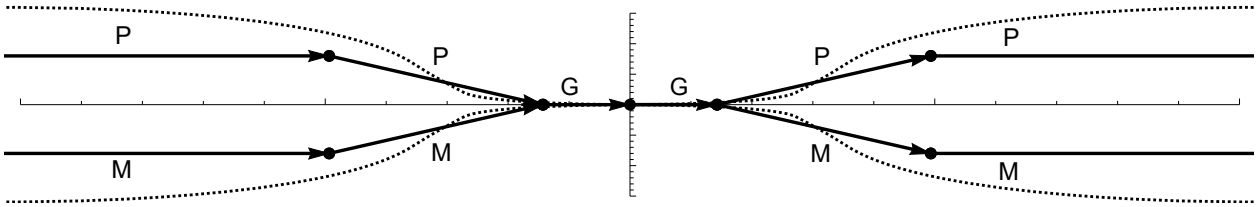

Figure 2.13: The jump contour in the complex plane in the transition region. When the saddle points are near the origin, the $G = LDU$ decomposition is collapsed to the real line. Away from the origin, deformations are inside the dashed lines which are the boundary of $\mathcal{D}_\delta$. Near the origin, the straight lines can still be used since the jump matrix is nearly identity.

2.4.4 Region 4: Transition, inside region 3 characterized by $t(t-x) \leq 1$

When $t - x = \varepsilon > 0$ is small, the saddle points approach the origin. This is classified as a transition region in [47]. Consider $z_0 < 1/t$ and $-z_0 < z < z_0$, then

$$|\theta(z,x,t)| = |zt| + \frac{1}{2}\left|(z-1/z)(t-x)\right| \leq 1 + \frac{1}{2}\left|(z-1/z)\right|\epsilon.$$

The oscillation is indeed controlled between the two saddle points when their distance is sufficiently close. In this case, from Theorem 2.74 and Corollary 2.75 in [73], the Sobolev norm of the solution q to the SIE (2.22) can be bounded uniformly in x and t since $\theta(z,x,t)$ is bounded independent of x and t. Therefore there is no need to use the $G = LDU$ factorization and we can collapse the contour back to the real line as in Figure 2.13.

2.5 Numerical results

We present some numerical examples and tests of the NIST for the SG equation on the whole line.

2.5.1 Propagation of dispersive waves

Let

$$u_s(x,t) = 4\arctan\left(e^x\right),$$

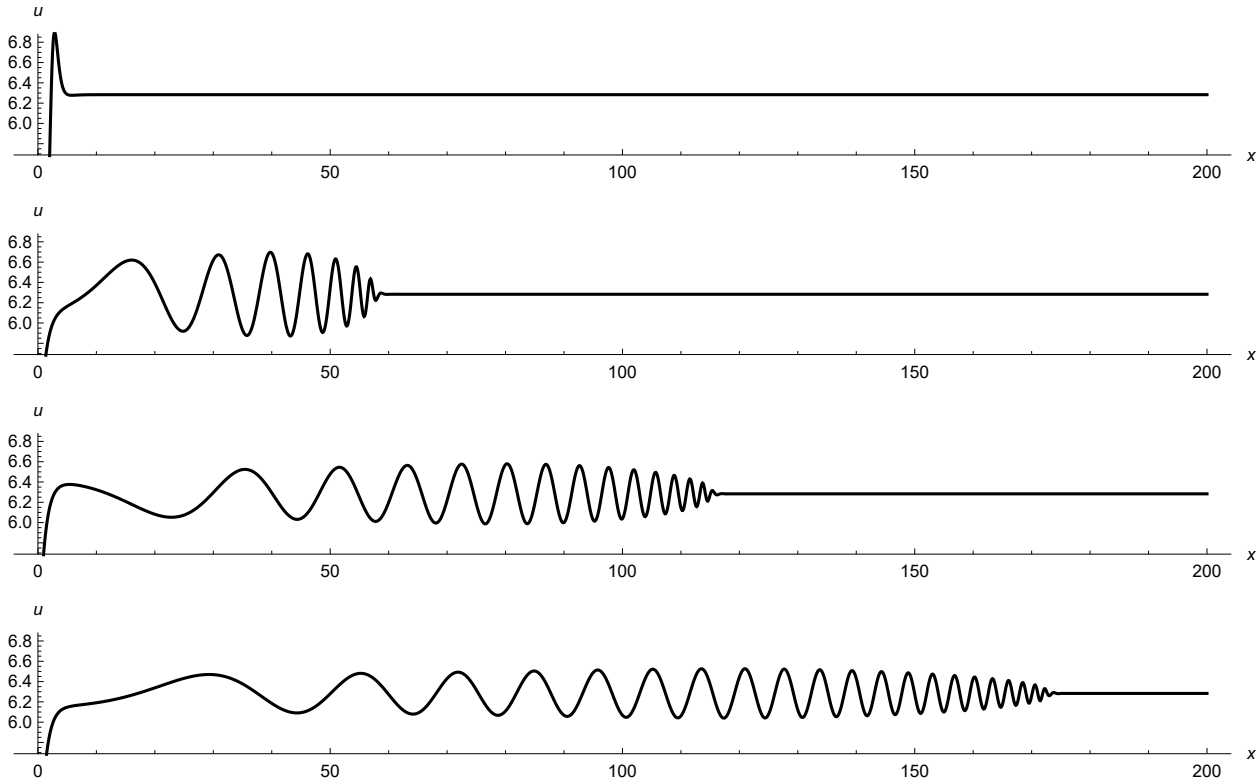

Figure 2.14: The propagation of dispersive waves to the right from a perturbed stationary kink located at $x = 0$ when $t = 2.5$, 60, 120, 180. The initial values are given by Equation (2.28).

be a one-soliton stationary kink solution. We choose the initial values to be a (not small) perturbation of $u_s(x, 0)$,

$$u(x, 0) = u_s(x, 0) + 5\,\mathrm{sech}^2(x),\ u_t(x, 0) = 0. \tag{2.28}$$

The magnitude of the perturbation is chosen to introduce large dispersion while the number of eigenvalues in the scattering problem does not change. Figure 2.14 shows dispersive waves generated by the perturbation from the kink at $t = 2.5$, 60, 120, 180. Due to the oscillations and the different scales, the solution is difficult to obtain with traditional numerical methods while maintaining high accuracy for long time.

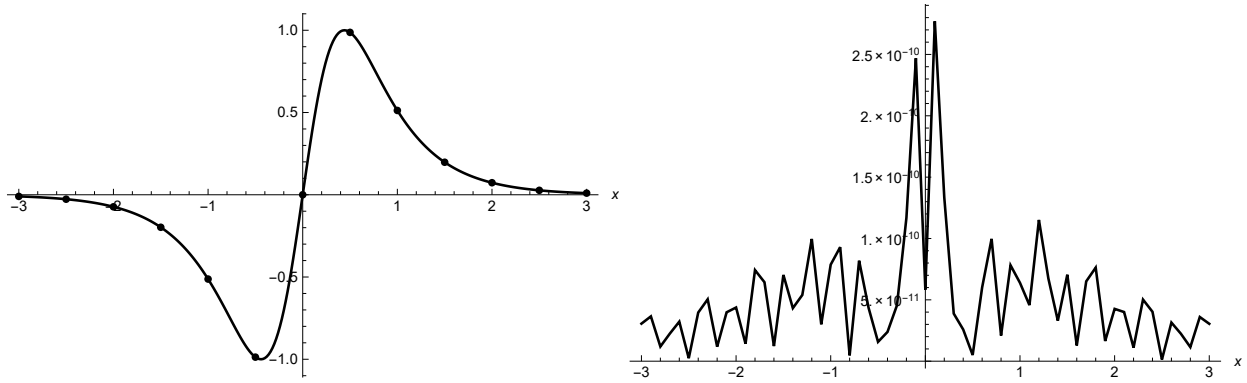

Figure 2.15: (Left) Solid: The exact initial values $\sin(u(x,0))$, Dots: The computed solution. (Right) The absolute error. The initial values are given by Equation (2.19) and $\mu = 0$, $n = 0$, $\epsilon = 2$.

2.5.2 Recovery of the initial values

As mentioned in Section 2.3.2, we can solve the RHP at $t = 0$ and compare it with the known initial values to verify that all eigenvalues have been computed. This is one way to check the accuracy when the exact solution is not known. Figure 2.15 shows the computed initial values using the NIST on the left at $t = 0$ with initial values (2.19) and $\mu = 0$, $n = 0$, $\epsilon = 2$. The absolute error is shown on the right and is on the order of 10^{-10}. Although it is a triviality for numerical methods like finite differences to check the initial values, in the NIST, computing $u(x, 0)$ requires going through the entire procedure of forward scattering and inverse scattering. Computing short time solutions costs more compared with computing the solutions for long time since the contour becomes more localized when t is large [60]. With the same initial value, the spectral convergence at $x = 1.5$, $t = 1$ is verified in Figure 2.16. The error is measured by the difference of two numerical solutions with a different number of collocation points, $e_{N_i} = \left|u_{N_{i+1}} - u_{N_i}\right|$. Linear behavior in the log plot indicates spectral convergence.

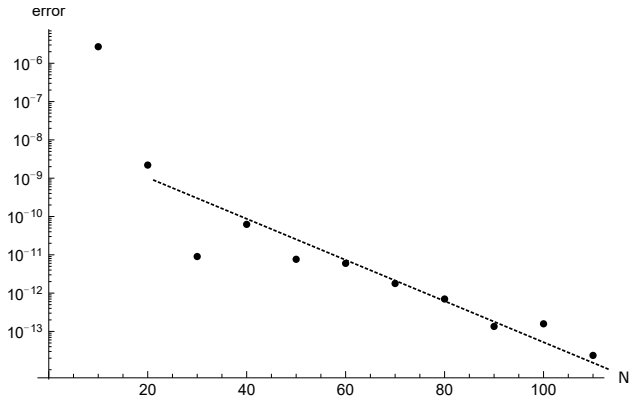

Figure 2.16: The log-linear plot of the error *vs.* number of collocation points for $u(1.5, 1)$. The dashed line is a reference straight line. The initial values are given by Equation (2.19) and $\mu = 0$, $n = 0$, $\epsilon = 2$.

2.5.3 Evolution of multi-soliton solutions with perturbations

In [17], the initial values (2.19) with $\epsilon = \gamma/(2n+1)$ are used so that one can compute pure soliton solutions by solving an algebraic system in the semiclassical limit $\epsilon \to 0$. If the condition $\epsilon = \gamma/(2n+1)$ is not satisfied, an RHP has to be solved due to the non-zero reflection coefficient, and the algebraic method does not apply. One expects that the non-zero reflection coefficient perturbs the solution only by a small amount, and the pure soliton solution approximates the general solution as $\epsilon \to 0$. In Figure 2.17, we show the pure soliton solution with $\mu = 0, n = 2, \epsilon = 0.2$ in the left panel. The perturbed solution with $\mu = 0, n = 2, \epsilon = 0.17$ is in the right panel using the NIST. In both cases the reflection coefficient has five poles on the unit circle in the upper-half plane. In the study of the semiclassical limit $\epsilon \to 0$, the scaling $X = \epsilon x$ and $T = \epsilon t$ is relevant. This transforms the SG equation to

$$\epsilon^2 U_{TT} - \epsilon^2 U_{XX} + \sin(U) = 0.$$

Therefore the domain $\epsilon x \in [-2.5, 2.5]$, $\epsilon t \in [0, 5]$ remains the same in Figure 2.17. The two plots are similar with a small difference of contour lines near the center of the plots. We remark that computing a 2D contour plot is not efficient using the NIST since the advantage

of the NIST is that the solution is computed at specified (x,t) without time-stepping. All points in the evolution are required in a 2D plot. However, it is competitive to use the NIST in this case if one wants accurate solutions containing dispersive waves for large time. In Figure 2.18, we compare the numerical solution by the NIST with a standard centered-difference method along the line $x = 4.5$. To prevent introducing error due to domain truncation, we choose the domain from $[-7.5/\epsilon, 7.5/\epsilon]$. The left plot shows the oscillatory evolution of the solution mostly due to the existence of breathers with the error on the order of 10^{-8}. The dispersive waves are not large enough to be observed in the plot. In the right panel of Figure 2.18, three grid sizes $\Delta x = 0.05, 0.1, 0.2$ are used with the time step $\Delta t = \Delta x/2$ to satisfy the stability condition. These step sizes are sufficient to resolve the oscillations in the plot but the error is on the order of 0.01 for small time and seems to grow to order 1 linearly. As a result, an extremely dense grid is required to get the solution with error smaller than 10^{-8}.

2.5.4 Uniform convergence for large t and x

Cheng, Venakides and Zhou [19] studied the long-time asymptotics for solitonless initial values. Outside the light cone, the solution decays to zero spectrally. Inside the light cone, let

$$z_0 = \sqrt{\frac{t-x}{t+x}}, \quad \tau = \frac{tz_0}{1+z_0^2},$$

then as $\tau \to \infty$,

$$\cos(u) - 1 = -\frac{4\,|\nu(z_0)|}{\tau}\cos^2(2\tau + \nu(z_0)\log(8\tau) + \beta(z_0)) + O\left(C(z_0)\frac{\log(\tau)}{\tau^{3/2}}\right), \tag{2.29a}$$

$$\sin(u) = \sqrt{\frac{8\,|\nu(z_0)|}{\tau}}\cos(2\tau + \nu(z_0)\log(8\tau) + \beta(z_0)) + O\left(C(z_0)\frac{\log(\tau)}{\tau}\right), \tag{2.29b}$$

where

$$\nu(z_0) = -\frac{1}{2\pi}\log(1+|\rho(z_0)|^2),$$

$$\beta(z_0) = -\arg(\Gamma(\nu(z_0)i)) - \arg(\overline{\rho(z_0)}) + \frac{\pi}{4} - \frac{1}{\pi}\int_{-z_0}^{z_0}\log(z_0-s)d\log(1+|\rho(s)|^2).$$

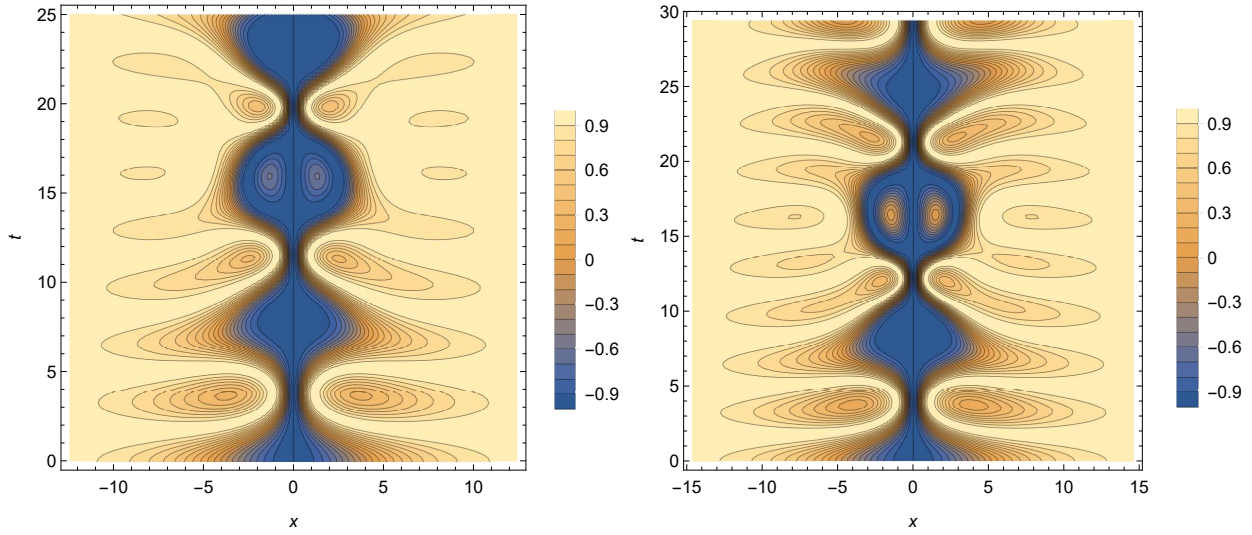

Figure 2.17: (Left) The numerical solution $\cos(u)$ with initial values (2.19), $\mu = 0$, $n = 2$ and $\epsilon = 0.2$. In this case the reflection coefficient vanishes. $\rho(z) \equiv 0$. The solution consists of several solitons as discussed in Section 2.3.2. (Right) The numerical solution with initial values (2.19), $\mu = 0$, $n = 2$ and $\epsilon = 0.17$. In this case, the solitons are perturbed and small dispersive waves exists since $\rho(z) \not\equiv 0$ but dispersive waves are hardly seen due to the small amplitude. The domain is the same in the two plots with scaling $\epsilon x \in [-2.5, 2.5]$, $\epsilon t \in [0, 5]$.

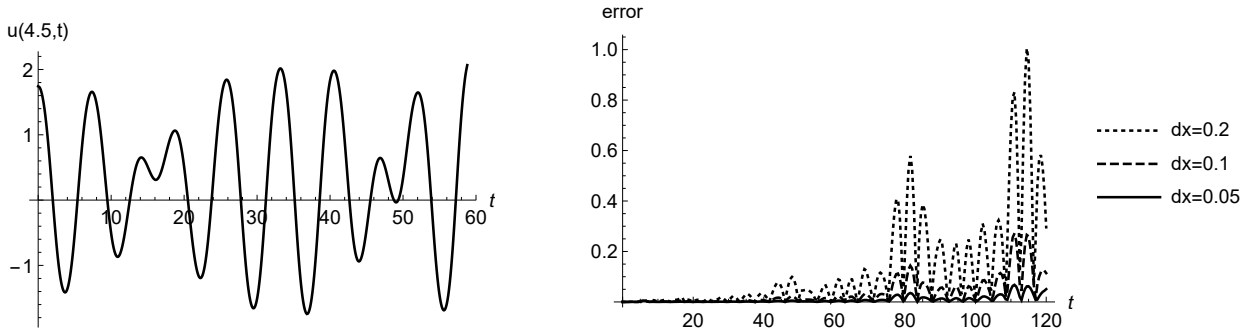

Figure 2.18: (Left) The numerical solution by the NIST $u(4.5, t)$. (Right) The absolute error (assuming the true solution is from the NIST) of second-order finite-difference method with various grid sizes at $x = 4.5$, $t \in [0, 120]$. The initial values are given by Equation (2.19) with $\mu = 0$, $n = 2$ and $\epsilon = 0.17$.

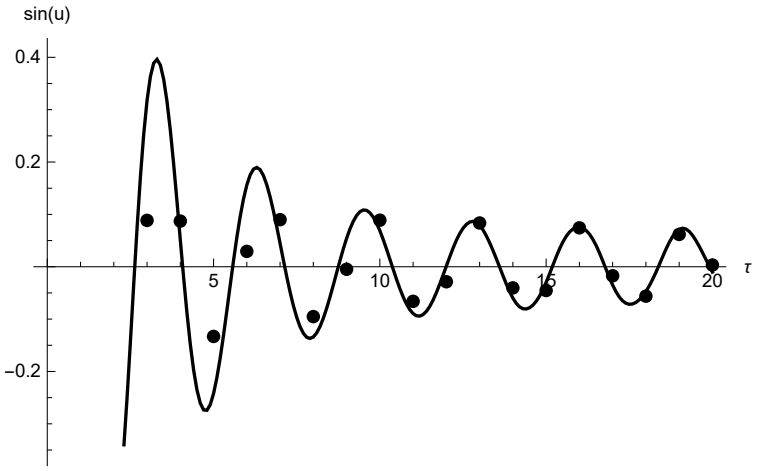

Figure 2.19: Comparison of the numerical solution $\sin(u(\tau))$ (Solid) to the asymptotic formula given by (2.29b) (Dots) for $\tau \in [0, 20]$, $z_0 = \sqrt{1/2}$. The initial values are $u(x, 0) = \mathrm{sech}^2(x)$ and $u_t(x, 0) = 0$.

Here, $\Gamma(\cdot)$ denotes the Gamma function and $C(z_0)$ decays faster than any power of z_0 as $z_0 \to \infty$. In Figures 2.19, 2.20, 2.21, we compare the numerical solution with asymptotic formula inside the light cone region $z_0 = \sqrt{1/2}$ with initial values $u(x, 0) = \mathrm{sech}^2(x)$ and $u_t(x, 0) = 0$. The observed orders of the correction terms are one half order smaller than the order given by the asymptotic formula. This is true for all initial values we have tested, which indicates a possible refinement of the estimates of the correction terms in [19].

2.5.5 Comparison with the auto-Bäcklund transformation

An important property of integrable systems is that they have a Bäcklund transformation. Two solutions $u(x, t)$ and $v(x, t)$ to (2.1) satisfy the auto-Bäcklund transformation if they satisfy the following equations [29],

$$u_x + u_t = v_x + v_t + 2k \sin\left(\frac{u+v}{2}\right), \tag{2.30a}$$

$$u_x - u_t = -(v_x - v_t) + \frac{2}{k} \sin\left(\frac{u-v}{2}\right). \tag{2.30b}$$

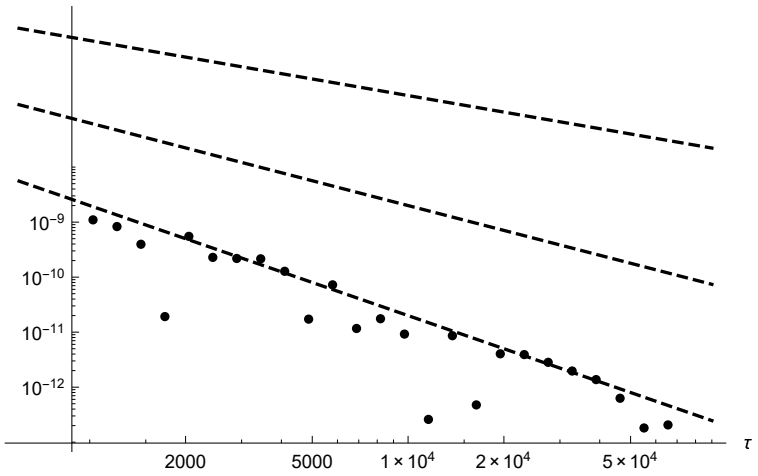

Figure 2.20: The absolute error between the numerical solution $\cos(u(\tau))$ and the asymptotic formula. (Dot) The error/$\log(\tau)$. (Dashed) Auxiliary lines with slope $-1, -1.5, -2$. The least square fit of the error/$\log(\tau)$ has slope -1.95, as opposed to -1.5, predicted by [19]. The initial values are $u(x,0) = \operatorname{sech}^2(x)$ and $u_t(x,0) = 0$.

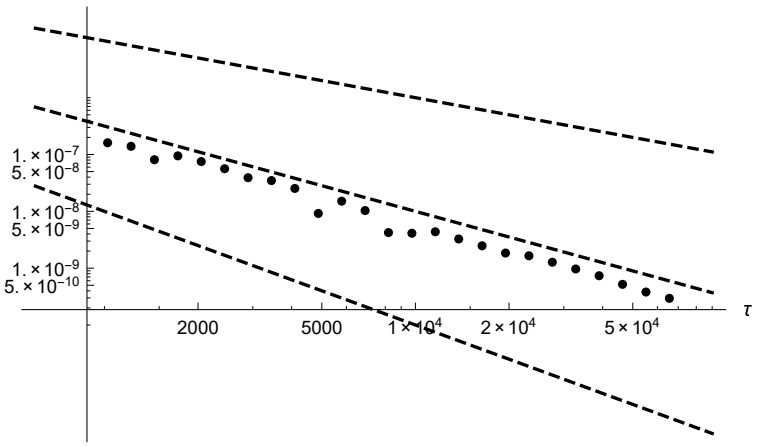

Figure 2.21: The absolute error between the numerical solution $\sin(u(\tau))$ and the asymptotic formula. (Dot) The error/$\log(\tau)$. (Dashed) Auxiliary lines with slope $-1, -1.5, -2$. The least square fit of the error/$\log(\tau)$ has slope -1.53, as opposed to -1, predicted by [19]. The initial values are $u(x,0) = \operatorname{sech}^2(x)$ and $u_t(x,0) = 0$.

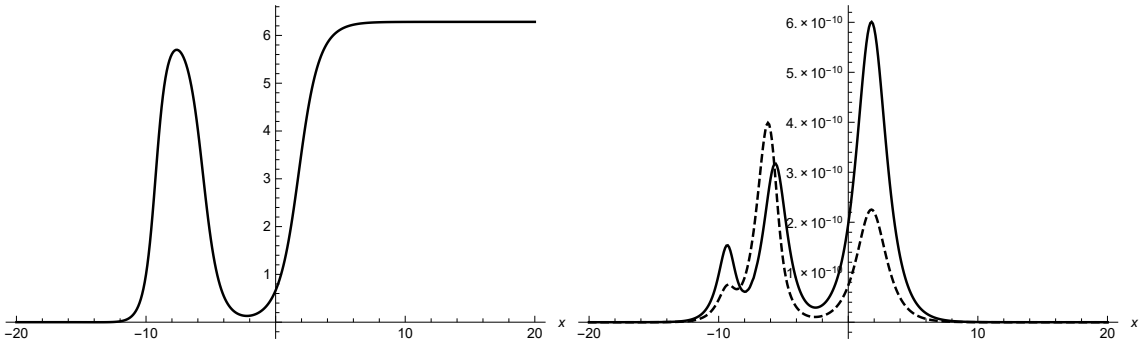

Figure 2.22: Left: The exact three-soliton solution at $t = 10$. Right: The error compared with the exact solution (solid) and the residual of (2.31) (dashed). The initial values are determined by computing a 3-soliton solution using Equation (2.31) and (2.32).

By choosing the parameter k, we can find a new solution u from a known solution v using the transformation. The effect of the transformation is the addition or removal of one zero of $a(z)$ in the upper-half plane. By cancellation of the derivative terms in the transformation (2.30a, 2.30b) using parameters k_1, k_2 in different order, we get an algebraic consistency condition among four solutions r, u, v, w to (2.1),

$$\tan\left(\frac{w-r}{4}\right) = \frac{k_2+k_1}{k_2-k_1}\tan\left(\frac{u-v}{4}\right), \tag{2.31}$$

where v is obtained using (2.31) with r, k_1 and u is obtained using (2.30a, 2.30b) with r, k_2. Since the trivial solution $v = 0$ satisfies (2.1), we obtain three one-soliton solutions u_j from (2.30a, 2.30b),

$$u_j = 4\arctan\left(\exp\left(k_j x + \frac{1}{k_j}t\right)\right),\ k_j = j,\ j = 1, 2, 3. \tag{2.32}$$

and construct a three-soliton solution by using (2.31) repeatedly. Figure 2.22 shows the three-soliton solution at $t = 10$ on the left. The error comparing with the exact solution is shown in a solid line in the right plot. The residual of (2.31) is examined by computing all the soliton solutions from their initial values to $t = 10$ independently. Both the absolute error and the residual stay small uniformly in both t and x in the computation.

Chapter 3

THE NUMERICAL UNIFIED TRANSFORM METHOD FOR LINEAR PDES ON THE HALF-LINE

In this chapter, we implement the UTM as a numerical method to solve several linear evolution PDEs on the half-line. With the help of contour deformations and oscillatory integration techniques, the method's complexity does not increase for large x, t and the method is more accurate as x, t increase (absolute errors are smaller, relative errors are bounded).

3.1 The Unified Transform Method for linear PDEs

Standard methods for solving linear evolution PDEs, including separation of variables and classical integral transforms, are often limited by the order of the PDE and the type of boundary conditions. The UTM is a relatively new method for analyzing a large family of PDEs with general initial and boundary conditions [33]. When applied to IBVPs for linear, constant coefficient PDEs, the UTM provides the solutions in terms of contour integrals involving the given initial and boundary conditions [23]. This does not only give rise to new analysis but it also provides a new direction for numerical methods. With this integral representation of the solution, it is possible to compute the solution at any x, t directly. The NUTM is a numerical method built upon the solution formula from the UTM with the addition of systematic contour deformations. In stark contrast to classical numerical PDE methods such as finite-difference methods, most spectral methods and finite-element methods, the NUTM can solve equations in unbounded domains and it does not experience accumulation of errors or stability issues. These issues that appear in standard numerical methods for evolution PDEs do not appear in the NUTM because spatial discretization

and time stepping are not required. As a hybrid analytical-numerical method, the NUTM operates in a complementary direction to the traditional numerical methods. In practice, if one is interested in the solution on a dense spacial and temporal grid and is satisfied with lower accuracy, traditional methods are better choices, whereas if one is interested in the solution along some curve with high accuracy for a long time, the NUTM is likely better. On the other hand, the NUTM can act as a benchmark tool for other numerical methods.

Since the first paper on the NUTM in 2008 [30], the method has been applied to the heat equation $q_t = q_{xx}$ on the half-line [30, 36] and on finite intervals [61], to the Stokes equations $q_t \pm q_{xxx} = 0$ on the half-line [30] and on finite intervals [54], and the advection-diffusion equation $q_t + q_x = q_{xx}$ on the half-line [20]. These applications of the NUTM use fixed contours that do not depend on (x, t) and most of them[1] rely on knowing closed-form expressions for the transforms of initial and boundary data. We refer to such implementations of the NUTM as fixed contour methods (FCMs). As we will see in Section 3.3.3, FCMs become less accurate for large x, t. In contrast to those FCMs, we propose a new implementation of the NUTM that uses contours depending dynamically on x, t and that does not severely restrict the initial or boundary conditions. Our goal is to make no assumptions on the functional form of the initial or boundary functions, other than to restrict them to be in certain function spaces (*i.e.*, impose specific decay). Our NUTM maintains high accuracy in a large region of the (x, t) plane. Similar to the discuss in Section 1.5, we build up the NUTM to include the following features:

1. The method gives the solution at given (x, t) **without time-stepping or spatial discretization**.

2. The method is **spectrally accurate** in that the error at fixed (x, t), $E_{\text{NUTM}}(N, x, t) = \mathcal{O}(1/N^l)$ for any integer l, where N is the number of arithmetic operations. For certain equations such as the heat equation, it is possible to achieve spectral accuracy uniformly

[1] In [20], one numerical example without closed-form expressions for the transforms is considered, but the idea is not applied to non-dissipative problems.

as long as (x, t) are bounded away from $x = 0$ and $t = 0$.

3. The method is **uniformly accurate** in the sense that the computational cost to compute the solution at a point (x, t) with given accuracy remains bounded for large x, t. In addition, we observe bounded relative errors in our numerical experiments.

4. The assumptions on the initial and boundary conditions are significantly weakened compared to the FCM. Decay and regularity conditions are necessary for the purpose of achieving high accuracy. We emphasize that **closed-form expressions for the transforms of initial or boundary conditions are not required**.

5. The method does not artificially truncate the infinite physical domain.

In this chapter, we consider linear, constant coefficient, one-dimensional scalar evolution equations on the half-line $x \geq 0$. This chapter is organized as follows: Section 3.2 gives a brief overview of the UTM and the methods for oscillatory integrals that are required in what follows. In Section 3.3, we discuss the NUTM for the heat equation where the deformation is based on the method of steepest descent. In Section 3.4, we discuss the NUTM applied to the linear Schrödinger equation where methods other than the method of steepest descent are needed. In Section 3.5, we show how to apply the NUTM to a third-order PDE with an advection term giving rise to integrands with branch points. We believe that the best way to explain the NUTM, similar to introducing the UTM, is to use a case-by-case study. In Section 6, we summarize the steps of the NUTM.

Numerical examples are provided throughout. In many examples the initial and boundary conditions are chosen to have closed-form transforms for the purpose of computing the true solution for comparison. An example with the boundary condition which does not have a known expression for the transform is shown at the end of Section 5.2. The proof of the uniform convergence of the NUTM applied to the heat equation is given in the Appendix.

3.2 Methods for computing oscillatory integrals

3.2.1 The unified transform method on the half-line

Consider a linear PDE written as

$$q_t + \omega(-i\partial_x)q = 0, \tag{3.1}$$

for $x, t > 0$. We assume $\omega(k)$ to be a polynomial of degree p. Note that $q(x,t) = e^{ikx-\omega(k)t}$ satisfies (3.1). This definition of the dispersion relation ω typically used in the UTM differs from the common convention by a factor of i. The UTM solves IBVPs for (3.1) using transforms of the initial and boundary values,

$$\hat{q}_0(k) = \int_0^\infty e^{-ikx} q_0(x,0)dx, \tag{3.2a}$$

$$\tilde{g}_0(\omega(k),t) = \int_0^t e^{\omega(k)s} q(0,s)ds, \tag{3.2b}$$

$$\vdots$$

$$\tilde{g}_{p-1}(\omega(k),t) = \int_0^t e^{\omega(k)s} \frac{\partial^{p-1} q}{\partial x^{p-1}}(0,s)ds. \tag{3.2c}$$

The number of boundary conditions required for a well-posed problem is determined by the UTM. It is based on the order of the highest spatial derivative as well as the leading coefficient of ω [30]. The solution formula from the UTM depends on contour integrals of the type

$$I_m = \int_{\mathcal{C}_m^I} e^{ikx-w(k)t} \hat{q}_0(\nu_m(k))dk, \quad m = 1, 2, \ldots, p,$$
$$B_m = \int_{\mathcal{C}_m^B} e^{ikx-w(k)t} f_m(k) \hat{g}_m(\omega(k),t)dk, \quad m = 0, 1, \ldots, n,$$

where p is the degree of $\omega(k)$ and $\nu_m(k)$ is its mth symmetry[2], and $f_m(k)$ is a function explicitly determined by $\omega(k)$, independent of the initial and boundary data. Thus, the

[2] A symmetry $\nu(k)$ of $\omega(k)$ satisfies $\omega(\nu(k)) = \omega(k)$. The symmetries play an important role in the UTM. The n symmetries $\{\nu_m(k) : m = 1, 2, \ldots, n\}$ exist by the fundamental theorem of algebra, and can be chosen to be analytic outside a compact set [35].

solution to (3.1) can be computed by quadrature. However, the integrands on the contours $\mathcal{C}_m^I$ and $\mathcal{C}_m^B$ obtained by the UTM are often highly oscillatory, and suitable methods must be applied for an accurate solution.

3.2.2 Methods for oscillatory integrals

The exponential factor $e^{ikx-w(k)t}$ in the integrand is the main cause of oscillations. Deformations based on the method of steepest descent [57] change the oscillations into exponential decay. Define the phase function $\theta(k;x,t) = ikx - w(k)t$. Saddle points k_0 satisfy

$$\frac{d\theta(k;x,t)}{dk}\Big|_{k=k_0} = 0.$$

Near $k = k_0$,

$$\theta(k;x,t) = ik_0x - w(k_0)t - \frac{w''(k_0)t}{2}(k-k_0)^2 + \mathcal{O}(k-k_0)^3.$$

The integrand is (locally) exponentially decaying if k follows a path such that $-w''(k_0)(k-k_0)^2$ is negative and decreasing. Since the integrals along the deformed paths are exponentially localized near the saddle point, they can be computed with high accuracy with standard quadrature methods after appropriate truncation.

For improved accuracy, Gauss-Hermite or Gauss-Laguerre quadratures are suitable, depending on the form of the exponentials and the paths [42, 48, 75]. We choose Clenshaw-Curtis quadrature for the deformed contour integrals for convenience, as it is spectrally accurate and efficient in most cases [67]. We note that there are situations where the deformations are restricted and the method of steepest descent is not applicable, see Sections 3.4 and 3.5.

The region in the complex k-plane where the contour can be deformed depends on the analyticity of the transform data $\hat{q}_0(k)$ and $\hat{g}_m(\omega(k),t)$ which is related to the decay rate of the initial and boundary data. For instance, when $q(x,0)$ and $q(0,t)$ are integrable, $\hat{q}_0$ is analytic and bounded in the lower-half plane $\{k \in \mathbb{C} : \mathrm{Im}\,(k) < 0\}$ and $\hat{g}_0(\omega(k),t)$ is analytic and bounded in $\{k \in \mathbb{C} : \mathrm{Re}\,(\omega(k)) < 0\}$. Data with faster decay gives more freedom to

deform the contour. We consider data with exponential decay rate $\delta > 0$, defined by

$$C_\delta^m = \left\{ f \in C^m([0,\infty)),\ \exists \delta' > \delta,\ \text{such that} \sup_{x\in[0,\infty)} e^{\delta' x} \left| f(x) \right| < \infty \right\}.$$

Remark 3. *For $f \in C_\delta^m$, we have $\int_0^\infty e^{\delta'' x} \left| f(x) \right| dx < \infty$ with $\delta'' = \frac{\delta' + \delta}{2} > \delta$. The boundedness is introduced for convenience in the proofs in the appendix and the implied integrability is used to allow deformation of contours not just in the interior of regions but also to their boundaries.*

If the initial condition $q_0 \in C_\delta^m$, then $\hat{q}_0$ is analytic and bounded in a open set containing $\{k \in \mathbb{C} : \mathrm{Im}\,(k) \leq \delta\}$. Therefore contour integrals of $\hat{q}_0(k)$ can be deformed inside a larger region. When the contours get close to the boundary of regions in which they can be deformed, highly oscillatory integrals of the form

$$S(x,t) = \int_{k_0}^{\infty} f(k) e^{\theta(k;x,t)} dk, \tag{3.3}$$

appear. Here $f(k)$ is, in general, not analytically extendable off the real axis, $k = k_0$ is the critical point of $\theta(k;x,t)$ and $\omega(k) \in i\mathbb{R}$. This integral is highly oscillatory when the parameters x, t are large, and therefore with traditional numerical quadrature methods the cost to achieve a desired accuracy increases as x, t increase. Fortunately, there are methods specific to highly oscillatory integrals, such as Filon-type and Levin-type methods, that are more accurate as oscillations increase, with a fixed number of evaluations of the integrand. Hence it is still possible to attain uniform accuracy without increasing computational cost. Readers can check Section 3.3 in [49] which has a nice and concise description of how Levin's method works. On the other hand, unlike in the method of steepest descent, the global error over all x, t does not, in general, decay spectrally. While we do compute solutions at arbitrarily large x, t with increasing accuracy as x, t increase, improvements over our methodology in the computation of integrals of the type given in (3.3) will improve the overall efficiency of our method. Some possible directions for the improved evaluation of (3.3) are:

1. Better computational methods for oscillatory integrals that can achieve higher order of accuracy, and

2. Faster solvers that can handle more nodes/modes in Levin-type methods like the ultraspherical polynomial spectral method [59].

We emphasize that our work focuses on the integrals from the UTM and therefore we focus on analyticity and decay of the integrands and possible contour deformations. A complete discussion of the treatment of (3.3) is beyond the scope of this project as any improvement is not only relevant to the NUTM but is also worth studying for its own sake.

In order to make use of the path of steepest descent to obtain exponential localization, we avoid computing the solution with arbitrarily small x or t. Hence in discussion about uniform accuracy, we assume $x, t \geq c$ for some constant $c > 0$. We choose $c = 0.1$ in most examples for convenience.

Remark 4. *The NUTM is less efficient for small x or t. We can use extrapolation and Taylor expansions to get $q(x,t)$ with small x or t [71]. Traditional time-stepping methods can be powerful and convenient if the number of time steps is small.*

Methods for oscillatory integrals are also needed for computing the transforms $\hat{q}, \tilde{g}$. These transformed data are Fourier-type integrals that can be handled efficiently by Levin's method. In Figure 3.1, the absolute errors for $\hat{q}_0(x+i)$ for $q_0(x) = e^{-2x}$ are plotted. The number of collocation points $N = 40$ is the same for Levin's method and for Clenshaw-Curtis quadrature. The values start to diverge for large x for Clenshaw-Curtis quadrature when the oscillations are under resolved but Levin's method provides reliable approximations with decreasing errors.

3.3 The heat equation on the half-line

We consider the heat equation on the half-line,

$$q_t = q_{xx}, \quad t > 0, \quad x > 0, \tag{3.4}$$

with Dirichlet boundary data $q(0,t) = g_0(t)$ and initial data $q(x,0) = q_0(x)$. The dispersion relation for the heat equation is $\omega(k) = k^2$. The initial data q_0 is assumed to be in C^∞_δ

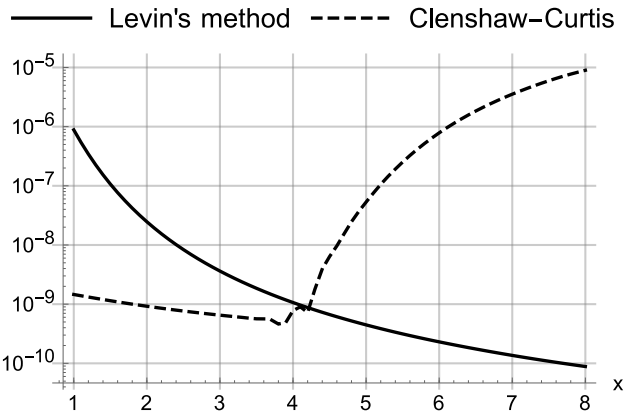

Figure 3.1: The absolute errors for the computation of $\hat{q}_0(x+i)$ for $x \in [1,8]$. The curves are computed using Clenshaw-Curtis quadrature (dashed) and Levin's method (solid). Both methods use a fixed number of nodes $N = 40$. The initial data is $q_0(x) = e^{-2x}$.

for some $\delta > 0$ and the boundary data g_0 is assumed to be in C^∞_γ for some $\gamma > 0$. The smoothness of $q_0,\ g_0$ allows us to compute the transformed data $\hat{q},\ \tilde{g}$ accurately. The rate of decay affects the regions where the deformation of the integration path is allowed. The same methodology can still be applied, with less efficiency and accuracy, when weaker conditions are satisfied.

Remark 5. *It is possible to deal with non-decaying boundary data when the asymptotics of the data is known and can be handled by some other method. The UTM for linear PDEs with piecewise-constant data is studied in [71]. Since the equation is linear, if the data is given as a superposition of data, it may then be beneficial to obtain the solution of the full problem as a superposition of solutions corresponding to individual pieces of data. For instance, suppose* $g_0(t) = h_1 + h_2(t)$ *where* h_1 *is a constant and* $h_2 \in C^\infty_\delta$. *The transform* $\hat{h}_1(k,\infty) = -1/k^2$ *is a meromorphic function in* $\mathbb{C}$ *and there is no restriction about where the integral contour for* $\hat{h}_1(k,\infty)$ *can be deformed if the residue is collected correctly. The full solution is easily obtained by superimposing the NUTM solutions for the problems corresponding to* h_1 *and* h_2 *separately.*

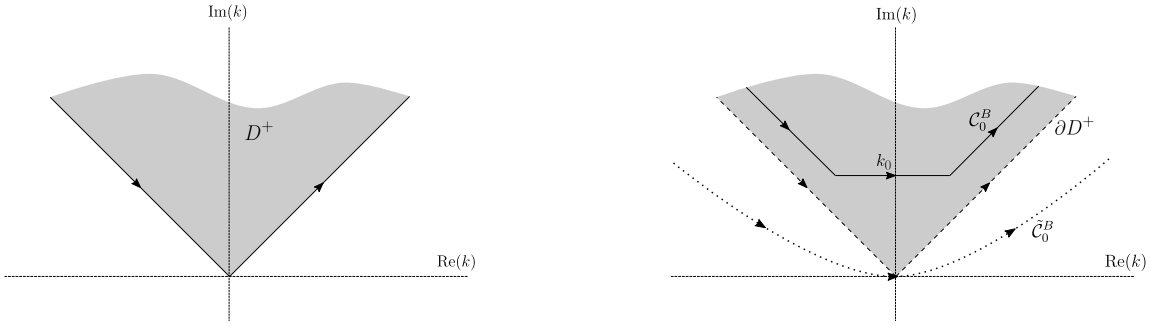

(a) (b)

Figure 3.2: Regions for the heat equation. Panel (a) shows the region $D^+ = \{\mathrm{Re}\,(k^2) < 0\} \cap \mathbb{C}^+$. Panel (b) shows different integral paths for B_0: (i) ∂D^+: the undeformed contour (dashed), (ii) $\mathcal{C}_0^B$: the deformed contour across the saddle point k_0 (solid), and (iii) $\tilde{\mathcal{C}}_0^B$: the deformed contour used in [30] (dotted).

3.3.1 The solution formula from the unified transform method

The solution to the heat equations on the half-line with Dirichlet boundary condition is given by [35]

$$q(x,t) = \frac{1}{2\pi}\int_{-\infty}^{\infty} e^{ikx-\omega(k)t}\hat{q}_0(k)dk - \frac{1}{2\pi}\int_{\partial D^+} e^{ikx-\omega(k)t}\left[\hat{q}_0(-k) + 2ik\tilde{g}_0(\omega(k),t)\right]dk, \quad (3.5)$$

where the contour $\partial D^+ = \{re^{i\pi/4} : r \in [0,\infty)\} \cup \{re^{3i\pi/4} : r \in [0,\infty)\}$ is the boundary of the region $D^+ = \{(re^{iu}) : r \in (0,\infty), u \in (\pi/4, 3\pi/4)\}$, shown in Figure 3.2a. The transformed data $\hat{q}_0(k)$ and $\tilde{g}_0(\omega(k),t)$ are defined by (3.2b) and (3.2c) respectively.

Using the classical sine transform [23], a different representation of the solution is

$$q(x,t) = \frac{2}{\pi}\int_0^{\infty} e^{-\omega(k)t}\sin(kx)\left[\sin(ky)q(y,0)dy - k\tilde{g}_0(\omega(k),t)\right]dk. \quad (3.6)$$

The equivalence of the expressions is shown by deforming the contour of (3.5) back to the real line. The reason we do not work with (3.6) is twofold:

1. Deforming the contour back to the real axis is possible only when classical transforms exist. Generally speaking, classical transforms do not exist for dispersive equations.

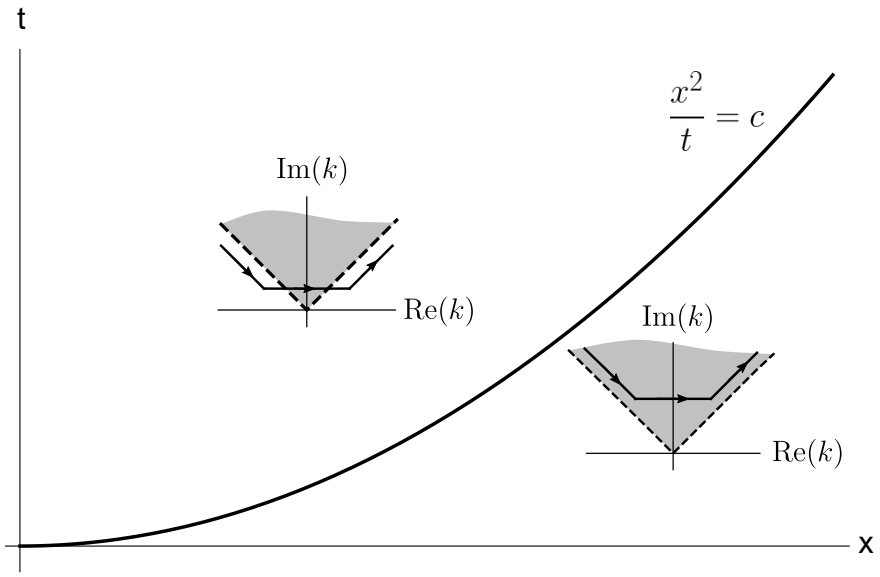

Figure 3.3: Deformed contours for the heat equation. Depending on the values of (x, t), the deformed contour for B_0 can be inside or outside of ∂D^+. Solid lines represent the deformed contours. Dashed lines give ∂D^+, where D^+ is the shaded region. See Section 3.3.2 for a detailed description of these deformations.

2. It is more straightforward to apply the method of steepest descent numerically to (3.5) than it is to (3.6).

3.3.2 Deformations of contours based on the method of steepest descent

We write the solution (3.5) as

$$q(x,t) = I_1 + I_2 + B_0, \tag{3.7}$$

where

$$\begin{aligned} I_1 &= \frac{1}{2\pi}\int_{-\infty}^{\infty} e^{ikx-\omega(k)t}\hat{q}_0(k)dk, \\ I_2 &= -\frac{1}{2\pi}\int_{\partial D^+} e^{ikx-\omega(k)t}\hat{q}_0(-k)dk, \\ B_0 &= -\frac{1}{2\pi}\int_{\partial D^+} e^{ikx-\omega(k)t}2ik\tilde{g}_0(\omega(k),t)dk. \end{aligned}$$

The associated deformed contours for I_1, I_2 and B_0 will be defined by $\mathcal{C}_1^I, \mathcal{C}_2^I$ and $\mathcal{C}_0^B$ respectively in the following sections. In [30], for the FCM, the deformed contour $\tilde{\mathcal{C}}_0^B$ is independent of (x,t), and is the same for all three integrals I_1, I_2 and B_0. The contour $\tilde{\mathcal{C}}_0^B$ is a hyperbola parameterized by $s \in \mathbb{R}$, shown in Figure 3.2,

$$k(s) = i\sin(\pi/8 - is). \tag{3.8}$$

This contour $\tilde{\mathcal{C}}_0^B$ is also used in [20, 36, 61] for different types of advection-diffusion equations. There are two major drawbacks of using $\tilde{\mathcal{C}}_0^B$: (i) the integrands of I_1, B_0 are not defined on all of $\tilde{\mathcal{C}}_0^B$, and (ii) the evaluation of the integral along $\tilde{\mathcal{C}}_0^B$ quickly loses accuracy when t increases as it does not follow the direction of steepest descent and large oscillations and potential growth destroy accuracy. To fix these issues with FCMs, we use different deformations of the contours for I_0, I_1 and B_0 that depend on (x,t) and the contours are deformed to follow the direction of steepest descent as much as possible, see Figure 3.3.

I_1: The integral involving $\hat{q}_0(k)$

The phase function in the integrand is

$$\theta(k;x,t) = ikx - \omega(k)t = ikx - k^2 t. \tag{3.9}$$

There is one saddle point $k_0 = ix/2t$ where $\theta'(k_0;x,t) = 0$ on the imaginary axis. The phase function $\theta(k;x,t)$ can be rewritten as

$$\theta(k;x,t) = ikx - k^2 t = -t(k - ix/2t)^2 - x^2/4t.$$

The direction of steepest descent, along which the magnitude of $e^{\theta(k;x,t)}$ decays exponentially, is horizontal. If $\mathrm{Im}(k_0) = x/2t > \delta$, the contour cannot be deformed to pass through the saddle point k_0 because the transform of the initial data $q \in C^\infty_\delta$ is only guaranteed to be defined for $\mathrm{Im}(k) \leq \delta$. However, there is exponential decay in the integrand when the path is along the horizontal line $\mathrm{Im}(k) = \delta$ since $t > 0, x > 0$. Hence the deformed path that we choose is a horizontal line $\mathcal{C}_1^I = \{k \in \mathbb{C} : \mathrm{Im}\,(k) = h\}$, with $h = \min(\delta, x/2t)$.

$$I_1 = -\frac{1}{2\pi}\int_{-\infty}^{\infty} e^{ikx-\omega(k)t}\hat{q}_0(k)dk = -\frac{1}{2\pi}\int_{\mathcal{C}_1^I} e^{ikx-k^2t}\hat{q}_0(k)dk.$$

The uniform convergence of Clenshaw-Curtis quadrature applied to I_1 for $x, t \geq c$ is established in Theorem 4 (Appendix), after proper truncation and rescaling.

I_2: The integral involving $\hat{q}_0(-k)$

Similar analysis can be applied to I_2 in (3.5). Here

$$I_2 = -\frac{1}{2\pi}\int_{\partial D^+} e^{ikx-\omega(k)t}\hat{q}_0(-k)dk.$$

Because $\hat{q}_0(-k)$ is analytic and bounded for $\mathrm{Im}(k) > -\delta$, we can deform the contour ∂D^+ to the horizontal line passing through $k_0 = ix/2t$ defined by $\mathcal{C}_2^I = \{k \in \mathbb{C} : \mathrm{Im}\,(k) = x/2t\}$,

$$I_2 = -\frac{1}{2\pi}\int_{\mathcal{C}_2^I} e^{ikx-\omega(k)t}\hat{q}_0(-k)dk.$$

The uniform convergence of Clenshaw-Curtis quadrature applied to I_2 for $x, t \geq c$ is established in Theorem 4 (Appendix), after proper truncation and rescaling.

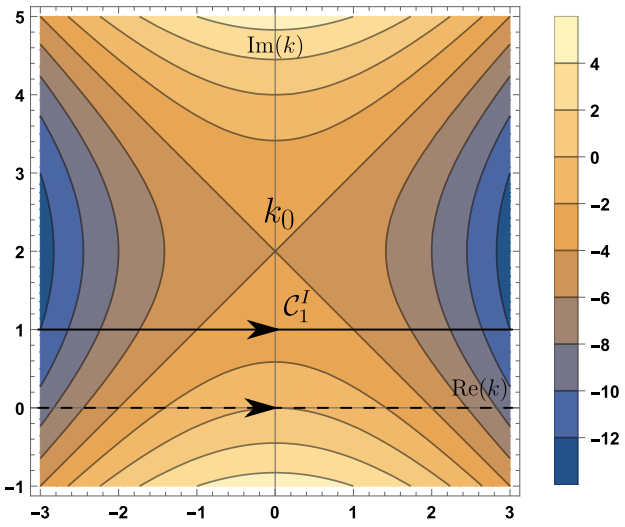

Figure 3.4: The deformed horizontal contour $\mathcal{C}_1^I$ (solid) passing through i with $\delta = 1$, $x = 4, t = 1$, $k_0 = 2i$. The undeformed contour (dashed). The background contour plot shows the level sets of $\mathrm{Re}(\theta(k, x, t))$. The integrand of I_1 is analytic for $\mathrm{Im}\,(k) < 1$ when $q_0 \in C_1^\infty$.

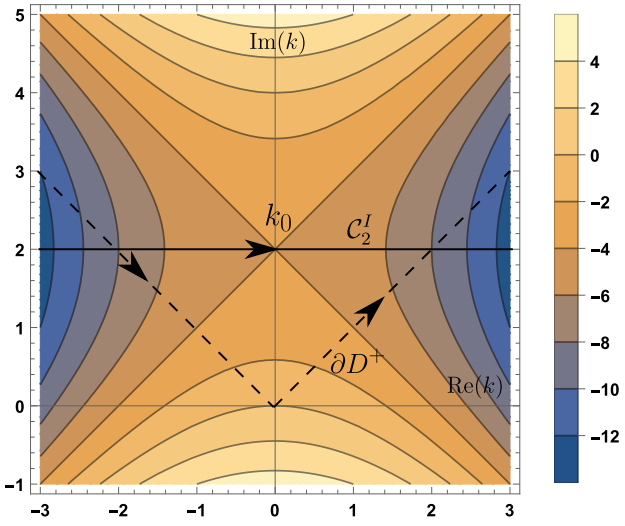

Figure 3.5: The deformed horizontal contour for I_2 (solid) through $k_0 = 2i$ with $\delta = 1$, $x = 4, t = 1$. The undeformed contour (dashed). The background contour plot shows the level sets of $\mathrm{Re}(\theta(k, x, t))$. The integrand of I_2 is analytic for $\mathrm{Im}\,(k) > -1$. The dashed line is the undeformed contour ∂D^+.

B_0: The integral of the transform of boundary data $\tilde{g}_0(\omega(k),t)$

The integral B_0 in (3.5) containing the boundary data is more complicated compared to the integrals I_1, I_2. There are two important factors that require special treatment:

1. The parameter t appears both in the exponential and in the transformed boundary data $\tilde{g}(\omega(k),t)$ and therefore the phase $\theta(k,x,t)$ alone does not describe the decay of the integrand in B_0.

2. The evaluation of $e^{-k^2t}\tilde{g}(\omega(k),t)$ is ill-conditioned due to the oscillations and growth in $\tilde{g}(\omega(k),t)$ canceling those from the exponential.

Example 1. *To get a more concrete understanding, consider $g_0(t) = e^{-t}$. The transform is*

$$\tilde{g}_0(\omega(k),t) = \int_0^t e^{k^2s}e^{-s}ds = \frac{1}{k^2-1}\left(e^{(k^2-1)t}-1\right).$$

Since $g_0(s) = e^{-s}$ is bounded on the finite interval $0 \le s \le t$, the transformed data $\tilde{g}_0(\omega(k),t)$ is an entire function of k with removable poles at $k = \pm 1$. The integrand of B_0 contains two terms,

$$e^{ikx-\omega(k)t}2ik\tilde{g}_0(\omega(k),t) = \frac{ike^{ikx-t}}{\pi(k^2-1)} - \frac{ike^{ikx-k^2t}}{\pi(k^2-1)}. \tag{3.10}$$

The second term follows the horizontal direction of steepest descent but the first term is not exponentially localized on horizontal lines in the complex k-plane. Although the integral of the first term on the ∂D^+ is zero, it is not possible to separate the two terms, in general, for all k.

General case. We write the transform $\tilde{g}_0(k,t)$ as

$$\tilde{g}_0(\omega(k),t) = \int_0^t e^{k^2s}g_0(s)ds = -\int_t^\infty e^{k^2s}g_0(s)ds + \int_0^\infty e^{k^2s}g_0(s)ds,$$

for $k \in D^+$. Therefore the integrand in B_0 is

$$e^{ikx-k^2t}\tilde{g}_0(\omega(k),t) = -e^{ikx}\int_0^\infty e^{k^2s}g_0(s+t)ds + e^{ikx-k^2t}\tilde{g}_0(\omega(k),\infty). \tag{3.11}$$

The two terms on the right-hand side of (3.11) behave the same as the two terms in (3.10). Because $\tilde{g}_0(\omega(k), \infty)$ is in general not defined outside D^+, a separation only exists inside D^+. Without splitting the two terms, to get exponential decay for both terms, the contour ∂D^+ is deformed to $\mathcal{C}_0^I$ passing through the saddle point horizontally and turns up when the second term in the integrand is negligible, see Figure 3.6. The corner point $k_1 = \pm L + ix/2t$ is determined by $L = \max(L_1, \sqrt{\gamma})$ with specified tolerance ϵ where $\left|e^{-L_1^2 t}\right| = \epsilon$ characterizes the exponential decay and $\sqrt{\gamma}$ allows the oblique segment to be away from $k = 0$. With this choice of contour, the exponential part in the second term decays exponentially along the horizontal segment and keeps the same magnitude along the oblique segment while the exponential part in the first term keeps the same magnitude along the horizontal segment and decays exponentially along the oblique segment. Uniform accuracy is shown in Theorem 5 (Appendix) after proper truncation and rescaling.

Remark 6. *For boundary data that are not exponentially decaying, the transforms $\tilde{g}_0(\omega(k), \infty)$ are only defined in D^+ in Figure 2. As a result, $\tilde{g}_0(\omega(k), t)$ for large t is highly ill-conditioned when k leaves D^+. However, staying inside D^+ requires retaining more oscillations. In the limit $t \to \infty$, the saddle point $x/(2t)$ approaches the corner of D^+, which further restricts contour deformations and makes achieving uniform accuracy more difficult.*

3.3.3 A numerical example

With these deformed contours, we can numerically evaluate the integrals efficiently for arbitrarily large values of the parameters x, t. Figure 3.7 shows the solution to the heat equation with initial and boundary data $q_0(x) = e^{-x}$, $g_0(t) = e^{-t}$. Although exact transforms can be obtained for these choices of data, in the rest of the chapter, they are only used for computing the errors and our NUTM does not make use of the formulas.

To demonstrate the uniform accuracy for large x, t, we plot the absolute errors E_{NUTM} and E_{FCM} along 3 different curves (a) $t = 0.1$, (b) $x = 0.1$, and (c) $t = x^2$ in Figure 3.8. The error E_{NUTM} is obtained using the contours $\mathcal{C}_1^I, \mathcal{C}_2^I$ and $\mathcal{C}_0^B$. The error E_{FCM} is obtained

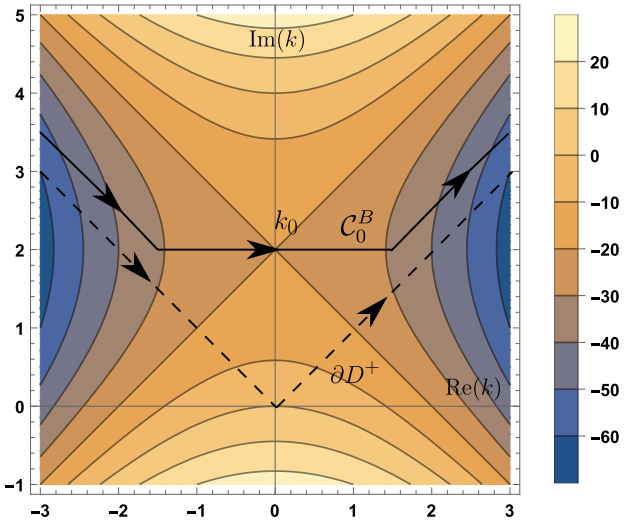

Figure 3.6: The undeformed contour ∂D^+. The solid line gives the deformed contour $\mathcal{C}_0^I$ of I_0 that goes through $k_0 = 2i$ and turns to rays parallel to ∂D^+ with $x = 20, t = 5$. The integrand of I_0 is entire. The background contour plot shows the level sets of $\mathrm{Re}(\theta(k, x, t))$.

using the contour $\tilde{\mathcal{C}}_0^B$ in (3.8) [30]. The initial and boundary conditions are $q_0(x) = e^{-10x}$, $g_0(t) = e^{-10t}$ to allow deformation in a larger region. The number of collocation points $N = 120$ is the same for both methods. This is a coarse grid for the integrals with the errors approximately 10^{-3} when $s = 0.1$ is small but it shows the efficiency of the NUTM as s grows. The true solution is computed using Mathematica's built-in numerical integration routine `NIntegrate` along the undeformed contour ∂D^+ with sufficient recursions and precision. This is time consuming if the transforms of the initial and boundary data need to be computed. The truncation tolerance is set to 10^{-13} for determining the truncation of the deformed path. This value of the truncation tolerance is chosen so that it is small enough to show the trend of the errors when x, t vary and the truncation is not affected by the rounding errors. These settings are the same for other examples in the chapter unless stated otherwise.

The absolute error E_{NUTM} decreases in all cases as x, t grow while E_{FCM} grows when t increases. This can be explained simply by the fact that the contour used in the FCM does not follow the steepest descent path. Furthermore, even when t is fixed in Figure 3.8(a),

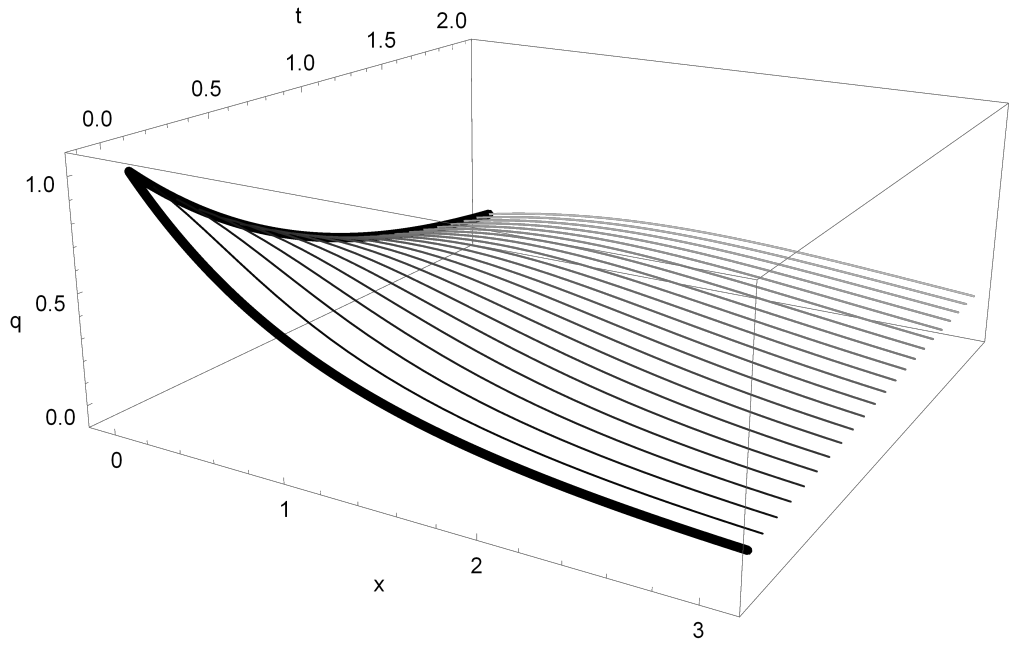

Figure 3.7: The solution to the heat equation (3.4) with exponential decay initial and boundary data $q(x,0) = e^{-x}$, $q(0,t) = e^{-t}$. The bold curves are the initial and boundary conditions.

E_{FCM} decreases slower than E_{NUTM}. On the other hand, E_{NUTM} increases relative to the true solution. This is mainly due to the fact that the magnitude of the solution is smaller than the truncation tolerance for $x > 5$ at which point the numerical solution has almost all contours truncated. In Figure 3.8(b-c), E_{NUTM} maintains good relative accuracy. In Figure 3.8(c), E_{NUTM} starts with a larger error because $t = s^2 = 0.01$ is very small and close to the initial condition which requires more nodes to produce the same order of errors compared with the other two starting from $t = 0.1$. As both the FCM and the NUTM are implemented with spectral methods, for fixed x and t, both methods are spectrally accurate.

Remark 7. *As can be seen in (3.10) and (3.11), there is large cancellation in the exponentials. To avoid potential overflow/underflow problems, we use $\hat{g}_0(\omega(k), T)$ defined by*

$$\hat{g}_0(\omega(k), T) = e^{-\omega(k)T}\tilde{g}_0(\omega(k), T) = \int_0^T e^{\omega(k)(s-T)} g_0(s) ds. \tag{3.12}$$

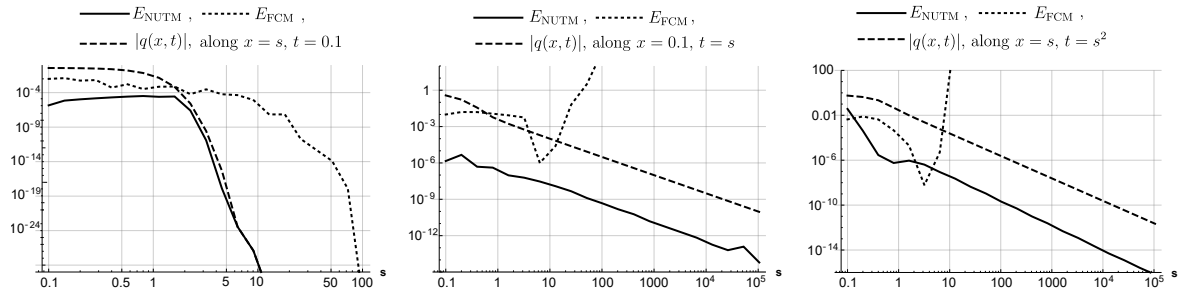

(a) (b) (c)

Figure 3.8: The absolute errors of the numerical solution to the heat equation with initial condition $q_0(x) = e^{-10x}$ and boundary condition $g_0(t) = e^{-10t}$ along (a) $x = s, t = 0.1$, (b) $x = 0.1, t = s$, (c) $x = s, t = s^2$ for $s \in [0.1, 10^5]$. The error E_{NUTM} is obtained using the contours $\mathcal{C}_1^I, \mathcal{C}_2^I$ and $\mathcal{C}_0^B$. The error E_{FCM} is obtained using the contour $\tilde{\mathcal{C}}_0^B$ in Figure 3.6. The absolute value of the solution $|q(x,t)|$ is also plotted with dashed lines for reference. The FCM loses accuracy as t grows while E_{NUTM} decreases in all cases as parameters increase.

3.4 The linear Schrödinger equation on the half-line

Next, we consider a dispersive example, the linear Schrödinger (LS) equation:

$$iq_t = -q_{xx}, \quad x > 0, \ t > 0, \tag{3.13}$$

with Dirichlet boundary data $g_0 \in C_\gamma^\infty$ and initial data $q_0 \in C_\delta^\infty$.

3.4.1 The solution formula from the unified transform method

The dispersion relation for (3.13) is $\omega(k) = ik^2$. Define the transform of the initial data $\hat{q}_0$ and the transform of the Dirichlet boundary data $\tilde{g}_0$ by (3.2b) and (3.2c). The UTM provides the solution in terms of the following contour integrals [23],

$$q(x,t) = \frac{1}{2\pi}\int_{-\infty}^{\infty} e^{ikx-\omega(k)t}\hat{q}_0(k)dk - \frac{1}{2\pi}\int_{\partial D^+} e^{ikx-\omega(k)t}\left[\hat{q}_0(-k) - 2k\tilde{g}_0(\omega(k),t)\right]dk, \tag{3.14}$$

where the contour ∂D^+ is the positively oriented boundary of the first quadrant $D^+ = \{k \in \mathbb{C} : \text{Re}\,(k) \geq 0, \text{Im}\,(k) \geq 0\}$. With the assumption of the decay of $g_0(t)$, the contour can be deformed to the lower-half plane inside $\tilde{D} = \{k \in \mathbb{C} : \text{Re}\,(k^2) < \gamma\}$ as in Figure 3.9. But

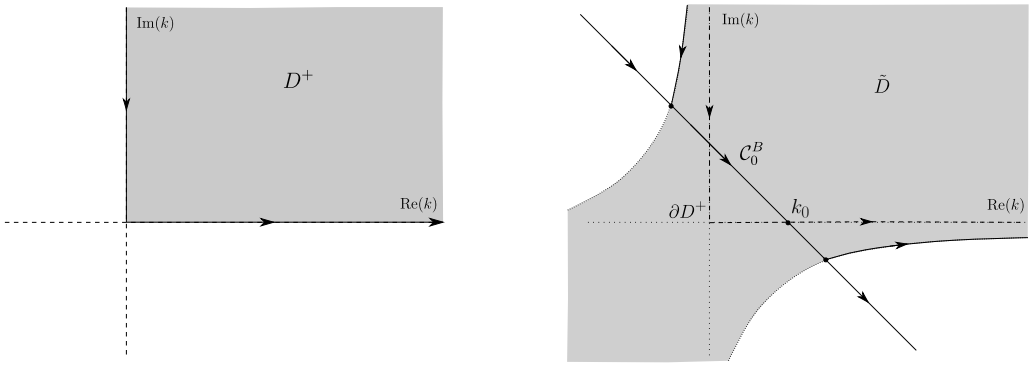

(a) (b)

Figure 3.9: Regions for the LS equation. Panel (a) shows the region $D^+ = \{k \in \mathbb{C}^+ : \mathrm{Re}\,(k^2) < 0\}$. Panel (b) shows $\tilde{D} = \{k \in \mathbb{C} : \mathrm{Re}\,(k^2) < \gamma\}$ and a schematic of the deformed contour from ∂D^+ to $\mathcal{C}_0^B$ for B_0 in (3.15), see Section 3.4.2 for details of the deformation.

this is not enough to completely eliminate the oscillations. In general, other methods for oscillatory integrals are required when t is not sufficiently large or the saddle point k_0 has large modulus.

3.4.2 Deformations of the contours based on the method of steepest descent

We separate the different integrals in the solution formula (3.14),

$$q(x,t) = I_0 + I_1 + B_0, \tag{3.15}$$

where

$$\begin{aligned} I_0 &= \frac{1}{2\pi}\int_{-\infty}^{\infty} e^{ikx-\omega(k)t}\hat{q}_0(k)dk, \\ I_1 &= -\frac{1}{2\pi}\int_{\partial D^+} e^{ikx-\omega(k)t}\hat{q}_0(-k)dk, \\ B_0 &= \frac{1}{2\pi}\int_{\partial D^+} e^{ikx-\omega(k)t}2k\tilde{g}_0(\omega(k),t)dk. \end{aligned}$$

I_1: integral with the transform of the initial data

The phase function in I_1 is

$$\theta(k;x,t) = ikx - \omega(k)t = ikx - ik^2t. \tag{3.16}$$

There is one saddle point $k_0 = x/2t$ on the positive real axis satisfying $\theta'(k_0;x,t) = 0$. Near the saddle point k_0,

$$\theta(k;x,t) = ikx - ik^2t = -it(k - x/2t)^2 + ix^2/4t.$$

The directions of steepest descent are $-\pi/4$ and $3\pi/4$. Similar to the case of the heat equation, the transformed initial data $\hat{q}_0(k)$ is bounded and analytic in $\mathrm{Im}\,(k) < \delta$ when $q_0 \in C^\infty_\delta$. Hence we choose the deformed contour $\mathcal{C}_1^I = \{a + k_0 + ib : a \in (-\infty, -\delta), b = \delta\} \cup \{a + k_0 - ia : a \in [-\delta, \infty)\}$ to be a horizontal ray with height $\mathrm{Im}(k) = \delta$ and a straight-line segment with slope -1 passing through the saddle point as shown in Figure 3.10. The integral I_1 becomes

$$I_1 = \frac{1}{2\pi}\int_{\mathcal{C}_1^I} e^{ikx - ik^2t}\hat{q}_0(k)dk.$$

I_2: integral with the transform of the initial data $\hat{q}_0(-k)$

Similar analysis can be applied to I_2 with $\hat{q}_0(-k)$ in (3.14). Since the transform $\hat{q}_0(-k)$ is analytic and bounded for $\mathrm{Im}\,(k) > -\delta$, we can deform the contour ∂D^+ to

$$\mathcal{C}_2^I = \{a + k_0 - ia : a \in (-\infty, \delta)\} \cup \{a + k_0 - ib : a \in [\delta, \infty), b = \delta\},$$

see Figure 3.11. Therefore, I_2 becomes

$$I_2 = -\frac{1}{2\pi}\int_{\mathcal{C}_2^I} e^{ikx - ik^2t}\hat{q}_0(-k)dk.$$

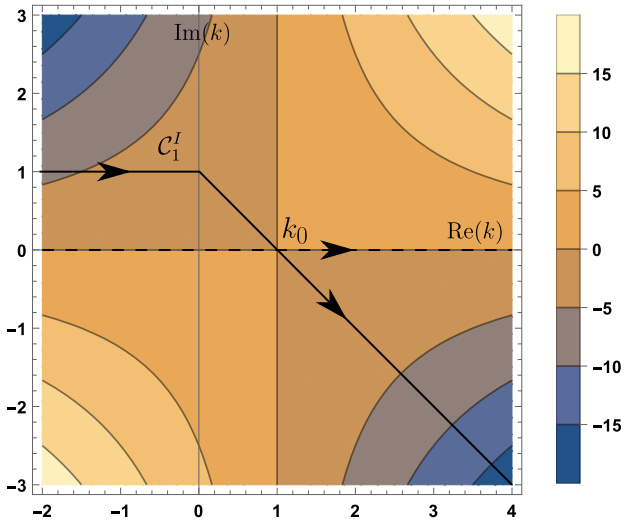

Figure 3.10: The undeformed contour (dashed). The deformed horizontal contour C_1^I (solid) going through $k_0 = 1$, $\delta = 1$, $x = 2, t = 1$. The background contour plot shows the level sets of $\mathrm{Re}(\theta(k, x, t))$. The integrand of I_1 is analytic for $\mathrm{Im}\,(k) < 1$.

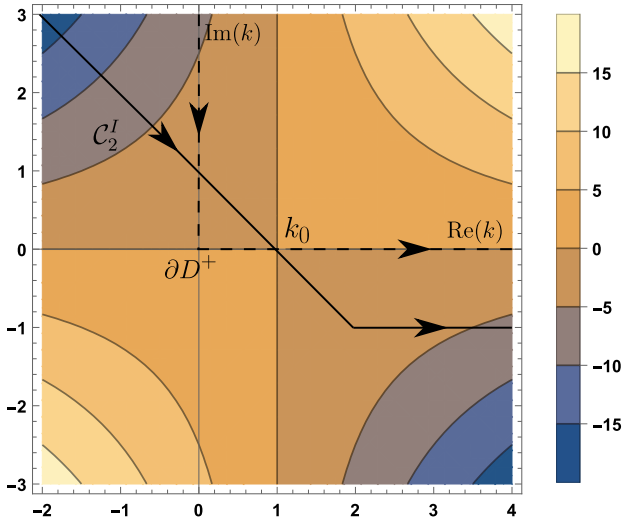

Figure 3.11: The undeformed contour (dashed). The deformed contour for I_2 (solid) going through $k_0 = 1$, $\delta = 1$, $x = 2, t = 1$. The background contour plot shows the level sets of $\mathrm{Re}(\theta(k, x, t))$. The integrand of I_2 is analytic for $\mathrm{Im}\,(k) > -1$.

B_0: integral of the transform of boundary data $\tilde{g}_0(\omega(k),t)$

The issues discussed in Section 3.3.2 also appear in the case of the LS equation. However, now the region where we can deform the contour is restricted. The same decomposition as in (3.11) gives

$$e^{ikx-k^2t}\tilde{g}_0(\omega(k),t) = -e^{ikx}\int_0^\infty e^{k^2s}g_0(s+t)ds + e^{ikx-k^2t}\tilde{g}_0(\omega(k),\infty). \tag{3.17}$$

For generic $g_0(t)$, if the contour of B_0 is along the $-\pi/4$ direction at the saddle point $k_0 = x/2t$, the first term in (3.17) grows exponentially as $x \to \infty$ since $\mathrm{Re}\,(ikx) > 0$. On the other hand, $\tilde{g}_0(\omega(k),\infty)$ may not be extendable outside D^+. With the assumption that $g_0 \in C^\infty_\gamma$, it becomes possible to deform the path to the lower-half plane to obtain some exponential decay. The steps of the deformation are:

1. The region D^+ is extended to $\tilde{D}$. The transformed data $\tilde{g}_0(\omega(k),\infty)$ is analytic in $\tilde{D}$, and continuous up to $\partial\tilde{D}$.

2. The contour ∂D^+ is deformed to $\mathcal{C}^B_{0,a} \cup \mathcal{C}^B_{0,b} \cup \mathcal{C}^B_{0,c}$ as shown in Figure 3.12 where $\mathcal{C}^B_{0,b}$ is the straight-line segment passing through the saddle point along the steepest-descent direction up to $\partial\tilde{D}$ and $\mathcal{C}^B_{0,a}, \mathcal{C}^B_{0,c}$ are the unbounded curved segments along $\partial\tilde{D}$.

3. Using that $e^{ikx-\omega(k)t}\int_t^\infty e^{\omega(k)s}g_0(s)ds$ is bounded and analytic in $\tilde{D}$, we can replace $\tilde{g}_0(\omega(k),t)$ with $\tilde{g}_0(\omega(k),\infty)$ using Jordan's lemma,

$$B_0 = \frac{1}{2\pi}\int_{\partial D^+} e^{ikx-\omega(k)t}2k\tilde{g}_0(\omega(k),t)dk = \frac{1}{2\pi}\int_{\mathcal{C}^B_{0,a}\cup\mathcal{C}^B_{0,b}\cup\mathcal{C}^B_{0,c}} e^{ikx-\omega(k)t}2k\tilde{g}_0(\omega(k),\infty)dk. \tag{3.18}$$

4. The integral along $\mathcal{C}^B_{0,a}$ is decomposed into two parts to maximize decay along the steepest descent direction:

$$\int_{\mathcal{C}^B_{0,a}} e^{ikx-\omega(k)t}2k\tilde{g}_0(\omega(k),\infty)dk = \int_{\mathcal{C}^B_{0,d}} e^{ikx-\omega(k)t}2k\tilde{g}_0(\omega(k),t)dk + \int_{\mathcal{C}^B_{0,a}} e^{ikx-\omega(k)t}2k\tilde{g}^c_0(\omega(k),t)dk,$$

where

$$\tilde{g}_0^c(\omega(k),t) = \int_t^\infty e^{\omega k s} g_0(s) ds,$$

is the complementary transform of g_0.

5. The integral along $\mathcal{C}^B_{0,c}$ is decomposed into two parts:

$$\int_{\mathcal{C}^B_{0,c}} e^{ikx-\omega(k)t} 2k\tilde{g}_0(\omega(k),\infty)dk = \int_{\mathcal{C}^B_{0,c}} e^{ikx-\omega(k)t} 2\left(k\tilde{g}_0(\omega(k),\infty) - k_0\tilde{g}_0(\omega(k_0),\infty)\right) dk + \int_{\mathcal{C}^B_{0,e}} e^{ikx-\omega(k)t} 2k_0\tilde{g}_0(\omega(k_0),\infty)dk.$$

The second integral on the right-hand side is deformed to follow the direction of steepest descent.

6. With the above steps, we obtain

$$\begin{aligned} B_0 =& \frac{1}{2\pi}\int_{\mathcal{C}^B_{0,a}} e^{ikx-\omega(k)t} 2k\tilde{g}_0^c(\omega(k),t)dk + \frac{1}{2\pi}\int_{\mathcal{C}^B_{0,d}} e^{ikx-\omega(k)t} 2k\tilde{g}_0(\omega(k),tdk \\ &+ \frac{1}{2\pi}\int_{\mathcal{C}^B_{0,b}} e^{ikx-\omega(k)t} 2k\tilde{g}_0(\omega(k),\infty)dk \\ &+ \frac{1}{2\pi}\int_{\mathcal{C}^B_{0,c}} e^{ikx-\omega(k)t} \left[2k\tilde{g}_0(\omega(k),\infty) - 2k_0\tilde{g}_0(\omega(k_0),\infty)\right] dk \\ &+ \frac{1}{2\pi}\int_{\mathcal{C}^B_{0,e}} e^{ikx-\omega(k)t} 2k_0\tilde{g}_0(\omega(k_0),\infty)dk. \end{aligned}$$

Using the deformed contour, for large x, t , the integral is exponentially localized near the saddle point on $\mathcal{C}^B_{0,b}$. When the integrand is not sufficiently small near the endpoints of $\mathcal{C}^B_{0,b}$, the oscillations in the integrand along $\mathcal{C}^B_{0,c}$ and $\mathcal{C}^B_{0,d}$ become important. Most of the potential error comes from the integral along $\mathcal{C}^B_{0,c}$ as the integrand along $\mathcal{C}^B_{0,d}$ has exponential decay from the e^{ikx} factor. The contour $\mathcal{C}^B_{0,c}$ asymptotically approaches the real axis. We use the Levin collocation method [49] for the integrals along $\mathcal{C}^B_{0,c}$ and $\mathcal{C}^B_{0,d}$ to maintain accuracy for large x, t. The rest of the integrals in B_0, as well as those making up I_1 and I_2, are computed using Clenshaw-Curtis quadrature.

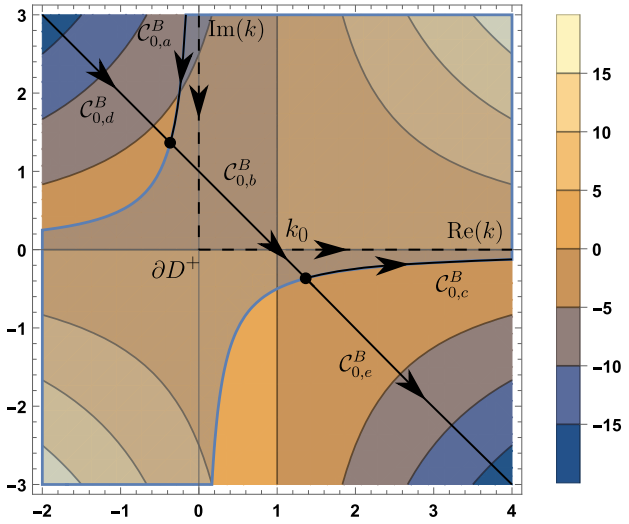

Figure 3.12: The undeformed contour (dashed). The deformed contour for B_0 (solid) through $k_0 = 1$ with $x = 2, t = 1, \gamma = 1$, see Section 3.4.2 for details of the deformation. The background contour plot shows the level sets of $\mathrm{Re}(\theta(k, x, t))$.

3.4.3 A numerical example

Consider the initial condition $q_0(x) = 0$, and the Dirichlet boundary condition $g_0(t) = te^{-t}$. The real part of the solution to (3.13) with this choice of data is shown in Figure 3.13. Dispersive waves quickly emerge from the boundary, becoming more oscillatory for large x. The absolute error and the magnitude of the solution evaluated along (a) $t = 0.1$, (b) $x = 0.1$, (c) $t = x^2$ are shown in Figure 3.14. The errors shown in dotted curves are computed with $N = 20$ collocation points for each part of the contour in B_0 while the errors shown in solid curves are computed with $N = 40$ collocation points. The absolute errors decrease as x, t increase. In Figure 3.14(a), we see that although the initial condition is zero, at $t = 0.1$ the solution $q(x, t)$ only decreases algebraically. This makes traditional time-stepping method inefficient even if we ignore issues related to the highly oscillatory nature of the solution.

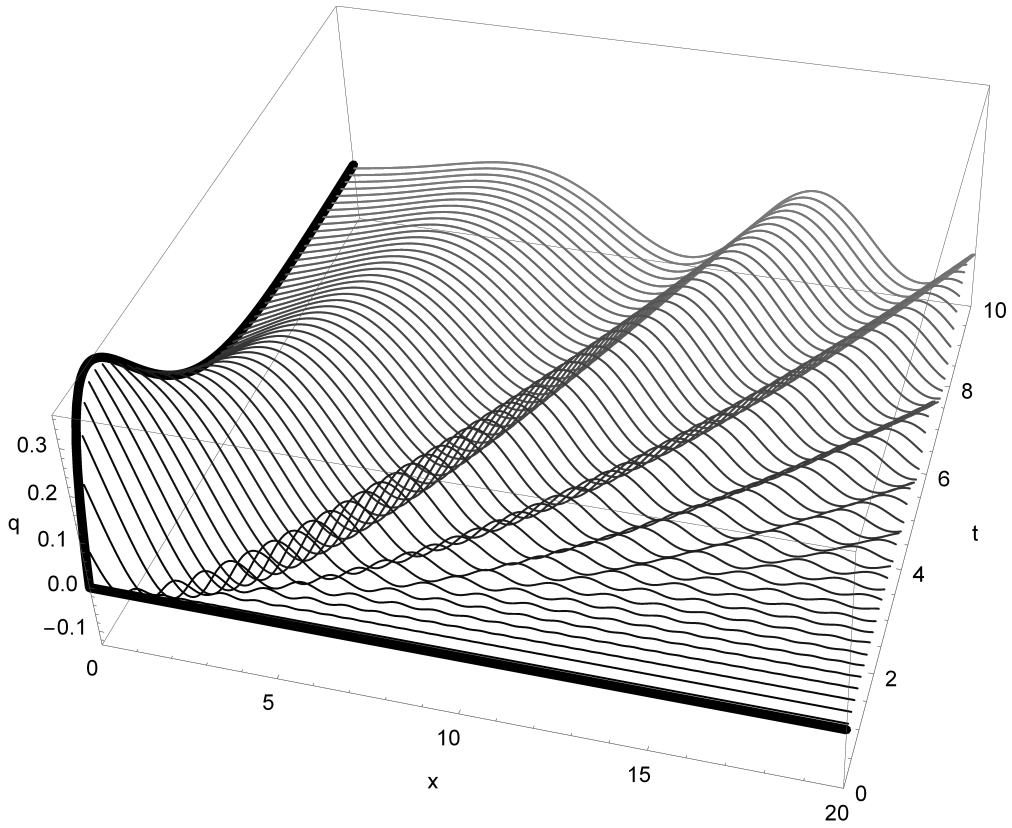

Figure 3.13: The plot of the real part of the solution of the LS equation with $q_0(x) = 0$, $g_0(t) = te^{-t}$. The bold solid curve shows the initial and boundary conditions.

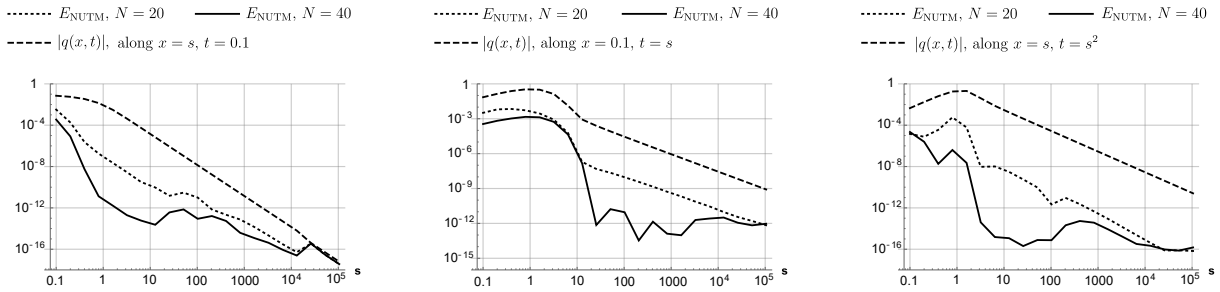

(a) (b) (c)

Figure 3.14: The absolute errors E_{NUTM} of the numerical solution to the LS equation (3.13) along three curves: (a) $x = s, t = 0.1$, (b) $x = 0.1, t = s$, (c) $x = s, t = s^2$ for $s \in [0.1, 10^5]$.

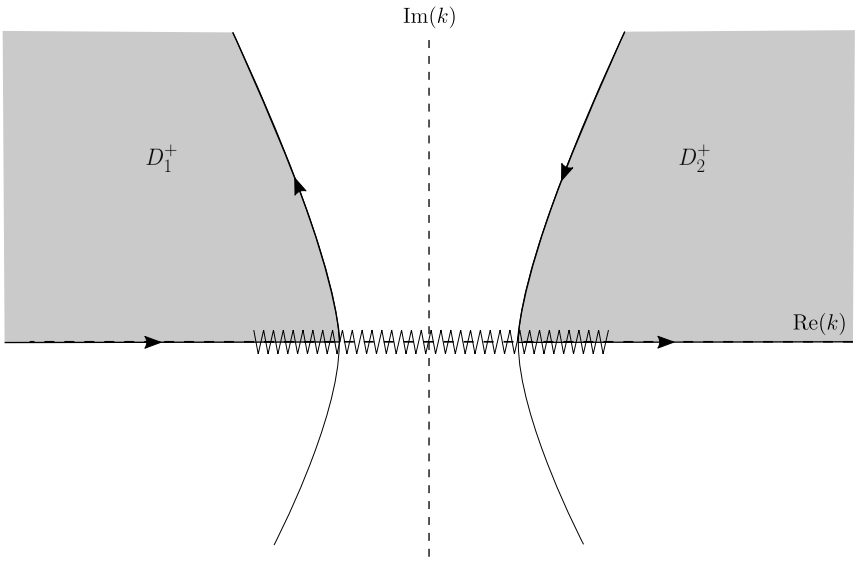

Figure 3.15: The region D^+ for (3.19). The shaded region in the top left is D_1^+. The shaded region in the top right is D_2^+. The branch cut is shown as a jagged line.

3.5 A multi-term third-order PDE on the half-line

The deformations for higher-order equations are more involved and the integrands may have branch points that are fixed by the equation and not by the initial or boundary data. The NUTM is implemented in a systematic way as long as one can solve the PDE using the UTM with additional care for the branch points. Consider a multi-term third-order PDE,

$$q_t = q_x + q_{xxx}, \qquad x > 0,\ t > 0, \tag{3.19}$$

with Dirichlet boundary data $g_0 \in C_\gamma^\infty$, Neumann boundary data $g_1 \in C_\gamma^\infty$ and initial data $q_0 \in C_\delta^\infty$. The dispersion relation is $\omega(k) = -ik + ik^3$ and $D^+ = \{k \in \mathbb{C}^+ : \mathrm{Re}\,(\omega(k)) < 0\} = D_1^+ \cup D_2^+$ as shown in Figure 3.15.

Using the UTM, it is known that the problem requires two boundary conditions at $x =$

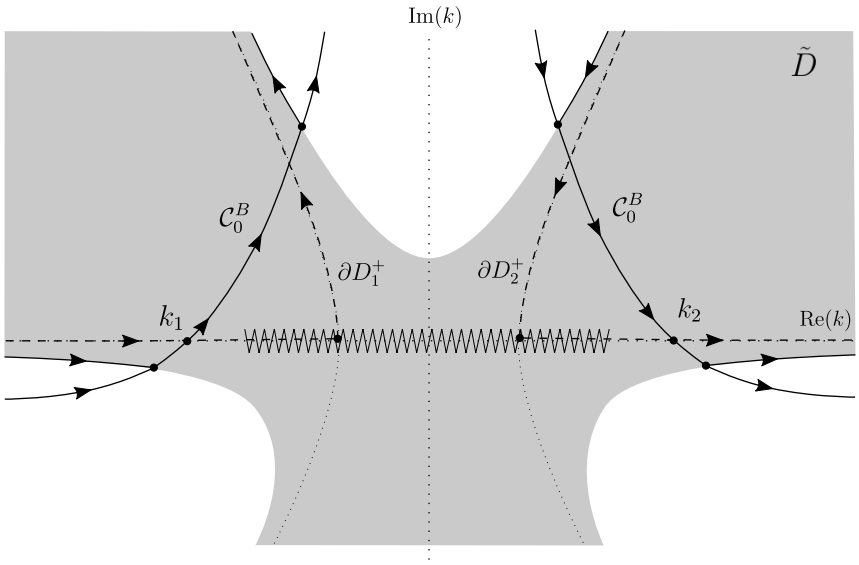

Figure 3.16: The region $\tilde{D}$ and the deformation for B_0 across the saddle points k_1 and k_2. The branch cut is shown as a jagged line.

0 [23]. By solving $\omega(\nu(k)) = \omega(k)$, we find two symmetries of the dispersion relation,

$$\nu_1(k) = (-k - \sqrt{4 - 3k^2})/2,$$
$$\nu_2(k) = (-k + \sqrt{4 - 3k^2})/2,$$

with branch cut $[-2/\sqrt{3}, 2/\sqrt{3}]$. Here, ν_1 is the branch of ν that tends to $(-1/2+i\sqrt{3}/2)k = k\exp(2\pi i/3)$ as $k \to \infty$ and ν_2 is the other branch. The solution formula is given by[3]

$$q(x,t) = I_1 + I_2 + I_3 + B_0 + B_1, \tag{3.20}$$

with

$$I_1 = \frac{1}{2\pi}\int_{-\infty}^{\infty} e^{ikx-\omega(k)t}\hat{q}_0(k)dk,$$
$$I_2 = -\frac{1}{2\pi}\int_{\partial D_1^+} e^{ikx-\omega(k)t}\hat{q}_0(\nu_1(k))dk,$$
$$I_3 = -\frac{1}{2\pi}\int_{\partial D_2^+} e^{ikx-\omega(k)t}\hat{q}_0(\nu_2(k))dk,$$
$$B_0 = -\frac{1}{2\pi}\int_{\partial D_1^+} e^{ikx-\omega(k)t}(\nu_1^2(k) - k^2)\tilde{g}_0(\omega(k),t)dk - \frac{1}{2\pi}\int_{\partial D_2^+} e^{ikx-\omega(k)t}(\nu_2^2(k) - k^2)\tilde{g}_0(\omega(k),t)dk,$$
$$B_1 = -\frac{1}{2\pi}\int_{\partial D_1^+} e^{ikx-\omega(k)t}(ik - i\nu_1(k))\tilde{g}_1(\omega(k),t)dk - \frac{1}{2\pi}\int_{\partial D_2^+} e^{ikx-\omega(k)t}(ik - i\nu_2(k))\tilde{g}_1(\omega(k),t)dk.$$

For convenience, we impose the following initial and boundary conditions to focus on the deformation of B_0,

$$q(x,0) = 0,\ q(0,t) = g_0(t),\ g_0 \in C_\gamma^\infty,\ q_x(0,t) = 0.$$

For inhomogeneous initial and Neumann data, the deformation of B_1 follows the same steps as the deformation of B_0 and the deformations of I_1, I_2, I_3 follow the same steps as in I_1, I_2 in the heat equation or the LS equation case.

---

[3]Although some parts of the contours lie on the branch cut, the integrands are well-defined if the values are taken as limits from the interior of D^+.

3.5.1 Deformations of the contour of B_0 based on the method of steepest descent

With homogeneous initial and Neumann boundary conditions, the solution reduces to

$$q(x,t) = B_0 = B_0|_{D_1^+} + B_0|_{D_2^+},$$

where

$$B_0|_{D_1^+} = -\frac{1}{2\pi}\int_{\partial D_1^+} e^{ikx-\omega(k)t}(\nu_1^2(k)-k^2)\tilde{g}_0(\omega(k),t)dk,$$
$$B_0|_{D_2^+} = -\frac{1}{2\pi}\int_{\partial D_2^+} e^{ikx-\omega(k)t}(\nu_2^2(k)-k^2)\tilde{g}_0(\omega(k),t)dk.$$

The phase function in B_0 is

$$\theta(k;x,t) = ikx - \omega(k)t = ikx - (-ik+ik^3)t.$$

There are two saddle points $k_{1,2} = \pm\sqrt{x/(3t)+1/3}$ on the real axis satisfying $\theta'(k;x,t)=0$, $k_1 \in D_1^+$ and $k_2 \in D_2^+$. Since the saddle points and contours are symmetric with respect to the imaginary axis, we only need to analyze the deformation for D_2^+ and use the mirror image about the imaginary axis for D_1^+. Near the saddle point k_2, θ has the expansion

$$\theta(k;x,t) = \frac{2}{9}i\left(t\sqrt{\frac{3(t+x)}{t}} + x\sqrt{\frac{3(t+x)}{t}}\right) - it\sqrt{\frac{3(t+x)}{t}}(k-k_2)^2 + \mathcal{O}(k-k_2)^3.$$

The direction of steepest descent is along the angles $-\pi/4$ and $3\pi/4$. The integrands need to be extended to the lower half plane similar to the steps in Section 3.4.2.

Deformations of the contour of B_0 for $x \geq 3t$

In this case the saddle points k_1,k_2 lie outside branch cut $[-2/\sqrt{3}, 2\sqrt{3}]$. We proceed as follows.

1. The region $D^+ = \{k \in \mathbb{C}^+ : \mathrm{Re}\,(\omega(k)) < 0\}$ is extended to $\tilde{D} = \{k \in \mathbb{C} : \mathrm{Re}\,(\omega(k)) < \gamma\}$. The transformed data $\tilde{g}_0(\omega(k),\infty)$ is analytic in $\tilde{D}$, and continuous up to $\partial\tilde{D}$.

2. The contour ∂D^+ is deformed to $\mathcal{C}^B_{0,a} \cup \mathcal{C}^B_{0,b} \cup \mathcal{C}^B_{0,c}$ as shown in Figure 3.17. $\mathcal{C}^B_{0,b}$ is the curve passing through the saddle point up to $\partial\tilde{D}$, keeping $\mathrm{Im}\,(\theta(k;x,t))$ constant along the steepest-descent direction and $\mathcal{C}^B_{0,a}, \mathcal{C}^B_{0,c}$ are the unbounded curve segments along $\partial\tilde{D}$.

3. Using that $e^{ikx-\omega(k)t}\int_t^\infty e^{\omega(k)s}g_0(s)ds$ is bounded and analytic in $\tilde{D}$, we can replace $\tilde{g}_0(\omega(k),t)$ with $\tilde{g}_0(\omega(k),\infty)$,

$$\begin{aligned} B_0|_{D_2^+} =& \frac{1}{2\pi}\int_{\partial D_2^+} e^{ikx-\omega(k)t}(\nu_2^2(k)-k^2)\tilde{g}_0(\omega(k),t)dk \\ =& \frac{1}{2\pi}\int_{\mathcal{C}^B_{0,a}\cup\mathcal{C}^B_{0,b}\cup\mathcal{C}^B_{0,c}} e^{ikx-\omega(k)t}(\nu_2^2(k)-k^2)\tilde{g}_0(\omega(k),\infty)dk. \end{aligned}$$

4. The integral along $\mathcal{C}^B_{0,a}$ is decomposed into two parts to maximize decay along the steepest-descent direction,

$$\begin{aligned} &\int_{\mathcal{C}^B_{0,a}} e^{ikx-\omega(k)t}(\nu_2^2(k)-k^2)\tilde{g}_0(\omega(k),\infty)dk = \\ &\qquad \int_{\mathcal{C}^B_{0,a}} e^{ikx-\omega(k)t}(\nu_2^2(k)-k^2)\tilde{g}_0^c(\omega(k),t)dk + \int_{\mathcal{C}^B_{0,d}} e^{ikx-\omega(k)t}(\nu_2^2(k)-k^2)\tilde{g}_0(\omega(k),t)dk, \end{aligned}$$

where

$$\tilde{g}_0^c(\omega(k),t) = \int_t^\infty e^{\omega(k)s}g_0(s)ds,$$

is the complement of the transform $\tilde{g}_0(\omega(k),t)$ and $\mathcal{C}^B_{0,d}$ is extended from $\mathcal{C}^B_{0,b}$ keeping $\mathrm{Im}\,(\theta(k;x,t))$ constant along the steepest-descent direction.

5. The integral along $\mathcal{C}^B_{0,c}$ is decomposed into two parts to separate the leading-order contribution in the oscillatory integral,

$$\begin{aligned} \int_{\mathcal{C}^B_{0,c}} e^{ikx-\omega(k)t}(\nu_2^2(k)-k^2)\tilde{g}_0(\omega(k),\infty)dk &= \int_{\mathcal{C}^I_{0,e}} e^{ikx-\omega(k)t}(\nu_2^2(k_2)-k_2^2)\tilde{g}_0(\omega(k_2),\infty)dk \\ &+ \int_{\mathcal{C}^B_{0,c}} e^{ikx-\omega(k)t}\left[(\nu_2^2(k)-k^2)\tilde{g}_0(\omega(k),\infty) - (\nu_2^2(k_2)-k_2^2)\tilde{g}_0(\omega(k_2),\infty)\right]dk. \end{aligned}$$

The contour $\mathcal{C}^B_{0,e}$ is extended from $\mathcal{C}^B_{0,b}$ keeping $\mathrm{Im}\,(\theta(k;x,t))$ constant along the steepest-descent direction.

6. Finally, we obtain

$$\begin{aligned}B_0|_{D_2^+} =&\frac{1}{2\pi}\int_{\mathcal{C}^I_{0,a}} e^{ikx-\omega(k)t}(\nu_2^2(k)-k^2)\tilde{g}_0^c(\omega(k),t)dk + \frac{1}{2\pi}\int_{\mathcal{C}^B_{0,d}} e^{ikx-\omega(k)t}(\nu_2^2(k)-k^2)\tilde{g}_0(\omega(k),t)dk\\ &+\frac{1}{2\pi}\int_{\mathcal{C}^B_{0,b}} e^{ikx-\omega(k)t}(\nu_2^2(k)-k^2)\tilde{g}_0(\omega(k),\infty)dk\\ &+\frac{1}{2\pi}\int_{\mathcal{C}^B_{0,c}} e^{ikx-\omega(k)t}(\nu_2^2(k)-k^2)\tilde{g}_0(\omega(k),\infty)-(\nu_2^2(k_2)-k_2^2)\tilde{g}_0(\omega(k_2),\infty)dk\\ &+\frac{1}{2\pi}\int_{\mathcal{C}^B_{0,e}} e^{ikx-\omega(k)t}(\nu_2^2(k_2)-k_2^2)\tilde{g}_0(\omega(k_2),\infty)dk.\end{aligned}$$

   The integrals along $\mathcal{C}^B_{0,b}, \mathcal{C}^B_{0,d}$ and $\mathcal{C}^B_{0,e}$ are computed using Clenshaw-Curtis quadrature and the integrals along $\mathcal{C}^B_{0,a}$ and $\mathcal{C}^B_{0,c}$ are computed using Levin's method.

The contour integral $B_0|_{D_1^+}$ is deformed in a symmetrical way. For real-valued data, we can use the symmetry and compute $q(x,t)$ with only the contour integral $B_0|_{D_2^+}$,

$$q(x,t) = 2\mathrm{Re}\left(B_0|_{D_2^+}\right).$$

Deformations of the contour for $B_0|_{D_2^+}$ for $x < 3t$

When $x < 3t$, the saddle points k_1, k_2 lie on branch cut $[-2/\sqrt{3}, 2/\sqrt{3}]$. To maximize the use of the steepest-decent direction, we choose a different branch cut for ν, shown in Figure 3.18 in red. The new branch cut starts from the branch point $2/\sqrt{3}$ and goes along the curve with $\mathrm{Im}\,(\theta(k;x,t))$ constant in the lower half plane. The corresponding $\tilde{\nu}_2(k)$ is defined as the analytic continuation of $\nu_2(k)$ from the interior of D_2^+. We use the following steps.

1. The region $D^+ = \{k \in \mathbb{C}^+ : \mathrm{Re}\,(\omega(k)) < 0\}$ is extended to $\tilde{D} = \{k \in \mathbb{C} : \mathrm{Re}\,(\omega(k)) < \gamma\}$. The transformed data $\tilde{g}_0(\omega(k),\infty)$ is analytic in $\tilde{D}$, and continuous up to $\partial\tilde{D}$.

2. The contour ∂D_2^+ is deformed to $\mathcal{C}^B_{0,a} \cup \mathcal{C}^B_{0,b} \cup \mathcal{C}^B_{0,e} \cup (-\mathcal{C}^B_{0,f}) \cup \mathcal{C}^B_{0,f} \cup \mathcal{C}^B_{0,c}$ as shown in Figure 3.18. The contour $\mathcal{C}^B_{0,b}$ is the curve passing through the saddle point up to $\partial\tilde{D}$

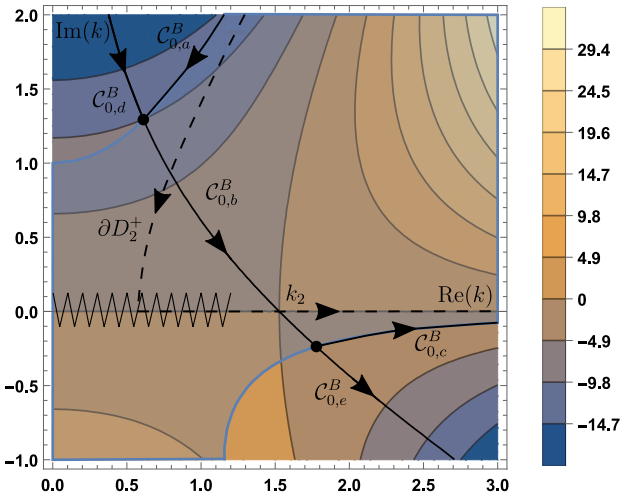

Figure 3.17: The deformed contour for $B_0|_{D_2}$ when $x \geq 3t$ (solid), the undeformed contour (dashed). The background contour plot shows the level sets of $\mathrm{Re}(\theta(k,x,t))$. The branch cut is shown as a jagged line.

with $\mathrm{Im}\left(\theta(k;x,t)\right)$ constant along the steepest-descent direction. The contours $\mathcal{C}^B_{0,a}, \mathcal{C}^B_{0,e}$ and $\mathcal{C}^B_{0,c}$ are along $\partial\tilde{D}$. The contours $-\mathcal{C}^B_{0,f}$ and $\mathcal{C}^B_{0,f}$ are the two segments on the new branch cut with opposite orientations. The contour $-\mathcal{C}^B_{0,f}$ points towards the branch point and $\mathcal{C}^B_{0,f}$ points away from the branch point.

3. Using that $e^{ikx-\omega(k)t}\int_t^\infty e^{\omega(k)s}g_0(s)ds$ is bounded and analytic in $\tilde{D}$, we can replace $\tilde{g}_0(\omega(k),t)$ with $\tilde{g}_0(\omega(k),\infty)$,

$$\begin{aligned}
B_0|_{D_2^+} =& \frac{1}{2\pi}\int_{\partial D_2^+} e^{ikx-\omega(k)t}(\tilde{\nu}_2^2(k)-k^2)\tilde{g}_0(\omega(k),t)dk \\
=& \frac{1}{2\pi}\int_{\mathcal{C}^B_{0,a}\cup\mathcal{C}^B_{0,b}\cup\mathcal{C}^B_{0,e}\cup\mathcal{C}^B_{0,c}} e^{ikx-\omega(k)t}(\tilde{\nu}_2^2(k)-k^2)\tilde{g}_0(\omega(k),\infty)dk \\
& - \frac{1}{2\pi}\int_{\mathcal{C}^B_{0,f}} e^{ikx-\omega(k)t}\tilde{\nu}_2^2(k^-)\tilde{g}_0(\omega(k),\infty)dk + \frac{1}{2\pi}\int_{\mathcal{C}^B_{0,f}} e^{ikx-\omega(k)t}\tilde{\nu}_2^2(k^+)\tilde{g}_0(\omega(k),\infty)dk,
\end{aligned}$$

where k^+ and k^- denote the limit from the left/right of the curve respectively.

4. The integral along $\mathcal{C}^B_{0,a}$ is decomposed into two parts to maximize decay along the

steepest-descent direction:

$$\int_{\mathcal{C}^B_{0,a}} e^{ikx-\omega(k)t}(\tilde{\nu}_2^2(k)-k^2)\tilde{g}_0(\omega(k),\infty)dk =$$
$$\int_{\mathcal{C}^B_{0,a}} e^{ikx-\omega(k)t}(\tilde{\nu}_2^2(k)-k^2)\tilde{g}_0^c(\omega(k),t)dk + \int_{\mathcal{C}^B_{0,d}} e^{ikx-\omega(k)t}(\tilde{\nu}_2^2(k)-k^2)\tilde{g}_0(\omega(k),t)dk,$$

5. We obtain

$$\begin{aligned}
B_0|_{D_2^+} =& \frac{1}{2\pi}\int_{\mathcal{C}^B_{0,a}} e^{ikx-\omega(k)t}(\tilde{\nu}_2^2(k)-k^2)\tilde{g}_0^c(\omega(k),t)dk \\
&+ \frac{1}{2\pi}\int_{\mathcal{C}^B_{0,d}} e^{ikx-\omega(k)t}(\tilde{\nu}_2^2(k)-k^2)\tilde{g}_0(\omega(k),t)dk \\
&+ \frac{1}{2\pi}\int_{\mathcal{C}^B_{0,b}} e^{ikx-\omega(k)t}(\tilde{\nu}_2^2(k)-k^2)\tilde{g}_0(\omega(k),\infty)dk \\
&+ \frac{1}{2\pi}\int_{\mathcal{C}^B_{0,e}\cup\mathcal{C}^B_{0,c}} e^{ikx-\omega(k)t}(\tilde{\nu}_2^2(k)-k^2)\tilde{g}_0(\omega(k),\infty)dk \\
&+ \frac{1}{2\pi}\int_{-\mathcal{C}^B_{0,f}} e^{ikx-\omega(k)t}\tilde{\nu}_2^2(k^+)\tilde{g}_0(\omega(k),\infty)dk \\
&+ \frac{1}{2\pi}\int_{\mathcal{C}^B_{0,f}} e^{ikx-\omega(k)t}\tilde{\nu}_2^2(k^+)\tilde{g}_0(\omega(k),\infty)dk.
\end{aligned}$$

The integrals along $\mathcal{C}^B_{0,b}, \mathcal{C}^B_{0,d}, -\mathcal{C}^B_{0,f}$ and $\mathcal{C}^B_{0,f}$ are computed using Clenshaw-Curtis quadrature and the integrals along $\mathcal{C}^B_{0,a}, \mathcal{C}^B_{0,c}$ and $\mathcal{C}^B_{0,e}$ are computed using Levin's method. The contour integral $B_0|_{D_1^+}$ is deformed symmetrically.

Improving the accuracy near the branch point

Since $\tilde{\nu}_2(k)$ is not differentiable at the branch point $k_2 = 2/\sqrt{3}$, Clenshaw-Curtis quadrature loses spectral accuracy for the integrals along $-\mathcal{C}^B_{0,f}$, $\mathcal{C}^B_{0,f}$ and $\mathcal{C}^B_{0,b}$ in the critical case $x = 3t$. With the change of variables $s^2 = k - k_2$, we get

$$\hat{\nu}_2(s) := \nu_2(s^2+k_2) = (-2\sqrt{3} - 3s^2 - i3^{5/4}s\sqrt{4+\sqrt{3}s^2})/6.$$

The new symmetry $\hat{\nu}_2(s)$ is smooth near $s = 0$. Clenshaw-Curtis quadrature maintains spectral accuracy for the integrals on $\mathcal{C}^B_{0,b}$ and $\mathcal{C}^B_{0,f}$ after this change of variables.

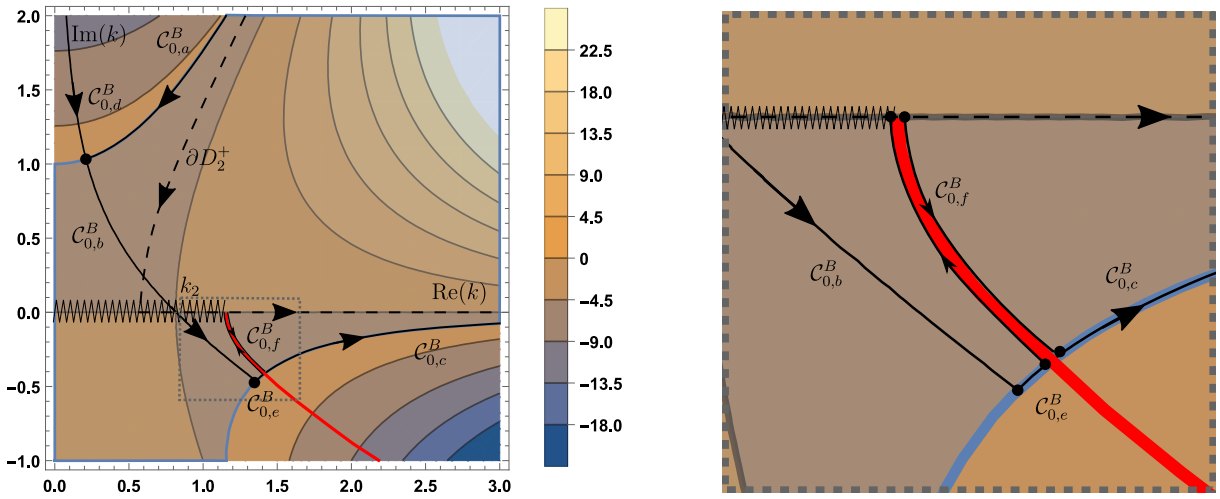

(a) (b)

Figure 3.18: The deformed contour for $B_0|_{D_2}$ when $x < 3t$ (solid). The undeformed contour (dashed). The background contour plot shows the level sets of $\mathrm{Re}(\theta(k, x, t))$. The original branch cut is shown as a jagged line and the new branch cut is shown in red. A zoomed plot of the contour near the new branch cut is shown in the right panel.

Improving the accuracy near the saddle point

Large numerical rounding errors can arise if the parametrization along $\mathcal{C}_{0,b}^B$ is not smooth. For instance, the parametrization of $\mathcal{C}_{0,b}^B$ using $\mathrm{Re}\,(k)$ by mapping the curve to the real line has a square root singularity at the saddle point. Other than seeking an optimal parametrization, we use line segments to approximate the curve near the saddle point.

3.5.2 Numerical examples

Consider the Dirichlet boundary condition $g_0(t) = te^{-t}$, the homogeneous initial condition $q_0(x) = 0$ and the Neumann boundary condition $g_1(t) = 0$. The solution to (3.19) is shown in Figure 3.19. For small time, the dispersive waves emanate from the boundary and the solution looks similar to Figure 3.13. As t grows, the advection dominates and the waves turn back to the boundary. The absolute error and the magnitude of the solution evaluated along (a) $t = 0.1$, (b) $x = 0.1$, (c) $x = 3t$ are shown in Figure 3.20. The errors shown in dotted curves are computed with $N = 20$ collocation points for each part of the contour in B_0 while the errors shown in solid curves are computed with $N = 40$ collocation points. The absolute errors tend to zero as x, t increase. To demonstrate spectral accuracy, the absolute errors E_{NUTM} evaluated at $x = 1, 3, 5$, $t = 1$ are plotted against the number of collocation points per segment in Figure 3.21. With the change of variables used in Section 3.5.1, the NUTM remains spectrally accurate even when the branch point is on the contour of integration.

All our examples use boundary conditions with transforms that can be computed explicitly. This is to allow us to estimate the error of our method by comparing with the built-in integration routine in Mathematica. To show the NUTM is not limited to this, in Figure 3.22, we show a plot of the solution $q(x, t)$ with $g_0(t) = \sin(2t)\phi(t/(2\pi))$ where

$$\phi(t) = \begin{cases} \exp(-1/(1-t^2)) & |t| \le 1, \\ 0 & |t| > 1. \end{cases} \tag{3.21}$$

The initial data and the Neumann data are zero. We see a similar wave pattern as in Figure 3.19 with dispersive waves propagating in the positive x direction, before turning

back.

3.6 Summary of the steps in the Numerical Unified Transform Method applied to linear evolution PDEs.

1. For PDEs of type

$$q_t + \omega(-i\partial_x)q = 0,$$

we construct the solution formula using the UTM.

2. The solution formula from the UTM requires transforms of the known initial and boundary data,

$$\begin{aligned}
\hat{q}_0(k) &= \int_0^\infty e^{-ikx} q_0(x,0)dx, \\
\tilde{g}_0(\omega(k),\infty) &= \int_0^\infty e^{\omega(k)s} q(0,s)ds, \\
&\vdots \\
\tilde{g}_{p-1}(\omega(k),\infty) &= \int_0^\infty e^{\omega(k)s} \frac{\partial^{p-1} q}{\partial x^{p-1}}(0,s)ds.
\end{aligned}$$

For most k values used on the deformed contour, these integrals are oscillatory. We apply Levin's method to compute these integrals.

3. The solution formula depends on (x,t) explicitly through $e^{ikx-\omega(k)t}$. Generally, each connected component of D^+ contains saddle points. The contour ∂D^+ is deformed to pass through the saddle points along the steepest descent directions until it hits the boundary of $\tilde{D}$ (a slightly enlarged version of D^+) where the transforms of the initial and boundary data are analytic. The size of $\tilde{D}$ is determined by the decay rate of the initial and boundary data. The path follows $\partial\tilde{D}$ in the same direction as ∂D^+. The contour deformations may be impacted by singularities such as branch cuts, poles.

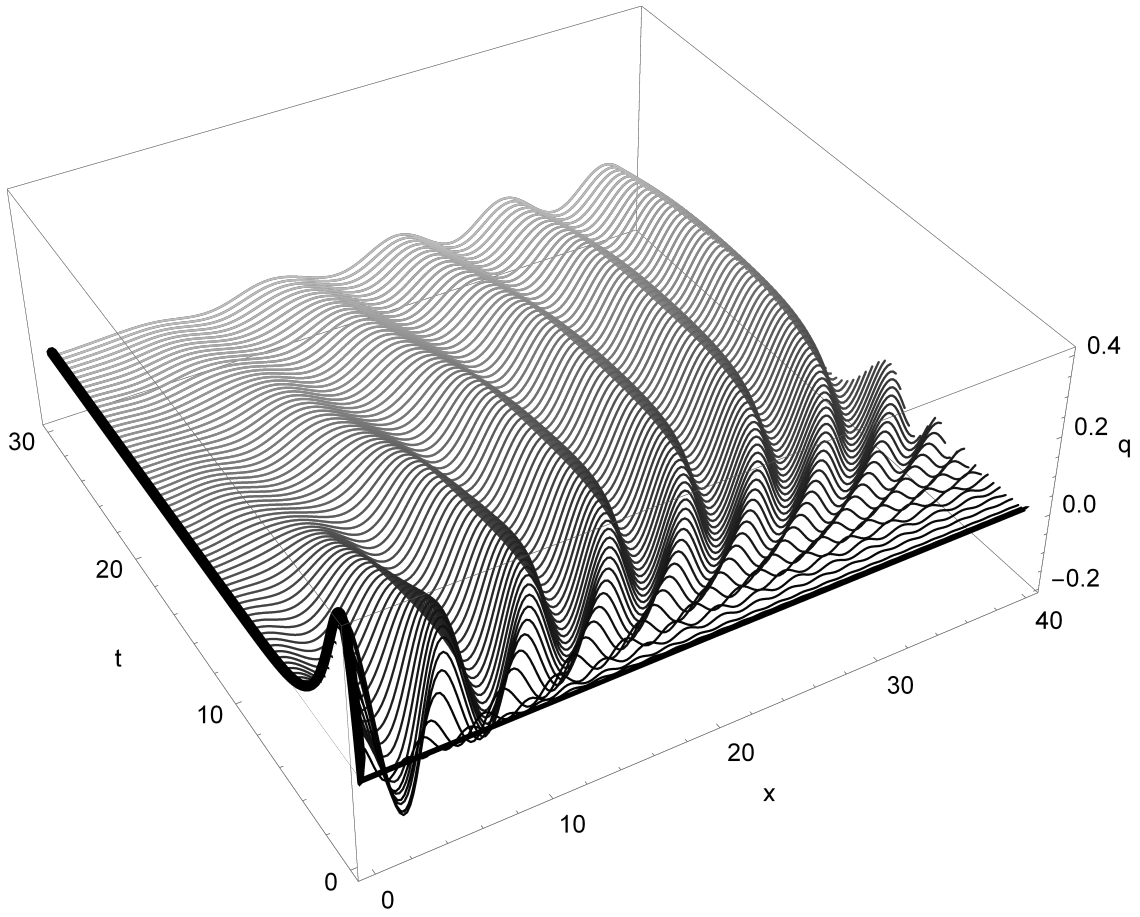

Figure 3.19: The numerical solution of equation (3.19) with $q_0(x) = 0$, $g_0(t) = te^{-t}$, $g_1(t) = 0$. The bold curves are the initial and Dirichlet boundary conditions. For small t, dispersive waves emanate from the boundary while the waves start to turn back following the advection as t grows.

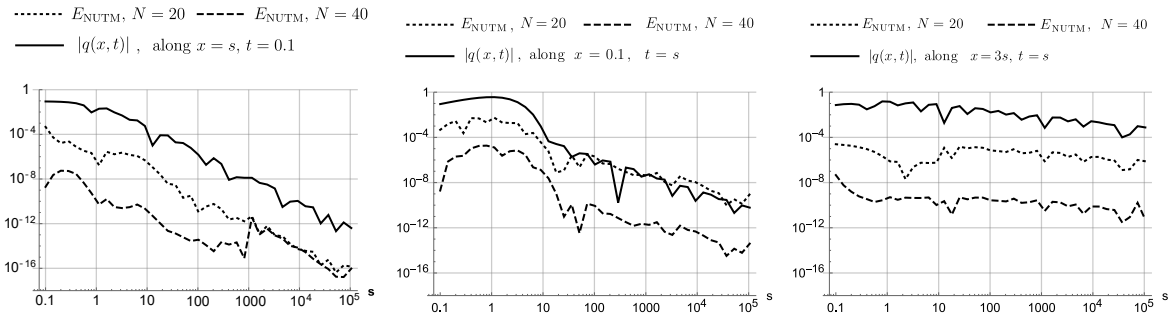

(a) (b) (c)

Figure 3.20: The absolute error E_{NUTM} of the numerical solution to (3.19) along (a) $x = s, t = 0.1$, (b) $x = 0.1, t = s$, (c) $x = 3s, t = s$ for $s \in [0.1, 10^5]$. The computation using $N = 20$ points for each segment in the contour (dotted) and using $N = 40$ points for each segment in the contour (dashed) are plotted.

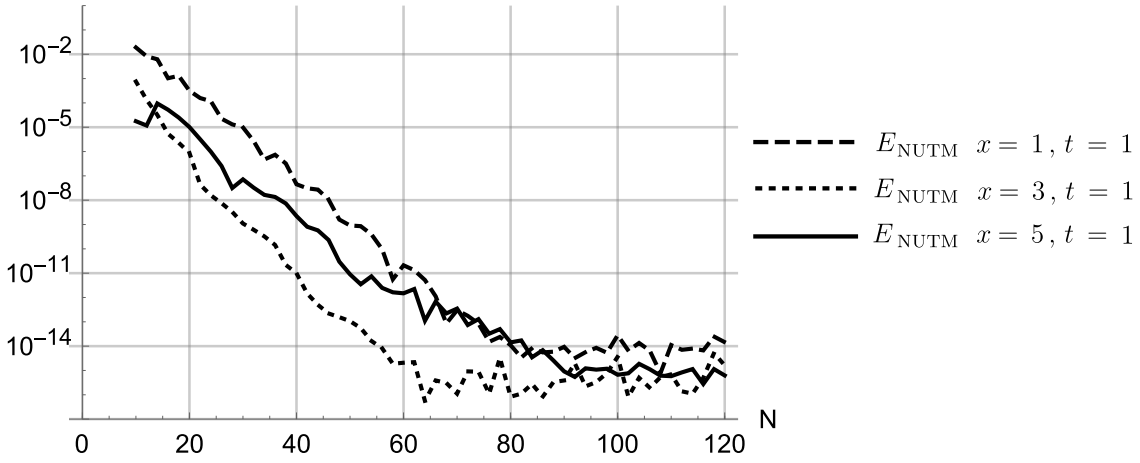

Figure 3.21: The absolute error E_{NUTM} against the number of collocation points N per segment: computed with $x = 1, t = 1$ (dashed), $x = 3, t = 1$ (dotted) and $x = 5, t = 1$ (solid). The truncation tolerance is 10^{-15} for this example.

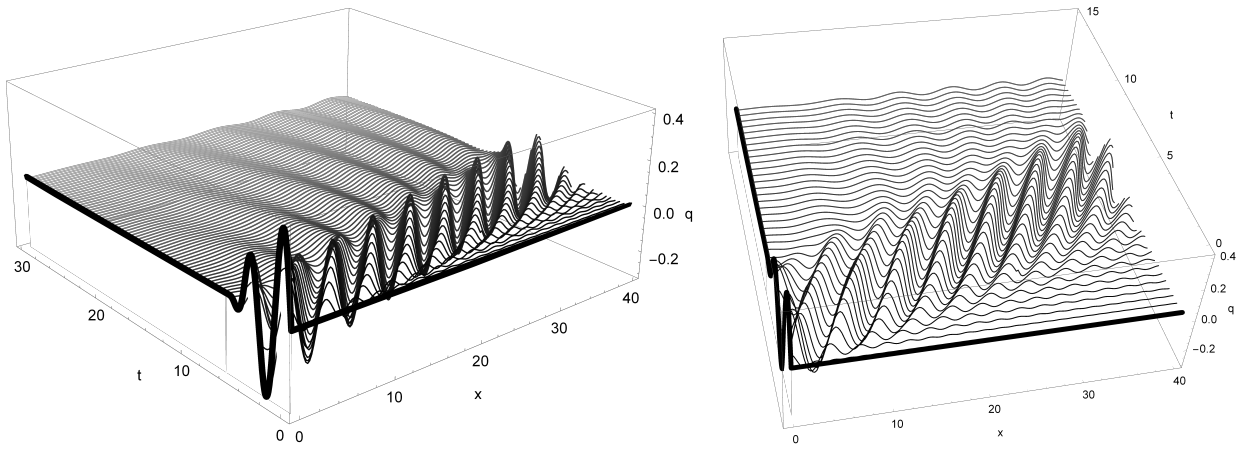

(a) (b)

Figure 3.22: The numerical solution of (3.19) with $g_0 = \sin(2t)\phi(t/(2\pi))$ with $\phi(t)$ defined in (3.21). The bold curves are the initial and Dirichlet boundary conditions. For small t, dispersive waves emanate from the boundary but the waves start to turn back because of advection as t grows. Panel (a) shows the solution for $x \in [0, 40]$, $t \in [0, 30]$. Panel (b) shows the solution from a different angle in a shorter time interval $t \in [0, 15]$.

4. The integrals along the steepest descent direction are non-oscillatory and they are computed using standard quadrature rules. The integrals along $\partial\tilde{D}$ are oscillatory and they are computed using Levin's method.

Chapter 4

THE NUMERICAL UNIFIED TRANSFORM METHOD FOR THE NLS EQUATION ON THE HALF-LINE

In this chapter, we implement the NUTM to the NLS equation on the half-line. A major difference in the UTM for nonlinear integrable IBVPs is that characterization of the unknown boundary data from the given initial and boundary conditions is difficult. For general boundary conditions, the unknown boundary data satisfies a system of nonlinear Volterra equations [62]. We believe that the nonlinear nature of the problem is unavoidable when solving problems with general boundary conditions. In this chapter, we show that for linearizable boundary conditions (see Section 4.2 for the definition), the NUTM applies to the NLS equation on the half-line in the same fashion as on the whole line with all features 1-6. This is indeed expected as these cases can be treated by appropriate spatial reflection. But importantly, if the spectral functions are known, the same procedures can still be applied. We also discuss the asymptotics of the spectral functions.

This chapter is organized as follows: Section 4.2 gives a brief overview of the UTM for the NLS equation on the half-line. In Section 4.3, we discuss the NUTM applied to the NLS equation with linearizable boundary conditions. In Section 4.4, we consider the solutions with prescribed spectral functions. The corresponding boundary conditions are not necessarily linearizable. In Section 4.5, we discuss the asymptotics of the spectral functions to improve accuracy for small x, t.

4.1 The Unified Transform Method for the NLS equation on the half-line

In this section we describe the UTM applied to the NLS equation on the half-line. A complete discussion is given in [34] and [35].

4.1.1 The Lax pair

The NLS equation

$$iq_t + q_{xx} + 2\lambda |q|^2 q = 0,\ \lambda = \pm 1, \tag{4.1}$$

is integrable with the associated Lax pair

$$\mu_x + ik[\sigma_3, \mu] = Q(x,t)\mu, \tag{4.2a}$$

$$\mu_t + 2ik^2[\sigma_3, \mu] = \tilde{Q}(x,t,k)\mu, \tag{4.2b}$$

where $\sigma_3 = \mathrm{diag}(1,-1)$, $[A,B] = AB - BA$ and

$$Q(x,t) = \begin{bmatrix} 0 & q(x,t) \\ -\lambda\overline{q(x,t)} & 0 \end{bmatrix},\ \tilde{Q}(x,t,k) = 2kQ - iQ_x\sigma_3 + i\lambda|q|^2\sigma_3.$$

Here $\lambda = \pm 1$ gives the focusing/defocusing NLS equation. (λ in [34] is $-\lambda$ here.) The compatibility of (2a) and (2b), $\mu_{xt} = \mu_{tx}$, is equivalent to $q(x,t)$ satisfying (4.1). Using the Lax pair (4.2a), (4.2b) we define

$$W(x,t,z) = d(e^{i(kx+2k^2t)\hat{\sigma}_3}\mu(x,t,k)) = e^{i(kx+2k^2t)\hat{\sigma}_3}\left(Q\mu(x,t,k)dx + \tilde{Q}\mu(x,t,k)dt\right), \tag{4.3}$$

where

$$\hat{\sigma}_3 A := [\sigma_3, A],\ e^{\hat{\sigma}_3}A = e^{\sigma_3}Ae^{-\sigma_3}.$$

Requiring that W is closed implies that $q(x,t)$ satisfies (4.1). An integral equation for a solution of the Lax pair (4.2a),(4.2b) is obtained by integrating the differential form,

$$\mu(x,t,k) = I + \int_{(x_*,t_*)}^{(x,t)} e^{-i(kx+2k^2t)\hat{\sigma}_3}W(\xi,\tau,k), \tag{4.4}$$

where I is the 2×2 identity matrix, $x,t \in (0,\infty)$ and $x_*, t_* \in [0,\infty]$. Using particular choices of (x_*,t_*), particular solutions are constructed and used to define the so-called spectral functions.

4.1.2 The spectral functions

Assume that $q(x,t)$ solves (4.1) for $x,t>0$ with the initial values

$$q(x,0)=q_0(x),\ x\geq 0,$$

and the boundary values

$$q(0,t)=g_0(t),\ t\geq 0,$$
$$q_x(0,t)=g_1(t),\ t\geq 0.$$

In general, we do not know both boundary functions $g_0(t)$ and $g_1(t)$. The NLS equation on the half-line is well-posed with either $g_0(t)$ or $g_1(t)$ specified [16, 18, 46]. We further assume that the initial condition q_0 is in $\mathcal{S}_\alpha(\mathbb{R}^+)$, the Schwartz class functions restricted to the positive half-line with exponential decay rate $\alpha>0$:

$$\mathcal{S}_\alpha(\mathbb{R}^+)=\left\{f\in\mathcal{S}(\mathbb{R})|_{\mathbb{R}^+},\ \exists\alpha'>\alpha>0:\ \sup_{x\in\mathbb{R}^+}e^{\alpha' x}\left|f(x)\right|<\infty\right\}.$$

Following [34], in this section, the boundary functions g_0 and g_1 are assumed to be smooth functions on $[0,T]$ and when $T=\infty$, g_0 and g_1 are assumed to be in $\mathcal{S}(\mathbb{R})|_{\mathbb{R}^+}$ which is sufficient to define the spectral functions. For the numerical examples we consider, this sufficient condition may not be satisfied. Different assumptions on the boundary values are used for problems discussed in Section 3, 4 and 5 so long as the spectral functions can be computed.

Using the conventions in [34], μ_1,μ_2 and μ_3 are defined using $(x_*,t_*)=(0,T)$, $(x_*,t_*)=(0,0)$ and $(x_*,t_*)=(\infty,t)$ respectively. For $T<\infty$ the spectral functions $s(k)$ and $S(k,T)$ are defined by

$$s(k)=\mu_3(0,0,k),\ S(k,T)=[e^{2ik^2T\hat{\sigma}_3}\mu_2(0,T,k)]^{-1}.$$

With this choice, $s(k)$ depends only on the initial values q_0 and $S(k,T)$ depends only on the boundary values g_0 and g_1 on the interval $[0,T]$. There is an alternate definition $S(k,\infty)=\mu_1(0,0,k)$, which is more convenient when $T=\infty$.

4.1.3 Properties of the spectral functions

Using the symmetries of Q and $\tilde{Q}$, the spectral functions have the form

$$s(k) = \begin{bmatrix} \overline{a(\overline{k})} & b(k) \\ -\lambda\overline{b(\overline{k})} & a(k) \end{bmatrix}, \; S(k,T) = \begin{bmatrix} \overline{A(\overline{k},T)} & B(k,T) \\ -\lambda\overline{B(\overline{k},T)} & A(k,T) \end{bmatrix}.$$

Moreover, since Q and $\tilde{Q}$ are traceless,

$$\det\, s(k) = \det\, S(k,T) = 1,$$

which implies that

$$a(k)\overline{a(\overline{k})} + \lambda b(k)\overline{b(\overline{k})} = 1, \; k \in \mathbb{R}, \tag{4.5a}$$

$$A(k,T)\overline{A(\overline{k},T)} + \lambda B(k,T)\overline{B(\overline{k},T)} = 1, \; k \in \mathbb{C} \; (k \in \mathbb{R} \cup i\mathbb{R} \text{ if } T = \infty). \tag{4.5b}$$

It is convenient to characterize the spectral functions $a(k) = \phi_2(0,k)$ and $b(k) = \phi_1(0,k)$ using linear Volterra integral equations:

$$\phi_1(x,k) = -\int_x^\infty e^{-2ik(x-y)} q_0(y)\phi_2(y,k)dy, \tag{4.6a}$$

$$\phi_2(x,k) = 1 - \lambda\int_x^\infty \bar{q}_0(y)\phi_1(y,k)dy. \tag{4.6b}$$

If $q_0 \in \mathcal{S}(\mathbb{R})|_{\mathbb{R}^+}$, $a(k)$ and $b(k)$ are analytic for $\mathrm{Im}\,(k) > 0$. With the additional assumption on exponential decay $q_0 \in \mathcal{S}_\alpha(\mathbb{R}^+)$, $a(k)$ and $b(k)$ are analytic in a larger region that contains $\mathrm{Im}\,(k) \geq -\alpha/2$.

For $T < \infty$, the spectral functions $\overline{A(\overline{k},T)} = \Phi_2(T,k)$ and $-e^{-4ik^2T}B(k,T) = \Phi_1(T,k)$ are defined using a different set of linear Volterra integral equations:

$$\Phi_1(t,k) = \int_0^t e^{-4ik^2(t-\tau)} \left(\tilde{Q}_{11}\Phi_1 + \tilde{Q}_{12}\Phi_2\right)(\tau,k)d\tau, \tag{4.7a}$$

$$\Phi_2(t,k) = 1 + \int_0^t \left(\tilde{Q}_{21}\Phi_1 + \tilde{Q}_{22}\Phi_2\right)(\tau,k)d\tau. \tag{4.7b}$$

Therefore $A(k,T)$ and $B(k,T)$ are entire and bounded in $\mathrm{Im}\,(k^2) \geq 0$.

For $T = \infty$, the spectral functions $A(k, \infty) = \Phi_2(0, k)$ and $B(k, \infty) = \Phi_1(0, k)$ are defined by yet another set of linear Volterra integral equations:

$$\tilde{\Phi}_1(t,k) = -\int_t^\infty e^{-4ik^2(t-\tau)} \left(\tilde{Q}_{11}\tilde{\Phi}_1 + \tilde{Q}_{12}\tilde{\Phi}_2\right)(\tau,k)d\tau, \tag{4.8a}$$

$$\tilde{\Phi}_2(t,k) = 1 - \int_t^\infty \left(\tilde{Q}_{21}\tilde{\Phi}_1 + \tilde{Q}_{22}\tilde{\Phi}_2\right)(\tau,k)d\tau. \tag{4.8b}$$

Therefore $A(k, \infty)$ and $B(k, \infty)$ are analytic for $\mathrm{Im}\,(k^2) > 0$ and bounded for $\mathrm{Im}\,(k^2) \geq 0$.

Since $A(k,T), B(k,T)$ are computed from overdetermined boundary data ($\tilde{Q}$ depends on both q and q_x), the spectral functions $a(k), b(k)$ from the initial values and $A(k,T), B(k,T)$ from the boundary values are not independent. This is clear because the Dirichlet to Neumann map depends on the initial data. The integral of the 1-form (4.3) along the boundary of the domain $(x,t) \in (0,\infty) \times (0,T)$ must vanish and we have the global relation connecting the information from the initial values and the boundary values in terms of the spectral data,

$$a(k)B(k,T) - b(k)A(k,T) = e^{4ik^2T}c^+(k,T),\ \mathrm{Im}\,(k) \geq 0, \tag{4.9}$$

where $c^+(k,T)$ is:

- an undetermined function analytic for $\mathrm{Im}\,(k) > 0$,
- continuous and bounded for $\mathrm{Im}\,(k) \geq 0$, and
- $c^+(k,T) = O(1/k)$, as $k \to \infty$ for $\mathrm{Im}\,(k) > 0$.

If $T = \infty$, the global relation reduces to

$$a(k)B(k,\infty) - b(k)A(k,\infty) = 0,\ \mathrm{Im}\,(k) \geq 0, \mathrm{Re}\,(k) \geq 0. \tag{4.10}$$

Definition 4 (an admissible set of functions [34]). *Given $q_0 \in \mathcal{S}(\mathbb{R}^+)$, the pair $\{g_0, g_1\}$ of smooth functions on $[0,T]$ or $[0,\infty)$ (if $T = \infty$) is an admissible set of functions with respect to q_0 if the following conditions are satisfied:*

1. *The associated spectral functions* $\{a, b, A, B\}$ *satisfy the global relation (4.9) for* $T < \infty$ *or (4.10) for* $T = \infty$.

2. *The functions* q_0, g_0 *and* g_1 *are compatible at* $x = t = 0$, *i.e.,* $g_0(0) = q_0(0)$, $g_1(0) = q_0'(0)$. *More equation-dependent conditions may be imposed if more regularity of the solution* $q(x,t)$ *is desired.*

Remark 8. *The spectral functions* $s(k), S(k,T)$ *are nonlinear transforms of the corresponding initial and boundary values. For the LS equation (when* $\lambda = 0$*),* $\mu_3(x,0,k) = \begin{pmatrix} \mu_{11} & \mu_{12} \\ \mu_{21} & \mu_{22} \end{pmatrix}$ *satisfies (4.2a),*

$$\begin{pmatrix} \mu_{11} & \mu_{12} \\ \mu_{21} & \mu_{22} \end{pmatrix}_x + 2ik \begin{pmatrix} 0 & \mu_{12} \\ -\mu_{21} & 0 \end{pmatrix} = \begin{pmatrix} 0 & q(x,0) \\ 0 & 0 \end{pmatrix} \begin{pmatrix} \mu_{11} & \mu_{12} \\ \mu_{21} & \mu_{22} \end{pmatrix}, \tag{4.11}$$

with $\mu_3(\infty, 0, k) = I$. *Solving (4.11) yields*

$$\mu_3(x,0,k) = \begin{pmatrix} 1 & -e^{-2ikx} \int_x^\infty e^{2ik\xi} q(\xi,0) d\xi \\ 0 & 1 \end{pmatrix}, \text{ and} \tag{4.12}$$

the spectral function $s(k)$ *is given by*

$$s(k) = \mu_3(0,0,k) = \begin{pmatrix} 1 & -\int_0^\infty e^{2ik\xi} q(\xi,0) d\xi \\ 0 & 1 \end{pmatrix}. \tag{4.13}$$

Therefore $b(k) = -\int_0^\infty e^{2ik\xi} q(\xi,0) d\xi$ *is the Fourier transform of the initial condition on the half-line. On the other hand,* $\mu_2(0,t,k) = \begin{pmatrix} \mu_{11} & \mu_{12} \\ \mu_{21} & \mu_{22} \end{pmatrix}$ *satisfies (4.2b),*

$$\begin{pmatrix} \mu_{11} & \mu_{12} \\ \mu_{21} & \mu_{22} \end{pmatrix}_t + 4ik^2 \begin{pmatrix} 0 & \mu_{12} \\ -\mu_{21} & 0 \end{pmatrix} = \begin{pmatrix} 0 & 2kq(0,t) + iq_x(0,t) \\ 0 & 0 \end{pmatrix} \begin{pmatrix} \mu_{11} & \mu_{12} \\ \mu_{21} & \mu_{22} \end{pmatrix}, \tag{4.14}$$

with $\mu_2(0,0,k) = I$. *Solving (4.14) yields*

$$\mu_2(0,T,k) = \begin{pmatrix} 1 & e^{-4ik^2T}\int_0^T e^{4ik^2\eta}\left(2kq(0,\eta) + iq_x(0,\eta)\right)d\eta \\ 0 & 1 \end{pmatrix}, \tag{4.15}$$

and the spectral function $S(k,T)$ *is given by*

$$S(k,T) = [e^{2ik^2T\hat{\sigma}_3}\mu_2(0,T,k)]^{-1} = \begin{pmatrix} 1 & -\int_0^T e^{4ik^2\eta}\left(2kq(0,\eta) + iq_x(0,\eta)\right)d\eta \\ 0 & 1 \end{pmatrix}. \tag{4.16}$$

Therefore $B(k) = -\int_0^T e^{4ik^2\eta}\left(2kq(0,\eta) + iq_x(0,\eta)\right)d\eta$ *is a sum of Fourier-type transforms of the boundary data on the interval* $[0,T]$. *The global relation (4.9) becomes*

$$\int_0^\infty e^{2ik\xi}q(\xi,0)d\xi - \left(i\int_0^T e^{4ik^2\eta}q_x(0,\eta)d\eta + 2k\int_0^T e^{4ik^2\eta}q(0,\eta)d\eta\right) = e^{4ik^2T}c^+(k,T),\ Im\,(k) \geq 0,$$

where

$$c^+(k,T) = \int_0^\infty e^{2ik\xi}q(\xi,T)d\xi.$$

This is exactly the same as the global relation in [23] which is obtained using Green's theorem.

Remark 9 (The nonlinear Volterra integral equation)**.** *In [39], it is shown that for the Dirichlet problem, the unknown Neumann value is given by*

$$\begin{aligned} g_1(t) = \frac{2}{\pi i}\int_{\partial D_3}\left(k\chi_1(t,k) + ig_0(t)\right)dk + \frac{2g_0(t)}{\pi}\int_{\partial D_3}\chi_2(t,k)dk \\ -\frac{4}{\pi i}\int_{\partial D_3} ke^{-4ik^2t}\frac{b(-k)}{a(-k)}\overline{\Phi_2(t,-\overline{k})}dk, \end{aligned} \tag{4.17}$$

for $0 < t < T$ *where* ∂D_3 *is the boundary of the third quadrant in the complex plane with counterclockwise orientation and*

$$\chi_j(t,k) = \Phi_j(t,k) - \Phi_j(t,-k), \quad j = 1,2, \quad 0 < t < T, \quad k \in \mathbb{C}.$$

For convenience, suppose that $a(k)$ *does not have zeros in the upper half-plane. Plugging the equation of* $g_1(t)$ *back into (4.7a) and (4.7b) yields a nonlinear Volterra integral equation for* $\Phi_1(t,k)$ *and* $\Phi_2(t,k)$ *that depend only on known data. However, since* $\Phi_j(t,k)$ *requires all*

the values of $\Phi_1(s,k), 0 < s < t, k \in \partial D_3$, this is a fundamentally nonlinear problem that depends on two continuous variables. As discussed in Section 4.3.1, even if one can solve the nonlinear Volterra integral equation for the unknown $g_1(t)$, the slow decay of $g_1(t)$ will affect the overall accuracy when computing the solution to the NLS equation. Perturbative methods for the nonlinear Volterra integral equation have been studied in [39] and [56] using related equations.

4.1.4 The Riemann-Hilbert problem

With the spectral functions $a(k), b(k)$ and $A(k,T), B(k,T)$ defined in the previous sections, we obtain $q(x,t)$ by solving the following RHP.

Theorem 2 ([34])**.** *Suppose that q_0 and an admissible set of functions $\{g_0, g_1\}$ with respect to q_0 are given. The spectral functions $a(k), b(k)$ are defined via (4.6a,4.6b), $A(k,T), B(k,T)$ are defined via (4.7a,4.7b) for $T < \infty$ and $A(k,\infty), B(k,\infty)$ are defined via (4.8a,4.8b) for $T = \infty$. Assume that*

- *If $\lambda = 1$, $a(k)$ has at most n simple zeroes $\{p_j^a\}_1^n$ in region $\mathbb{C}^+\backslash i\mathbb{R}$. Let n_1 be the number of the zeroes in the first quadrant $\arg p_j^a \in (0, \pi/2), j = 1, \ldots, n_1$, and therefore $\arg p_j^a \in (\pi/2, \pi), j = n_1 + 1, \ldots, n$.*

- *If $\lambda = 1$, for both $T < \infty$ and $T = \infty$, then*

$$d(k,T) = a(k)\overline{A(\overline{k},T)} + \lambda b(k)\overline{B(\overline{k},T)}, \ \ arg\ k \in [\pi/2, \pi], \tag{4.18}$$

  has at most n_2 simple zeroes in the second quadrant $\{p_j^d\}_1^{n_2}$, where $\arg p_j^d \in (\pi/2, \pi)$, $j = 1, \ldots, n_2$.

For both $T < \infty$ and $T = \infty$, the following 2×2 matrix RHP for $\Phi(k;x,t)$ has a unique solution:

1. *$\Phi(k;x,t)$ is sectionally meromorphic for $k \in \mathbb{C}\backslash\{\mathbb{R} \cup i\mathbb{R}\}$ (sectionally analytic if $\lambda = -1$).*

2. *For $k \in \mathcal{C}$ where $\mathcal{C}$ is an oriented contour, define $\Phi_{\pm}(k;x,t)$ to be the limit of $\Phi(k';x,t)$ as $k' \to k$ nontangentially from the right $(+)$ or the left $(-)$. $\Phi(k;x,t)$ satisfies the jump condition on the cross $k \in \mathbb{R} \cup i\mathbb{R}$ with orientation as shown in Figure 4.1,*

$$\Phi_+(k;x,t) = \Phi_-(k;x,t)J(k;x,t), \tag{4.19}$$

The jump matrix $J(k;x,t)$ is given by

$$J(k;x,t) = \begin{cases} J_4(k;x,t), & arg\ k = 0, \\ J_1(k;x,t), & arg\ k = \frac{\pi}{2}, \\ J_2(k;x,t), & arg\ k = \pi, \\ J_3(k;x,t), & arg\ k = \frac{3\pi}{2}, \end{cases} \tag{4.20}$$

where

$$J_1(k;x,t) = \begin{bmatrix} 1 & 0 \\ -\Gamma(k,T)e^{2i\theta(k;x,t)} & 1 \end{bmatrix},$$

$$J_3(k;x,t) = \begin{bmatrix} 1 & -\lambda\overline{\Gamma(\overline{k},T)}e^{-2i\theta(k;x,t)} \\ 0 & 1 \end{bmatrix},$$

$$J_4(k;x,t) = \begin{bmatrix} 1+\lambda\gamma(k)\overline{\gamma(\overline{k})} & \gamma(k)e^{-2i\theta(k;x,t)} \\ \lambda\overline{\gamma(\overline{k})}e^{2i\theta(k;x,t)} & 1 \end{bmatrix},$$

$$\begin{aligned} J_2(k;x,t) =& J_1(k;x,t)J_4^{-1}(k;x,t)J_3(k;x,t) \\ =& \begin{bmatrix} 1 & -\left(\lambda\overline{\Gamma(\overline{k},T)}+\gamma(k)\right)e^{-2i\theta(k;x,t)} \\ -\left(\lambda\overline{\gamma(\overline{k})}+\Gamma(k,T)\right)e^{2i\theta(k;x,t)} & 1+\left(\lambda\overline{\Gamma(\overline{k},T)}+\gamma(k)\right)\left(\lambda\overline{\gamma(\overline{k})}+\Gamma(k,T)\right) \end{bmatrix}, \end{aligned}$$

and

$$\theta(k;x,t) = kx + 2k^2t,\ k \in \mathbb{C}, \tag{4.21a}$$

$$\gamma(k) = \frac{b(k)}{\overline{a(\overline{k})}},\ k \in \mathbb{R}, \tag{4.21b}$$

$$\Gamma(k,T) = -\frac{\lambda\overline{B(\overline{k},T)}}{a(k)d(k,T)},\ arg\ k \in \left[\frac{\pi}{2},\pi\right]. \tag{4.21c}$$

3. *If $\lambda = 1$, the first column of $\Phi(k;x,t)$ has simple poles at $\{p_j^a\}_1^{n_1}$ and $\{p_j^d\}_1^{n_2}$. The second column of $\Phi(k;x,t)$ has simple poles at $\{\overline{p_j^a}\}_1^{n_1}$ and $\{\overline{p_j^d}\}_1^{n_2}$. The associated residues satisfy the relations:*

$$Res_{k=p_j^a}\Phi(k;x,t) = \lim_{k\to p_j^a}\Phi(k;x,t)\begin{pmatrix} 0 & 0 \\ \frac{1}{a'(p_j^a)b(p_j^a)}e^{2i\theta(p_j^a;x,t)} & 0 \end{pmatrix}, \quad j=1,\dots,n_1, \tag{4.22a}$$

$$Res_{k=\overline{p_j^a}}\Phi(k;x,t) = \lim_{k\to\overline{p_j^a}}\Phi(k;x,t)\begin{pmatrix} 0 & \frac{-\lambda}{\overline{a'(p_j^a)b(p_j^a)}}e^{-2i\theta(\overline{p_j^a};x,t)} \\ 0 & 0 \end{pmatrix}, \quad j=1,\dots,n_1, \tag{4.22b}$$

$$Res_{k=p_j^d}\Phi(k;x,t) = \lim_{k\to p_j^d}\Phi(k;x,t)\begin{pmatrix} 0 & 0 \\ -\frac{\lambda\overline{B(\overline{p_j^d})}}{a(p_j^d)d'(p_j^d)}e^{2i\theta(p_j^d;x,t)} & 0 \end{pmatrix}, \quad j=1,\dots,n_2, \tag{4.22c}$$

$$Res_{k=\overline{p_j^d}}\Phi(k;x,t) = \lim_{k\to\overline{p_j^d}}\Phi(k;x,t)\begin{pmatrix} 0 & \frac{B(\overline{p_j^d})}{\overline{a(p_j^d)d'(p_j^d)}}e^{-2i\theta(\overline{p_j^d};x,t)} \\ 0 & 0 \end{pmatrix}, \quad j=1,\dots,n_2. \tag{4.22d}$$

4. *$\Phi(k;x,t) = I + O(1/k)$ as $k\to\infty$.*

Then (as shown in [34])

$$q(x,t) = 2i\lim_{k\to\infty}\left(k\Phi(k;x,t)\right)_{12},$$

solves the NLS equation with

$$q_x(x,t) = \lim_{k\to\infty}\left\{4\left(k^2\Phi(k;x,t)\right)_{12} + 2iq(x,t)\left(k\Phi(k;x,t)\right)_{22}\right\},$$

$$q(x,0) = q_0(x), \quad q(0,t) = g_0(t) \quad \textit{and} \quad q_x(0,t) = g_0(t).$$

Figure 4.2 shows a detailed diagram of the UTM applied to nonlinear integrable PDEs. The steps 1 and 1′ denote the invertible transforms between the initial condition $q(x,0) =$

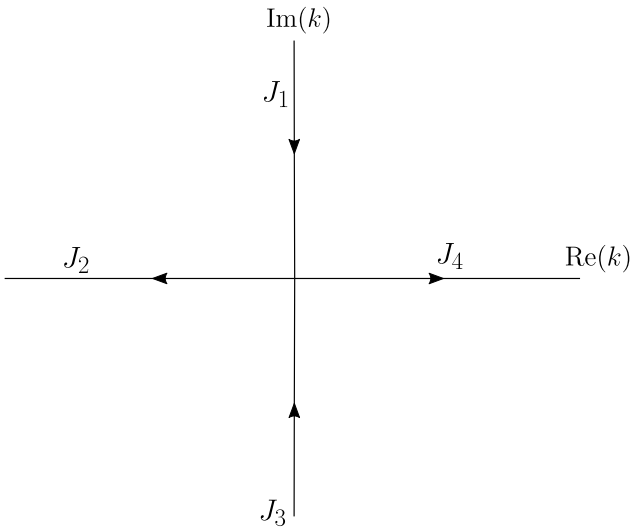

Figure 4.1: The jump contour of RHPs (4.19) and (4.32). The contour consists of the real and imaginary axes.

$q_0(x)$ and the spectral functions $\{a(k), b(k)\}$. The step 2 and $2'$ denote the invertible transforms between the pair of boundary functions $\{q(0,t) = g_0(t),\ q_x(0,t) = g_1(t)\}$ and the spectral functions $\{A(k,T), B(k,T)\}$ for $T < \infty$ or $T = \infty$. Step 3 denotes obtaining $\{A(k,T), B(k,T)\}$ with a special class of boundary conditions known as linearizable boundary conditions. Step 4 denotes the construction of the associated RHP using the spectral functions incorporating time dependence. Step 5 denotes the inverse transform to get the solution $q(x,t)$ by solving the RHP. In following sections, we show examples of the solutions that can be efficiently computed with different types of given data. In Section 4.2, we give an example with linearizable boundary conditions following steps 1-5. In Section 4.4.1, we show an example with an admissible set of functions $g_0, g_1 \in \mathcal{S}_\beta(\mathbb{R}^+)$ with respect to $q_0 \in \mathcal{S}_\alpha(\mathbb{R}^+)$. This follows steps $1, 2, 4, 5$ in Figure 4.2. In Section 4.4.2, we show an example with specified spectral functions that follows steps $4, 5$ in Figure 4.2. This is also known as the dressing method to construct solution to the NLS equation [35].

Remark 10. *The defocusing NLS equation on the half-line does not have soliton solutions [55]. More precisely, $a(k)$ does not have zeroes for $Im\,(k) \geq 0$ and $d(k,T)$ does not*

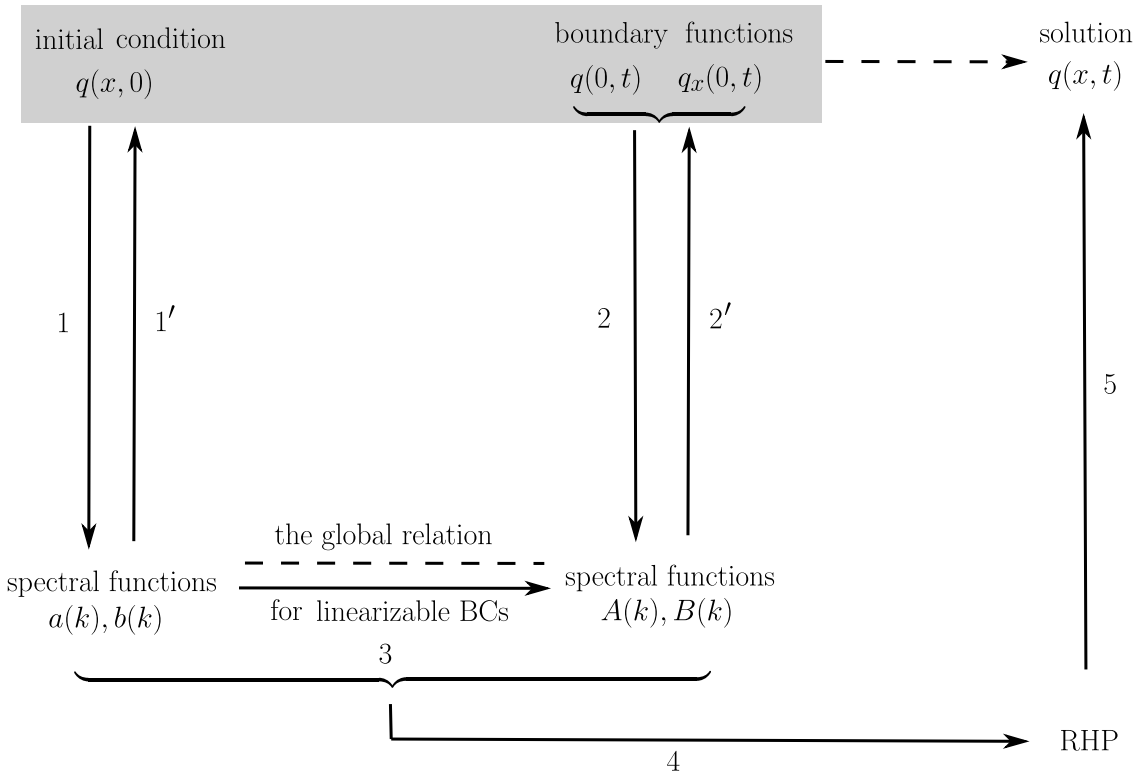

Figure 4.2: A diagram describing the use the UTM to solve integrable PDEs on the half-line. The path along 1, 4, 5 is the same as the IST for IVPs. In this chapter, we focus on three paths: (a) The path along 1-5 for problems with linearizable boundary conditions. (b) The path along 1, 2, 4, 5 for problem with overdetermined but compatible initial and boundary values. (c) The path along 4, 5 for problems with specified spectral functions.

have zeroes for $arg(k) \in [\pi/2, \pi]$.

Remark 11. *When* $t = 0$*, the RHP (4.19) reduces to a RHP that depends only on* $a(k)$ *and* $b(k)$ *after deforming* J_1 *and* J_3 *to the negative real line. The global relation is not needed in the deformation. When* $x = 0$*, the RHP (4.19) reduces to a RHP that depends only on* $A(k,T)$ *and* $B(k,T)$ *on the cross* $k \in \mathbb{R} \cup i\mathbb{R}$ *but the reduction requires the use of the global relation as well as (4.5b).*

4.1.5 Algorithms for computing the spectral data

The goal of the numerical computation for the forward transform is to obtain: (i) evaluate the spectral functions along the (deformed) jump contour, (ii) in the focusing case, the zeroes of $a(k)$ and $d(k,T)$ as well as the related residues.

(i) Continuous spectral data: For convenience, we describe the algorithm for the computations of the spectral data in the case $T=\infty$. Assuming q_0, as well as an admissible set of functions g_0 and g_1, are given, we compute the spectral functions $\{a(k),b(k)\}$ using the differential equation form of (4.6a) and (4.6b) and compute $A(k,\infty),B(k,\infty)$ using the differential form of (4.8a) and (4.8b). Both sets of equations are in the form of

$$\begin{pmatrix} y_1(s,k) \\ y_2(s,k) \end{pmatrix}_s + \mathcal{M}_1(k) \begin{pmatrix} y_1(s,k) \\ y_2(s,k)+1 \end{pmatrix} = \mathcal{M}_2(s,k) \begin{pmatrix} y_1(s,k) \\ y_2(s,k)+1 \end{pmatrix}.$$

They are solved by a Chebyshev collocation method [9] on $[0,L]$ with vanishing boundary condition at $y_1(L,k)=y_2(L,k)=0$ for sufficiently large L. The method is the same as in Chapter 2 when solving the scattering problem for the SG equation. A detailed discuss of the Chebyshev collocation method solving this type of the equations can be found in [73] and [74].

(ii) Discrete spectral data: In [55], it is shown that zeroes of $a(k)$ in the upper half-plane are the $L^2(\mathbb{R},\mathbb{C}^{2\times 2})$ eigenvalues of the operator

$$\mathcal{L} = i\sigma_3\partial_x - i\sigma_3 Q_e,$$

where

$$q_e(x) = \begin{cases} q(x,0), & x\geq 0, \\ 0, & x<0, \end{cases} \quad \text{and} \quad Q_e = \begin{bmatrix} 0 & q_e \\ -\lambda\overline{q_e} & 0 \end{bmatrix}.$$

The eigenvalues are obtained using the Floquet-Fourier-Hill method [22]. Though the Floquet-Fourier-Hill method does not achieve spectral accuracy due to the possible discontinuity of the potential $q_e(x)$ at $x=0$, it provides initial guesses for Newton's method. Residue

conditions requires evaluating the norming constants $c_j^a := \frac{1}{a'(p_j^a)b(p_j^a)}$ at the zeroes $\{p_j^a\}_1^{n_1}$ where $a'(p_j^a)$ is computed by Cauchy's integral formula.

Similarly, it is shown in [55] that the zeroes of $d(k,T)$ satisfy the same eigenvalue problem except that

$$q_e(x) = \begin{cases} q(x,T), & x \geq 0, \\ 0, & x < 0. \end{cases}$$

However, the potential q_e depends on the unknown solution $q(x,T)$, root-finding algorithms are needed to find zeroes of $d(k,T)$. Once the zeroes $\{p_j^d\}_1^{n_2}$ are obtained, the norming constants $c_j^d := -\frac{\lambda\overline{B(\overline{p_j^d})}}{a(p_j^d)d'(p_j^d)}$ are computed by Cauchy's integral formula.

4.2 The NLS equation with linearizable boundary conditions

4.2.1 Linearizable boundary conditions

Obtaining $A(k,T)$ and $B(k,T)$ is non-trivial since they are defined in terms of the Dirichlet *and* Neumann data, both of which cannot be arbitrarily specified, for a the well-posed problem [16, 18, 46]. In the special case of linearizable boundary conditions, $A(k,T)$ and $B(k,T)$ can be obtained by solving algebraic equations involving $a(k)$ and $b(k)$ without solving (4.2b) (recall that (4.2b) requires boundary functions $g_0(t)$ and $g_1(t)$). The idea is to use the global relation (4.9) to find extra identities using the symmetries of the dispersion relation similar to the UTM applied to linear PDEs [23]. For the LS equation, the dispersion relation is $\omega(k) = ik^2$ and this is invariant under the mapping $k \to -k$. Similarly, for the NLS equation, we want to determine a relation between $A(k,T), B(k,T)$ and $A(-k,T), B(-k,T)$. Recall that $A(k,T)$ and $B(k,T)$ are defined in terms of $e^{2ik^2T\hat{\sigma}_3}\mu_2(0,T,k)$. Let $\Phi(t,k) = \mu_2(0,t,k)e^{-2ik^2t\sigma_3}$, then $\Phi(t,k)$ satisfies

$$\Phi_t + 2ik^2\sigma_3\Phi = \tilde{Q}(t,k)\Phi, \ \Phi(0,k) = I.$$

Suppose there exists a t-independent, nonsingular matrix $N(k)$ such that

$$\Phi(t,-k) = N(k)\Phi(t,k)N^{-1}(k). \tag{4.23}$$

More explicitly, (4.23) is equivalent to

$$(2ik^2\sigma_3 - \tilde{Q}(t,-k))N(k) = N(k)(2ik^2\sigma_3 - \tilde{Q}(t,k)). \tag{4.24}$$

A necessary condition for the existence of $N(k)$ is that the determinant of $2ik^2\sigma_3 - \tilde{Q}(t,k)$ is even in k. This implies

$$q(0,t)\overline{q}_x(0,t) - \overline{q}(0,t)q_x(0,t) = 0.$$

If this condition is satisfied, (4.24) becomes

$$\begin{aligned}(2kq - iq_x)N_{21} &= \lambda(2k\overline{q} - i\overline{q}_x)N_{12},\\ (2kq + iq_x)N_{11} + (2kq - iq_x)N_{22} &= -2(2ik^2 - i\lambda\left|q\right|^2)N_{12}.\end{aligned}$$

In particular, for the homogeneous Robin boundary condition with a real parameter $\rho > 0$ (this choice of sign is discussed in the end of the section)

$$q_x(0,t) - \rho q(0,t) = 0, \tag{4.25}$$

we choose $N_{12} = N_{21} = 0$ and $(2k - i\rho)N_{22} + (2k + i\rho)N_{11} = 0$ so that

$$A(k,T) = A(-k,T),\ B(k,T) = -\frac{2k + i\rho}{2k - i\rho}B(-k,T),\ k \in \mathbb{C}. \tag{4.26}$$

The results for the homogeneous Dirichlet boundary condition and the homogeneous Neumann boundary condition are obtained by taking $\rho \to \infty$ and $\rho \to 0$ respectively. For instance, for the homogeneous Dirichlet boundary condition, (4.26) becomes

$$A(k,T) = A(-k,T),\ B(k,T) = B(-k,T),\ k \in \mathbb{C}. \tag{4.27}$$

With this, we can solve for $A(k)$ and $B(k)$ in terms of $a(k)$ and $b(k)$ using only algebraic equations. Indeed, if $T = \infty$, the global relation (4.10) gives the following equation valid in the first quadrant,

$$a(k)B(k,\infty) - b(k)A(k,\infty) = 0,\ \arg k \in \left[0, \frac{\pi}{2}\right]. \tag{4.28}$$

Letting $k \to -k$ in the expression for $\overline{d(\overline{k},\infty)}$ in (4.18) and using (4.27) we find a second equation, also valid in the first quadrant:

$$A(k,\infty)\overline{a(-\overline{k})} + \lambda B(k,\infty)\overline{b(-\overline{k})} = \overline{d(-\overline{k},\infty)},\ \arg k \in \left[0,\frac{\pi}{2}\right]. \tag{4.29}$$

Solving both (4.28) and (4.29) for $A(k,\infty)$ and $B(k,\infty)$ yields

$$A(k,\infty) = \frac{a(k)\overline{d(-\overline{k},\infty)}}{\Delta_0(k)},\ B(k,\infty) = \frac{b(k)\overline{d(-\overline{k},\infty)}}{\Delta_0(k)},\ \arg k \in \left[0,\frac{\pi}{2}\right], \tag{4.30}$$

where

$$\Delta_0(k) = a(k)\overline{a(-\overline{k})} + \lambda b(k)\overline{b(-\overline{k})},\ \arg k \in [0,\pi]. \tag{4.31}$$

There is no need to solve for $d(k,\infty)$ in terms of $a(k)$ and $b(k)$ since the jump condition in (4.19) depends only on $B(k,\infty)/A(k,\infty)$.

Example 2 (The RHP associated with homogenous Dirichlet boundary conditions)**.** *With a homogenous Dirichlet boundary condition, we obtain a RHP involving only $a(k)$ and $b(k)$, which are determined solely by the initial condition. We seek a 2×2 matrix-valued function $\Phi(k;x,t)$ that satisfies*

$$\Phi_+(k;x,t) = \Phi_-(k;x,t)J(k;x,t), \tag{4.32}$$

with the jump functions defined in (4.20) on the cross $k \in \mathbb{R}\cup i\mathbb{R}$ shown in Figure 4.1. The only difference is that (4.21c) becomes

$$\Gamma(k) = \frac{-\lambda\overline{b(-\overline{k})}}{a(k)\Delta_0(k)},\ \textit{arg } k \in [0,\pi], \tag{4.33}$$

where $\Delta_0(k)$ is given by (4.31).

Remark 12. *In general, ρ in the homogeneous Robin boundary condition can take any real value [16]. As shown in [50], when $\rho < 0$, generically, there are zeroes of $a(k)$ in the positive imaginary axis. This requires modifications on our assumptions on the RHPs since we do not allow for poles on the jump contour. Meanwhile, the long time behaviour of such solutions*

at $x = 0$ are dominated by oscillatory standing solitons which lead to non-decaying boundary data. The choice of the sign of ρ is also related to the possibility of extending the half-line solution to a bounded whole-line solution, see [13, 38] for further details.

4.2.2 Deformation of the contour based on the method of nonlinear steepest descent

We use the numerical approach developed in [59, 73] to solve the RHP (4.32). Uniform accuracy can be obtained using appropriate deformations of the jump contours. Then, the deformed RHP is solved using the Mathematica package *RHPackage* developed by Olver [59] with spectral accuracy. The deformations are derived in a similar fashion as the deformations used for the solution of the RHP for the NLS equation on the whole line [72]. The idea is to deform the contour near the saddle point to the steepest descent direction so that the oscillations from the exponential factor $e^{2i\theta(k;x,t)}$ change to exponential decay. The saddle point k_0 of the phase $\theta(k;x,t)$ is determined by

$$\frac{d\theta(k;x,t)}{dk}\Big|_{k=k_0} = 0 \Rightarrow k_0 = -\frac{x}{4t}.$$

We write the exponent as

$$2i\theta(k;x,t) = -\frac{ix^2}{4t} + 4it(k-k_0)^2.$$

Thus $e^{2i\theta(k;x,t)}$ is exponentially decaying if k follows a path with $\arg(k-k_0) = \pi/4, 5\pi/4$. In addition, the deformation of contours requires that the functions $\gamma(k), \Gamma(k)$ are analytic in the neighbourhood of k_0. Since $q_0 \in \mathcal{S}_\alpha(\mathbb{R}^+)$, $a(k)$ and $b(k)$ are analytic and bounded for $\mathrm{Im}\,(k) \geq -\alpha/2$. To ensure that the residue condition is outside the region in which the contour is deformed, if $0 \leq \min(\{\mathrm{Im}\left(p_j^a\right)\}_{j=1}^n) \leq \alpha/2$, we redefine $\alpha = \min(\{\mathrm{Im}\left(p_j^a\right)\}_{j=1}^n)/4$. Therefore, $\gamma(k)$ is bounded and analytic in a strip centered around the real axis with $-\alpha/2 \leq \mathrm{Im}\,(k) \leq \alpha/2$, while $\Gamma(k)$ is bounded and analytic for $\mathrm{Im}\,(k) \geq -\alpha/2$. In some cases, if $\tau(k)$ in (4.34) vanishes in the strip, then we need to further shrink the width of the strip. Since $\tau(k) \geq 1$ on the real axis, we can always find a valid choice for $\alpha > 0$. We introduce the following deformation steps for the contour of the RHP (4.32).

Step 1: deformations based on steepest descent directions

Define $\mathcal{R}_{k,\theta} = \{k + re^{i\theta} : r \geq 0\}$. The jump matrix $J_4(k;x,t)$ has the factorization

$$\begin{aligned} J_4(k;x,t) &= \begin{bmatrix} 1+\lambda\gamma(k)\overline{\gamma(\overline{k})} & \gamma(k)e^{-2i\theta(k;x,t)} \\ \lambda\overline{\gamma(\overline{k})}e^{2i\theta(k;x,t)} & 1 \end{bmatrix} \\ &= \begin{bmatrix} 1 & \gamma(k)e^{-2i\theta(k;x,t)} \\ 0 & 1 \end{bmatrix} \begin{bmatrix} 1 & 0 \\ \lambda\overline{\gamma(\overline{k})}e^{2i\theta(k;x,t)} & 1 \end{bmatrix} = MP. \end{aligned}$$

This factorization provides $J_4(k;x,t)$ with decay away from k_0 as, by replacing the contour on the real line with two oblique rays starting from k_0. Then M approaches the identity matrix exponentially fast in the lower half-plane along $\mathcal{R}_{k_0,7\pi/4}$ and P approaches the identity matrix exponentially fast in the upper half-plane along $\mathcal{R}_{k_0,\pi/4}$. However, for $\mathrm{Re}\,(k) < \mathrm{Re}\,(k_0)$, the exponentials in M and P are growing for M along $\mathcal{R}_{k_0,5\pi/4}$ in the lower half-plane and P along $\mathcal{R}_{k_0,3\pi/4}$ in the upper half-plane. Alternatively, $J_2(k;x,t)$ has the factorization

$$\begin{aligned} J_2(k;x,t) &= \begin{bmatrix} 1 & -\left(\lambda\overline{\Gamma(\overline{k})}+\gamma(k)\right)e^{-2i\theta(k;x,t)} \\ -\left(\lambda\overline{\gamma(\overline{k})}+\Gamma(k)\right)e^{2i\theta(k;x,t)} & 1+\left(\lambda\overline{\Gamma(\overline{k})}+\gamma(k)\right)\left(\lambda\overline{\gamma(\overline{k})}+\Gamma(k)\right) \end{bmatrix} \\ &= \begin{bmatrix} 1 & 0 \\ -\left(\lambda\overline{\gamma(\overline{k})}+\Gamma(k)\right)\frac{e^{2i\theta(k;x,t)}}{\tau(k)} & 1 \end{bmatrix} \begin{bmatrix} \frac{1}{\tau(k)} & 0 \\ 0 & \tau(k) \end{bmatrix} \begin{bmatrix} 1 & -\left(\lambda\overline{\Gamma(\overline{k})}+\gamma(k)\right)\frac{e^{-2i\theta(k;x,t)}}{\tau(k)} \\ 0 & 1 \end{bmatrix} \\ &= LDU, \end{aligned}$$

where

$$\tau(k) = 1 + \left(\lambda\overline{\gamma(\overline{k})}+\Gamma(k)\right)\left(\lambda\overline{\Gamma(\overline{k})}+\gamma(k)\right),\ \mathrm{Im}\,(k) \leq \frac{\alpha}{2}. \tag{4.34}$$

This factorization provides $J_2(k;x,t)$ with decay for increasing t as, for $\mathrm{Re}\,(k) < \mathrm{Re}\,(k_0)$, L approaches the identity matrix exponentially fast along $\mathcal{R}_{k_0,5\pi/4}$ in the lower half-plane and U approaches the identity matrix exponentially fast along $\mathcal{R}_{k_0,3\pi/4}$ in the upper half-plane. We obtain the RHP

$$\Phi_+(k;x,t) = \Phi_-(k;x,t)H(k;x,t), \tag{4.35}$$

with jump functions

$$H(k;x,t)=\begin{cases} M(k;x,t), & \{k\in\mathcal{R}_{k_0,7\pi/4}:|\mathrm{Im}\,(k)|\le\alpha/2\}\cup\{k=k_0+\frac{\alpha}{2}e^{-i\frac{\pi}{4}}+s,\ s\ge 0\},\\ P(k;x,t), & \{k\in\mathcal{R}_{k_0,\pi/4}:|\mathrm{Im}\,(k)|\le\alpha/2\}\cup\{k=k_0+\frac{\alpha}{2}e^{i\frac{\pi}{4}}+s,\ s\ge 0\},\\ J_1(k;x,t), & \{k\in\mathcal{R}_{k_0,\pi/4}\},\\ L(k;x,t), & \{k\in\mathcal{R}_{k_0,5\pi/4}:|\mathrm{Im}\,(k)|\le\alpha/2\}\cup\{k=k_0+\frac{\alpha}{2}e^{i\frac{5\pi}{4}}-s,\ s\ge 0\},\\ D(k;x,t), & \{k\in\mathbb{C}:k=k_0-s,\ s\ge 0\},\\ U(k;x,t), & \{k\in\mathcal{R}_{k_0,3\pi/4}:|\mathrm{Im}\,(k)|\le\alpha/2\}\cup\{:k=k_0+\frac{\alpha}{2}e^{i\frac{3\pi}{4}}-s,\ s\ge 0\},\\ J_3(k;x,t), & \{k\in\mathcal{R}_{k_0,7\pi/4}\}, \end{cases} \tag{4.36}$$

and the deformed contour, with orientation, is shown in Figure 4.3.

Step 2: deformations for uniform accuracy

Similar to the RHP for the whole-line problem in [72], the errors for computing the solution of RHP (4.35) are not uniformly small for large time since not all jumps decay to the identity matrix away from the saddle point k_0. For large t, although the jump matrix D along the negative real axis does not contain oscillatory exponentials, the solution of the RHP (4.35) has increasing oscillations along the jump contour for $k<k_0$ as t grows. Therefore we remove the jump matrix D using conjugation [72]. We introduce the matrix-valued function $\Delta(k,k_0)$,

$$\Delta(k,k_0)=\begin{bmatrix}\delta(k,k_0) & 0\\ 0 & \delta^{-1}(k,k_0)\end{bmatrix},$$

where

$$\delta(k,k_0)=\exp\left(\frac{1}{2\pi i}\int_{-\infty}^{k_0}\frac{\log\tau(z)}{z-k}dz\right).$$

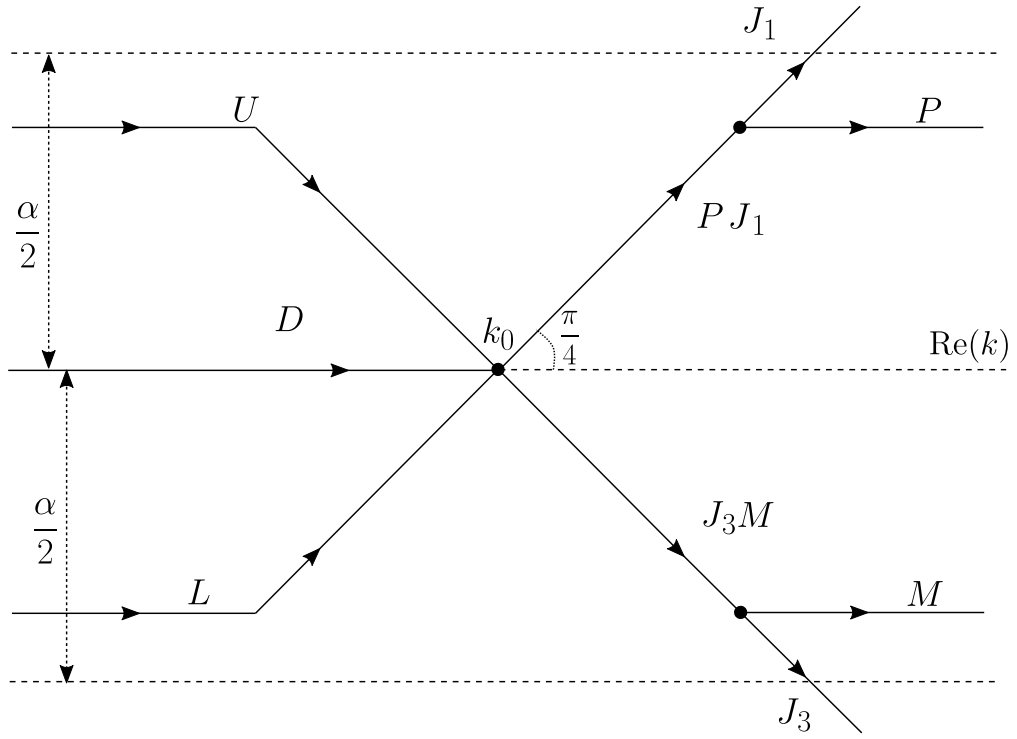

Figure 4.3: The deformed contour for the RHP (4.35) in the complex k-plane near the saddle point k_0 for the method of nonlinear steepest descent.

Then, $\Psi(k;x,t) = \Phi(k;x,t)\Delta^{-1}(k,k_0)$ is continuous across the real axis for $\mathrm{Re}\,(k) \neq \mathrm{Re}\,(k_0)$, and satisfies

$$\Psi_+(k;x,t) = \Psi_-(k;x,t)\Delta(k,k_0)H(k;x,t)\Delta^{-1}(k,k_0) = \Psi_-(k;x,t)\tilde{H}(k;x,t),$$

Since $\delta(k,k_0)$ is singular at k_0, lensing is used to avoid the singularity by introducing new jump conditions on a square around k_0, as shown in Figure 4.4. The length of the side of the square is $O(1/\sqrt{t})$ for large t. See [72] for further details of the scaling. Summarizing all deformations, we have the RHP

$$\Psi_+(k;x,t) = \Psi_-(k;x,t)\tilde{H}(k;x,t), \tag{4.37}$$

where the jump contours are shown in Figure 4.4.

Step 3: Adding residue conditions

For the focusing NLS equation, there is an additional step for the residue conditions (4.22a)-(4.22d). By introducing small circles centered at the singularities, and modifying the unknown function Ψ inside the circle, the residue conditions are replaced with jump conditions on the circles [72]. Let $\{z_j\}_{1=j}^{n_1+n_2}$ be the union of the zeroes of $a(k)$ and $d(k,T)$ defined by $z_j = p_j^a$, for $1 \leq j \leq n_1$ and $z_j = p_{j-n_1}^d$, for $n_1+1 \leq j \leq n_1+n_2$. Let $\{c_j\}_{1=j}^{n_1+n_2}$ be the associated norming constants defined by $c_j = c_j^a, 1 \leq j \leq n_1$ and $c_j = c_{j-n_1}^d, n_1+1 \leq j \leq n_1+n_2$. For a residue condition at $k = z_j$ in the upper half-plane,

$$\Psi^+(k;x,t) = \Psi^-(k;x,t)\begin{pmatrix} 1 & 0 \\ c_j e^{2i\theta(z_j;x,t)}/(k-z_j) & 1 \end{pmatrix}, \tag{4.38}$$

is the jump condition on a circle centered at z_j with radius ε oriented counterclockwise. The circles need to avoid intersections with contours already present in the RHP. The corresponding residue condition at $k = \overline{z_j}$ in the lower half-plane becomes

$$\Psi^+(k;x,t) = \Psi^-(k;x,t)\begin{pmatrix} 1 & -\overline{c_j} e^{-2i\theta(\overline{z_j};x,t)}/(k-\overline{z_j}) \\ 0 & 1 \end{pmatrix}, \tag{4.39}$$

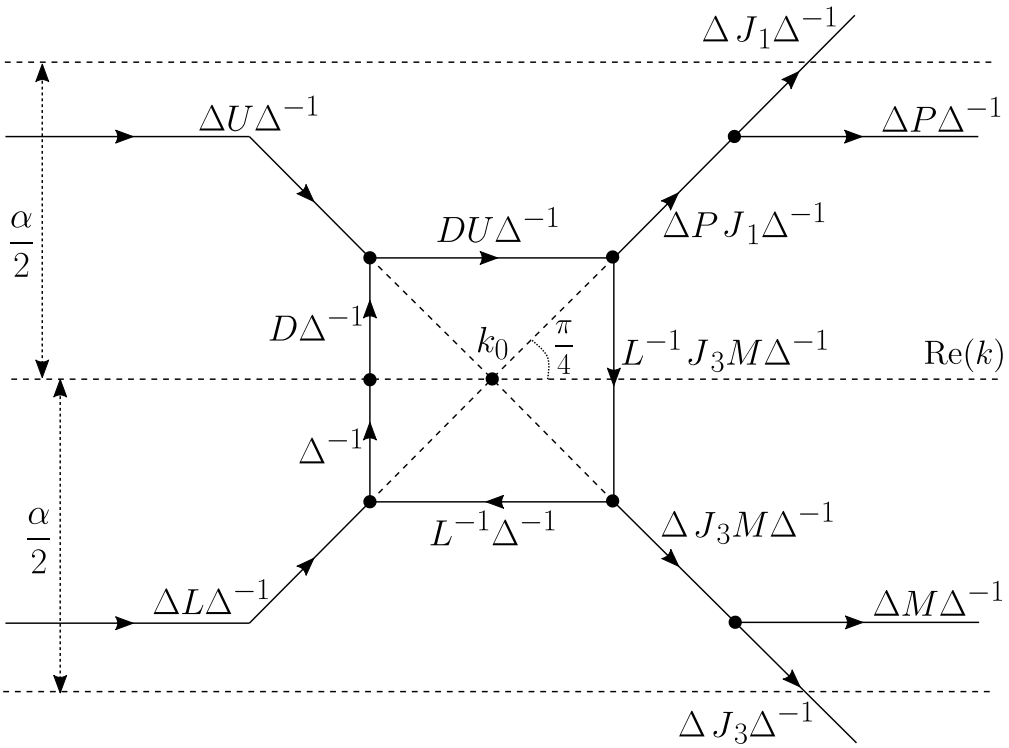

Figure 4.4: The deformed contour for the RHP (4.37) in the complex k-plane near the saddle point k_0 after removing the jump on the negative real axis. All jumps away from k_0 approach the identity exponentially fast as $t \to \infty$. The length of the side of the square is on the order of $O(1/\sqrt{t})$ for large t.

on a circle centered at $\overline{z_j}$ with radius ε. Since $\left|c_j e^{2i\theta(z_j;x,t)}\right|$ may be unbounded for large x,t, we invert this factor through a deformation when $\left|c_j e^{2i\theta(z_j;x,t)}\right| > 1$. We define the matrix-valued function $\hat{\Psi}(k;x,t)$ by

$$\hat{\Psi}(k;x,t) = \Psi(k;x,t)\begin{cases} \begin{pmatrix} 1 & \frac{-(k-z_j)}{c_j e^{2i\theta(z_j;x,t)}} \\ \frac{c_j e^{2i\theta(z_j;x,t)}}{k-z_j} & 0 \end{pmatrix} V(k), & \text{if } |k-z_j|<\varepsilon, \\ \begin{pmatrix} 0 & \frac{-\overline{c_j} e^{-2i\theta(\overline{z_j};x,t)}}{k-\overline{z_j}} \\ \frac{k-\overline{z_j}}{\overline{c_j} e^{-2i\theta(\overline{z_j};x,t)}} & 1 \end{pmatrix} V(k), & \text{if } |k-\overline{z_j}|<\varepsilon, \\ V(k), & \text{otherwise,} \end{cases} \tag{4.40}$$

where

$$v(z) = \prod_{j\in K_{x,t}} \frac{k-z_j}{k-\overline{z_j}} \quad \text{and} \quad V(z) = \begin{pmatrix} v(z) & 0 \\ 0 & 1/v(z) \end{pmatrix},$$

for each j in the set $K_{x,t} = \{j : \left|c_j e^{2i\theta(z_j;x,t)}\right| > 1\}$ that contains the indexes of the zeros of $a(k)$ and $d(k,T)$ whose jump matrices need to be inverted. Then $\hat{\Psi}(k;x,t)$ satisfies the jump conditions

$$\hat{\Psi}_+(k;x,t) = \hat{\Psi}_-(k;x,t)V^{-1}(k)\tilde{H}(k;x,t)V(k),$$

on the same contours as (4.37). In addition, $\hat{\Psi}(k;x,t)$ satisfies the jump conditions circles around $\{z_j\}_{1=j}^{n_1+n_2}$,

$$\hat{\Psi}^+(k;x,t) = \begin{cases} \hat{\Psi}^-(k;x,t)V^{-1}(k) \begin{pmatrix} 1 & -(k-z_j)/(c_j e^{2i\theta(z_j;x,t)}) \\ 0 & 1 \end{pmatrix} V(k), & \text{if } |k-z_j|=\varepsilon, \\ \hat{\Psi}^-(k;x,t)V^{-1}(k) \begin{pmatrix} 1 & 0 \\ (k-\overline{z_j})/(\overline{c_j} e^{-2i\theta(\overline{z_j};x,t)}) & 1 \end{pmatrix} V(k), & \text{if } |k-\overline{z_j}|=\varepsilon. \end{cases}$$

With all deformations, the RHP (4.37) is solved using *RHPackage* [59] after truncating the contours along which the jump matrices are close to the identity matrix. In practice, this tolerance is set to 10^{-9} unless otherwise stated. For convenience, we also truncate the contours if they are outside a disk centered at the origin with radius 50. In most cases, the

truncation errors are on the same order of the tolerance since the jump matrix approaches the identity matrix exponentially fast. When x, t are small, the truncation error dominates. We discuss how to control the truncation error in Section 4.4.5.

4.2.3 Numerical results

In Figure 4.5, we plot the real part of the solution to the defocusing NLS equation on the half-line with homogenous Dirichlet boundary condition at $x = 0$ and the initial condition $q(x, 0) = xe^{-x^2}$. We observe dispersive waves propagating to the right from the localized initial condition. We plot the solution for $0 \leq x \leq 10$ and $0.1 \leq t \leq 3.5$. The domain is chosen to be bounded away from $t = 0$ as the NUTM is less efficient there. In addition, when the UTM is applied to linear PDEs on the half-line, the solution formula requires principle-value integrals to evaluate at $x = t = 0$ [26]. This also happens when using the UTM to the NLS equation at $x = t = 0$. The UTM is well-defined for any $x > 0$ or $t > 0$ but the numerics suffer from slow convergence when x, t are small. The details are discussed in Section 4.4.5. In general, traditional time-stepping methods work well for small t. If needed, a combination of the NUTM and traditional methods works for both small time and large time.

4.3 The NLS equation with nonlinearizable boundary conditions

4.3.1 Overdetermined boundary conditions

Another possible way to avoid computing the unknown boundary condition is to specify both boundary functions $g_0(t)$ and $g_1(t)$, provided and they are admissible with respect to the given initial condition $q_0(x)$. However, there are obstacles to computing the associated solution efficiently:

1. For a generic whole-line solitonless solution $q(x, t)$ with a nontrivial reflection coefficient $\rho(k) = b(k)/a(k) \neq 0$, one has $q(0, t) \sim t^{-1/2}$ and $q_x(0, t) \sim t^{-3/2}$ as $t \to \infty$ [34]. Therefore, in general, for half-line problems the Dirichlet and Neumann data do not

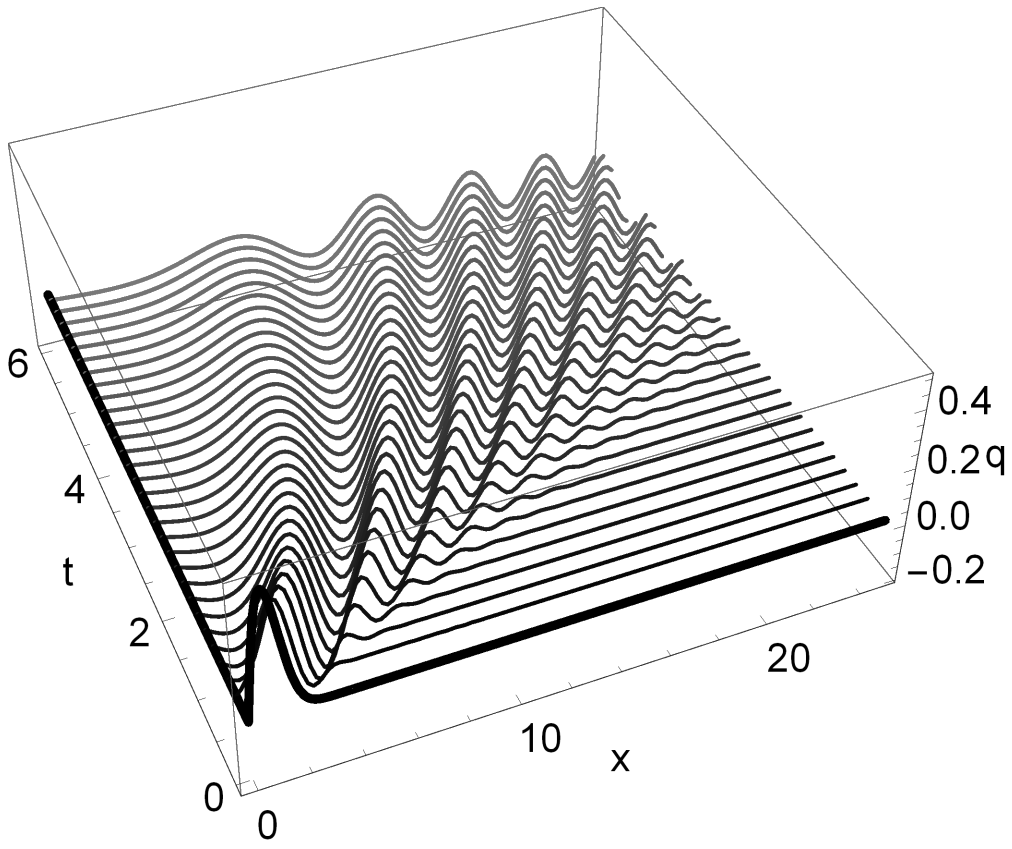

Figure 4.5: The real part of $q(x,t)$ with homogenous Dirichlet boundary condition $q(0,t)=0$ and the initial condition $q(x,0)=xe^{-x^2}$. The thick curves show the initial and boundary conditions.

both decay exponentially. This affects the regions where the contours can be deformed. For instance, in the $T = \infty$ case, $A(k, \infty)$ and $B(k, \infty)$ are only guaranteed to be analytic in the first and third quadrants. Therefore, jump contours , which depend on $\tau(k)$ defined in (4.34) cannot be deformed away from the real axis and the method of nonlinear steepest descent cannot be applied directly. These undeformed contours become highly oscillatory as t increases. For linear PDEs, numerical methods such as Levin's method can be used to compute the oscillatory integrals with high accuracy [26]. For nonlinear integrable PDEs, efficient numerical methods for oscillatory singular integral equations from the RHP are not as well developed [69]. A complete discussion of this is beyond our scope.

2. For pure whole-line soliton solutions that have non-zero velocity, $q(0,t)$ and $q_x(0,t)$ decay exponentially. In this case, the focusing NLS equation allows right-going soliton solutions whose parameters correspond to zeroes of $d(k,T)$ in the second quadrant. As discussed in Section 4.1.5, this step requires root-finding algorithms.

There are solutions, with compatible q_0, g_0, g_1, that do not suffer from (1) and (2). We can compute these solutions efficiently. Such solutions include left-going singular solutions of the defocusing NLS equation, known as positons, or left-going soliton solutions of the focusing NLS equation.

Such solutions have analytical expressions and are used to demonstrate the accuracy of the NUTM. In fact, unlike the whole line problem, the jump function (4.20) in the half-line problem is non-trivial even when the solution does not contain dispersion. For instance, suppose the initial and boundary values are prescribed by the one-positon solution of the defocusing NLS equation [73]

$$q(x,t) = 2\eta e^{-4it(\xi^2-\eta^2)-2ix\xi-i\phi_0}\ \mathrm{csch}(2\eta(4t\xi + x - x_0)),$$

where ξ, η, x_0, ϕ_0 are constants. The positon is left-going if $\xi > 0$. If $x_0 < 0$ the singularity is outside the domain for all $t \geq 0$, therefore $q(x,t)$ is exponentially localized and smooth

for $x, t \geq 0$. This positon solution corresponds to a simple zero of $a(k)$ at $k_1 = \xi + i\eta \tanh(2\eta x_0)$ [52]. The assumptions $\xi > 0$ and $x_0 < 0$ imply that k_1 is not in the first quadrant so no residue conditions are required for formulating the associated RHP. Similarly, suppose the initial and boundary values are obtained from the one-soliton solution of the focusing NLS equation [73],

$$q(x,t) = 2\eta e^{-4it(\xi^2-\eta^2)-2ix\xi-i\phi_0} \operatorname{sech}(2\eta(4t\xi + x - x_0)). \tag{4.41}$$

This soliton corresponds to a simple zero of $a(k)$ at $k_1 = \xi + i\eta \tanh(2\eta x_0)$. If the initial position of the center of the soliton lies outside of the domain (*i.e.,* $x_0 < 0$) and it is left-going (*i.e.,* $\xi < 0$), the soliton is represented by the continuous part of the spectral data and no residue conditions are used. On the other hand, for the focusing NLS equation, it is possible to allow $x_0 > 0$. In this case, k_1 is in the first quadrant and residue conditions are required:

$$\operatorname{Res}_{k=k_1} \Phi(k;x,t) = \lim_{k\to k_1} \Phi(k;x,t) \begin{pmatrix} 0 & 0 \\ c_1 e^{2i\theta(k_1;x,t)} & 0 \end{pmatrix},$$

$$\operatorname{Res}_{k=\overline{k_1}} \Phi(k;x,t) = \lim_{k\to \overline{k_1}} \Phi(k;x,t) \begin{pmatrix} 0 & -\overline{c_1} e^{-2i\theta(\overline{k_1};x,t)} \\ 0 & 0 \end{pmatrix},$$

where $c_1 = 1/(a'(k_1)b(k_1))$ is the norming constant. These considerations can be generalized to n-positon and n-soliton solutions.

Figure 4.6 shows the error plots of the solution using the NUTM with the initial and boundary values given by (4.41) with $\xi = 1, \eta = 1, x_0 = 0.4$ along different lines in the x, t quarter plane. The spectral convergence of the NUTM is demonstrated by the errors with fixed x, t and varying N, the number of collocation points used in the solution of the RHP. The absolute errors are uniformly controlled and decreasing for increasing x, t with fixed N. For increasing t, the NUTM even maintains relative accuracy with N fixed, but sufficiently large. Although the absolute errors decrease exponentially for fixed t, the exponential decay rate of the solution is not captured exactly. As a result, the relative error with fixed t increases as x grows. This is expected and it is due to the fact that the jump matrix after

deformation decays to the identity exponentially but not exactly at the decay rate of the solution. Indeed, how far we can deform the contour is restricted by the region of analyticity of $\gamma(k)$ and $\Gamma(k)$. For instance, when $q_0 \in \mathcal{S}_{2\alpha}$, $\gamma(k)$ is analytic within $-\alpha \leq \mathrm{Im}\,(k) \leq \alpha$, along a horizontal segment of the contour $k = s + i\alpha$,

$$e^{2i\theta(k;x,t)} = e^{-8s\alpha t - 2\alpha x + i(4(s^2-\alpha^2)t + 2sx)}.$$

This is to be compared with the situation for the 1-soliton solution (4.41) which has a exponential decay rate 2η in the x direction. The zeroes of $a(k)$ are outside the strips $-\alpha \leq \mathrm{Im}\,(k) \leq \alpha$, since $|\alpha| < |\eta \tanh(2\eta x_0)| < |\eta|$. To capture the same exponential decay rate, a deformation of the horizontal contours up to the pole of $\gamma(k)$ at $k = \xi + i\eta \tanh(2\eta x_0)$ is necessary. The restriction is not required if t is sufficiently large, in which case the jump matrix along the deformed contour approaches the identity and is truncated before $\mathrm{Im}(k) = \eta \tanh(2\eta x_0)$. For instance, consider the jump functions related to P in Figure 4.4. When t is sufficiently large, the jump function $\Delta P \Delta^{-1}$ in the top right corner of Figure 4.4 is close to the identity matrix and is negligible. After the truncation, only the jump function $\Delta P J_1 \Delta^{-1}$ remains.

4.3.2 Boundary conditions implicitly determined by given spectral data $A(k,T)$ and $B(k,T)$

A dressing argument

If $A(k,T)$ and $B(k,T)$ are given directly, the deformation steps discussed in Section 4.2 can still be performed provided that the deformations are within the regions where $A(k,T)$ and $B(k,T)$ are analytic. From the idea of the dressing method, as long as the spectral functions $A(k,T)$ and $B(k,T)$ satisfy (4.5b) and (4.9), the RHP (4.19) generates solutions to the NLS equation.

Proposition 1 (The dressing method [35])**.** *Suppose that the oriented smooth curve $\mathcal{L}$ divides the complex k-plane into the domains D^+ and D^-. Let $M^+(k;x,t)$ satisfy the following 2×2*

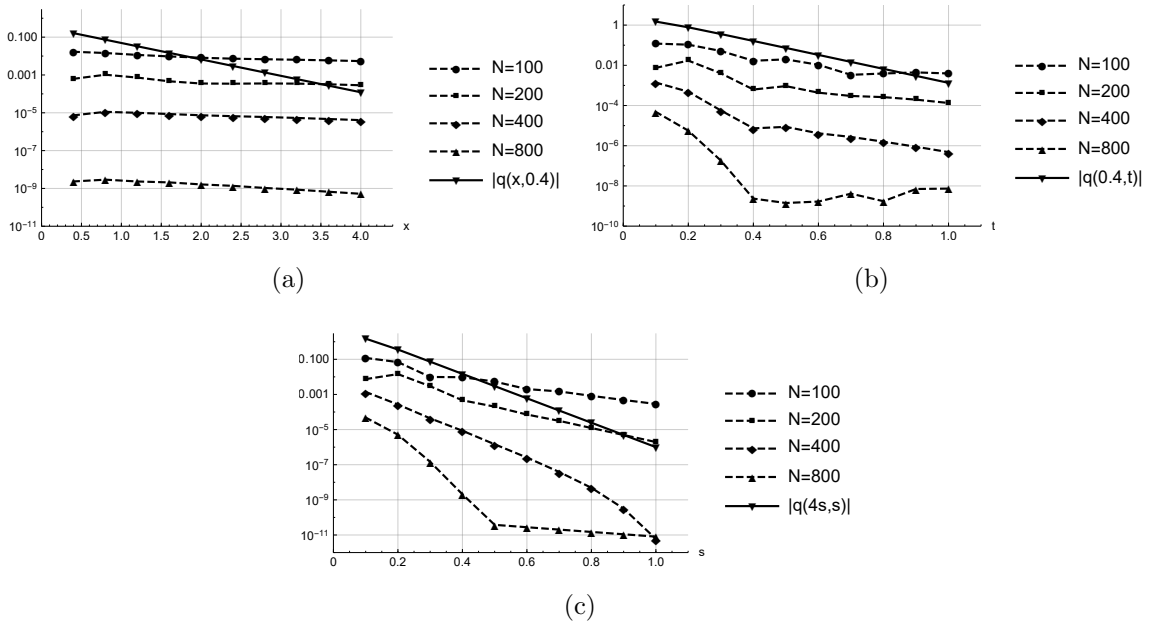

Figure 4.6: The absolute value of the exact one-soliton solution (4.41) with $\xi = 1, \eta = 1, x_0 = 0.4$ (solid lines) and the absolute errors of the numerical solution with different numbers of collocation points N (dashed lines). Panel (a) shows the evaluations for $x \in [0.4, 4], t = 0.4$. Panel (b) shows the evaluations for $x = 0.4, t \in [0.1, 1]$. Panel (c) shows the evaluations for $x = 4s, t = s, s \in [0.1, 1]$. The tolerance of the error from computation of the spectral functions and contour truncations is set to 10^{-9}.

matrix RHP in the complex k-plane for all $x, t > 0$*,*

$$M^+(k; x, t) = M^-(k; x, t)e^{-i(kx+2k^2t)\hat{\sigma}_3}J(k),\ k \in \mathcal{L},$$

where $J(k)$ *is a* 2×2 *unimodular matrix with* $J_{11} = 1$ *or*

$$J_{22} = 1$$

. Assume that the above RHP has a unique solution which is sufficiently smooth for all $x, t > 0$*. Define* $Q(x, t)$ *by*

$$Q(x, t) = i \lim_{k\to\infty}[\sigma_3, kM(x, t, k)],$$

then $Q(x, t)$ *satisfies the nonlinear equation*

$$iQ_t - Q_{xx}\sigma_3 + 2Q^3\sigma_3 = 0.$$

To ensure that (4.5b) is satisfied, we specify the ratio $h(k) = B(k)/A(k)$ for $k \in D_3$ since this is the quantity required in (4.19). Then the spectral data $A(k)$ and $B(k)$ are defined implicitly from (4.5b),

$$1 + \lambda h(k)\overline{h(\overline{k})} = \frac{1}{A(k)\overline{A(\overline{k})}},\ k \in \mathbb{R} \cup i\mathbb{R}.$$

Remark 13. *The global relation (4.10) determines the value of* $h(k)$ *in the first quadrant. If* $T = \infty$*,* $h(k) = b(k)/a(k)$ *provided that* $a(k) \neq 0$*.*

Numerical results

We solve the focusing NLS equation on the half-line with initial condition $q_0(x) = 0$ and $B(k)/A(k) = 1000k/\left(k - 2(1 + i)\right)^5$ for $\arg(k) \in [\pi, 3\pi/2]$. In this case, $\gamma(k) = 0$ and $\Gamma(k) = 1000k/\left(k - 2(1 - i)\right)^5$. Furthermore, we impose two residue conditions at $k_1 = -1+i$ and $k_2 = -2 + i$ with corresponding norming constants $c_1 = 100000, c_2 = 2$. The constant 1000 is chosen so that the dispersion is on the same order of the solitons for small x, t. We plot the real part and the absolute value of the solution for $0 \leq x \leq 20$ and $0.1 \leq t \leq 3$ in

Figure 4.7. The solution contains two right-going solitons as well as dispersion. Two slices of the solution at $t = 0.1$ and $t = 2.9$ are shown in Figure 4.8. We also observe that the solution approximates the exact two-soliton with the envelope plotted in dashed lines. Using the parameters $\{z_1 = -1 + i, z_2 = -2 + i, s_1 = \frac{2}{c_1}e^{-i(\pi/2-0.3)}, s_2 = \frac{2}{c_2}e^{i(\pi/2+0.5)}\}$, the exact two-soliton solution [77] is defined by

$$q_{\text{2-soliton}}(x - 0.4, t) = -2i\frac{\det F}{\det M}, \tag{4.42}$$

where

$$M = \begin{pmatrix} \left(e^{-\phi(z_1)-\overline{\phi(z_1)}} + \overline{s_1}s_1e^{\phi(z_1)+\overline{\phi(z_1)}}\right)/(\overline{z_1} - z_1) & \left(e^{-\phi(z_2)-\overline{\phi(z_1)}} + \overline{s_1}s_2e^{\phi(z_2)+\overline{\phi(z_1)}}\right)/(\overline{z_1} - z_2) \\ \left(e^{-\phi(z_1)-\overline{\phi(z_2)}} + \overline{s_2}s_1e^{\phi(z_1)+\overline{\phi(z_2)}}\right)/(\overline{z_2} - z_1) & \left(e^{-\phi(z_2)-\overline{\phi(z_2)}} + \overline{s_2}s_2e^{\phi(z_2)+\overline{\phi(z_2)}}\right)/(\overline{z_2} - z_2) \end{pmatrix},$$

$$F = \begin{pmatrix} 0 & e^{-\overline{\phi(z_1)}} & e^{-\overline{\phi(z_2)}} \\ s_1e^{\phi(z_1)} & M_{11} & M_{21} \\ s_2e^{\phi(z_2)} & M_{12} & M_{22} \end{pmatrix},$$

$$\phi(z) = -i\theta(x, t, z).$$

In the long time regime, the 2-soliton solution (4.42) separates into two right-going 1-soliton solutions described by (4.41). The interaction between the solitons and the dispersion affects the parameters of their initial phases and initial positions. The change in the initial phase $\Delta_{\phi_0}|_{k_j}$ of the 1-soliton solution corresponding to the zero of $d(k_j) = 0$, $k_j = \xi_j + i\eta_j$ in the second quadrant is given by [37]

$$\Delta_{\phi_0}|_{k_j} = \frac{1}{\pi}\int_{-\infty}^{\xi_j} \frac{\log\left(1 + \lambda\left|\gamma(k) + \lambda\overline{\Gamma(k)}\right|^2\right)}{(\mu - \xi_j)^2 + \eta_j^2}(\mu - \xi_j)d\mu,$$

and in our example, $\xi_1 + i\eta_1 = -1 + i$ and $\xi_2 + i\eta_2 = -2 + i$,

$$\Delta_{\phi_0}|_{k_1} \approx -0.236191, \quad \Delta_{\phi_0}|_{k_2} \approx -0.107931.$$

The change in the initial position $\Delta_{x_0}|_{k_j}$ of the 1-soliton solution corresponding to the zero of $d(k_j) = 0$, $k_j = \xi_j + i\eta_j$ in the second quadrant is given by [37]

$$\Delta_{x_0}|_{k_j} = -\frac{\eta_j}{\pi}\int_{-\infty}^{\xi_j} \frac{\log\left(1+\lambda\left|\gamma(k)+\lambda\overline{\Gamma(k)}\right|^2\right)}{(\mu-\xi_j)^2+\eta_j^2}d\mu,$$

and in our example, $\xi_1 + i\eta_1 = -1 + i$ and $\xi_2 + i\eta_2 = -2 + i$,

$$\Delta_{x_0}|_{k_1} \approx -0.354645, \quad \Delta_{x_0}|_{k_2} \approx -0.180415.$$

We compare our solution with the large t asymptotics along $x/t = 2, 6, 10$ in Figure 4.9. Away from the solitons, the large t asymptotics along $x/t = O(1)$ are described by (see [34])

$$q(x,t) = t^{-1/2}\alpha\left(-\frac{x}{4t}\right)\exp\left(\frac{ix^2}{4t}+2i\lambda\alpha^2\left(-\frac{x}{4t}\right)\log t + i\phi\left(-\frac{x}{4t}\right)\right)+o\left(t^{-\frac{1}{2}}\right), \quad \text{as} \quad t\to\infty, \tag{4.43}$$

where the amplitude α and the phase ϕ are given by

$$\begin{aligned}
\alpha^2(k) =& \frac{\lambda}{4\pi}\log\left(1+\lambda\left|\gamma(k)+\lambda\overline{\Gamma(k)}\right|^2\right),\\
\phi(k) =& 6\lambda\alpha^2(k)\log 2 + \frac{\pi(2+\lambda)}{4} + \arg\left(\gamma(k)+\lambda\overline{\Gamma(k)}\right) + \arg\Gamma(-2i\lambda\alpha^2(k))\\
&+ 4\lambda\int_{-\infty}^{k}\log|\mu-k|\,d\alpha^2(\mu).
\end{aligned}$$

In practice, to avoid computing the integral in the formula for the phase ϕ, since ϕ is constant with fixed x/t, we estimate ϕ by choosing ϕ so that the errors in Figure (4.9d) show a trend of decreasing errors with order $O(1/t)$.

4.4 Large k asymptotics of the spectral functions

In this section we consider the large k asymptotics of the spectral functions $a(k), b(k)$, $A(k,\infty), B(k,\infty)$ and $A(k,T), B(k,T)$. It is known that the global relation characterizes the initial and boundary data from a solution to the NLS equation while the large k asymptotics of the global relation characterizes the compatibility of initial and boundary data at $x = 0$

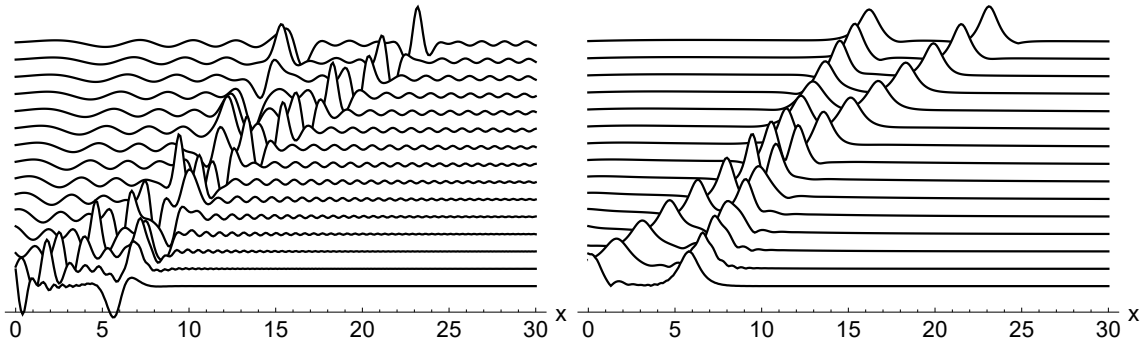

Figure 4.7: The numerical solution $q(x,t)$ on the domain $0 \leq x \leq 30$ and $0.1 \leq t \leq 3$ with spectral functions specified in Section 4.3. The solution contains two right-going solitons as well as dispersion. Left: The real part of $q(x,t)$. Right: The absolute value of $q(x,t)$.

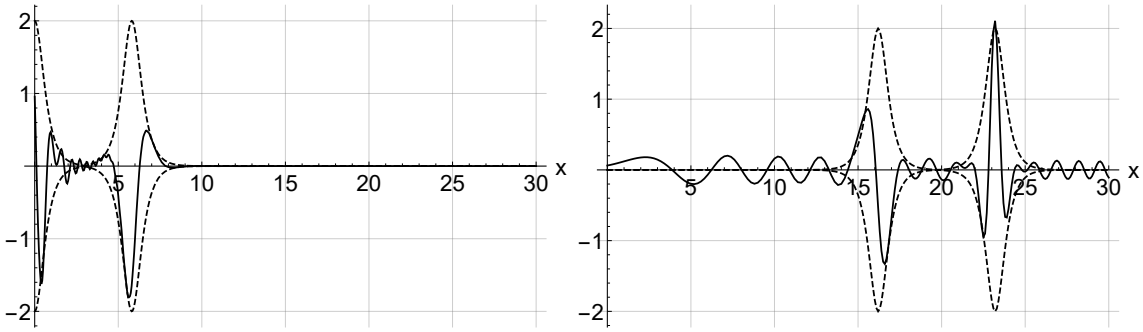

Figure 4.8: The real part of $q(x,t)$ (solid curve) with the envelope of the right-going 2-soliton (dashed curve). Left: $q(x,0.1)$. Right: $q(x,2.9)$.

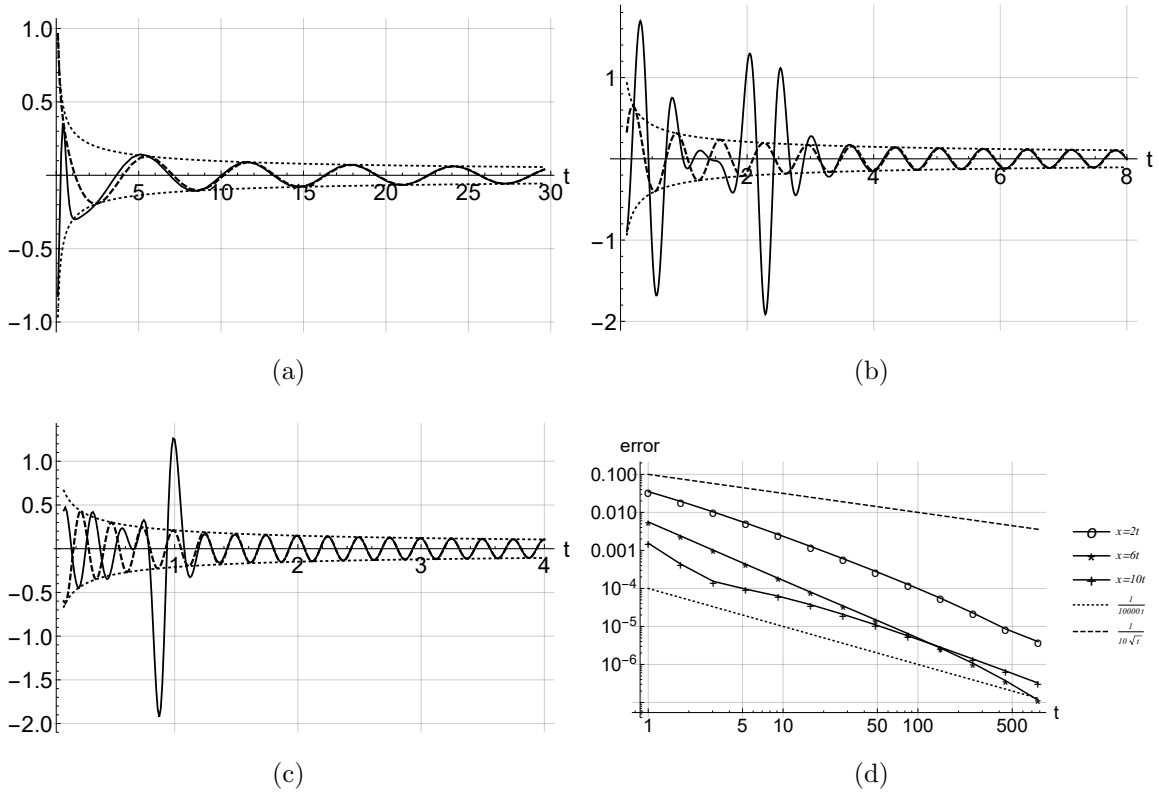

Figure 4.9: The real part of the numerically computed $q(x,t)$ (solid curve), the real part of the dispersive wave from the asymptotic formula (4.43) (dashed curves) and its envelope (dotted curves). Panel (a) shows the evaluations along $x = 2t$. Panel (b) shows the evaluations along $x = 6t$. Panel (c) shows the evaluations along $x = 10t$. Panel (d) shows the errors compared with the asymptotic formula (4.43).

and $t = 0$ [47]. Some of these asymptotic results can be found in [39]. We reexamine these results with more terms, computing them with examples from the LS equation, and using them to improve the decay of the jump matrix for the RHP (4.19). The initial data $q_0(x)$ and the boundary data $g_0(t), g_1(t)$ are assumed to have sufficient smoothness and decay at infinity so that the relevant integrals are well-defined.

4.4.1 Large k asymptotics of $a(k), b(k)$

Recall that the spectral functions $a(k) = \phi_2(0,k)$ and $b(k) = \phi_1(0,k)$ are defined using the linear Volterra integral equations (4.6a) and (4.6b). We use the following expansions for large k in the upper half-plane $\mathrm{Im}\,(k) \geq 0$,

$$\phi_1(x,k) = \frac{f_{11}(x)}{k} + \frac{f_{12}(x)}{k^2} + O\left(\frac{1}{k^3}\right), \tag{4.44a}$$

$$\phi_2(x,k) = 1 + \frac{f_{21}(x)}{k} + O\left(\frac{1}{k^2}\right). \tag{4.44b}$$

Substituting the expansions into (4.6a) and (4.6b) and matching terms with different powers of k, we obtain the following:

- $O(1/k)$ in (4.6a):

$$\begin{aligned}
\frac{f_{11}(x)}{k} &= -\int_x^\infty e^{-2ik(x-y)} q_0(y) \left(1 + \frac{f_{21}(x)}{k} + O\left(\frac{1}{k^2}\right)\right) dy \\
&= -\int_x^\infty e^{-2ik(x-y)} q_0(y) dy + O\left(\frac{1}{k^2}\right) \\
&= \frac{q_0(x)}{2ik} + \frac{1}{2ik}\int_x^\infty e^{-2ik(x-y)} q_0'(y) dy + O\left(\frac{1}{k^2}\right), \\
\Rightarrow f_{11}(x) &= \frac{q_0(x)}{2i}.
\end{aligned}$$

- $O(1/k)$ in (4.6b):

$$\begin{aligned}
\frac{f_{21}(x)}{k} &= -\lambda \int_x^\infty \bar{q}_0(y)\phi_1(y,k) dy + O\left(\frac{1}{k^2}\right) = -\frac{\lambda}{2ik}\int_x^\infty |q_0(y)|^2 dy + O\left(\frac{1}{k^2}\right), \\
\Rightarrow f_{21}(x) &= -\frac{\lambda}{2i}\int_x^\infty |q_0(y)|^2 dy.
\end{aligned}$$

- $O(1/k^2)$ in (4.6a):

$$\begin{aligned}
\frac{f_{12}(x)}{k^2} &= \frac{1}{2ik}\int_x^\infty e^{-2ik(x-y)}q_0'(y)dy - \int_x^\infty e^{-2ik(x-y)}q_0(y)\left(-\frac{\lambda}{2ik}\int_y^\infty |q_0(z)|^2\,dz\right)dy \\
&\quad + O\left(\frac{1}{k^3}\right) \\
&= -\frac{q_0'(x)}{(2ik)^2} - \frac{\lambda q_0(x)\int_x^\infty |q_0(z)|^2\,dz}{(2ik)^2} \\
&\quad + \frac{\lambda}{(2ik)^2}\int_x^\infty e^{-2ik(x-y)}\left(q_0(y)\,|q_0(y)|^2 - q_0'(y)\int_y^\infty |q_0(z)|^2\,dz\right)dy + O\left(\frac{1}{k^3}\right) \\
&= -\frac{q_0'(x)}{(2ik)^2} - \frac{\lambda q_0(x)\int_x^\infty |q_0(y)|^2\,dy}{(2ik)^2} + O\left(\frac{1}{k^3}\right), \\
\Rightarrow f_{12}(x) &= -\frac{q_0'(x)}{(2i)^2} - \frac{\lambda q_0(x)\int_x^\infty |q_0(y)|^2\,dy}{(2i)^2}.
\end{aligned}$$

As a result, we obtain expansions for $a(k), b(k)$:

$$\begin{aligned}
a(k) &= \phi_2(0,k) = 1 - \frac{\lambda}{2ik}\int_0^\infty |q_0(y)|^2\,dy + O\left(\frac{1}{k^2}\right), \\
b(k) &= \phi_1(0,k) = \frac{q_0(0)}{2ik} - \frac{q_0'(0) + \lambda q_0(0)\int_0^\infty |q_0(y)|^2\,dy}{(2ik)^2} + O\left(\frac{1}{k^3}\right).
\end{aligned}$$

4.4.2 Large k asymptotics of $A(k,T), B(k,T)$

For $T < \infty$, the spectral functions $\overline{A(\bar{k},T)} = \Phi_2(T,k)$ and $-e^{-4ik^2T}B(k,T) = \Phi_1(T,k)$ are defined using the linear Volterra integral equations (4.7a) and (4.7b). We use the following expansions for large $k \in \mathbb{C}$,

$$\Phi_1(t,k) = \frac{h_{11}(t)}{k} + \frac{\hat{h}_{11}(t)e^{-4ik^2t}}{k} + \frac{h_{12}(t)}{k^2} + \frac{\hat{h}_{12}(t)e^{-4ik^2t}}{k^2} + O\left(\frac{1}{k^3}\right) + O\left(\frac{e^{-4ik^2t}}{k^3}\right), \tag{4.45a}$$

$$\Phi_2(t,k) = 1 + \frac{h_{21}(t)}{k} + \frac{\hat{h}_{22}(t)e^{-4ik^2t}}{k^2} + \frac{\hat{h}_{23}(t)e^{-4ik^2t}}{k^3} + O\left(\frac{1}{k^2}\right) + O\left(\frac{e^{-4ik^2t}}{k^4}\right), \tag{4.45b}$$

where the terms depending on e^{-4ik^2t} are separated. Substituting the expansions into (4.7a) and (4.7b) and matching terms with different powers of k, we obtain the following:

- $O(1) + O(e^{-4ik^2t}/k^2)$ in (4.7b):

$$\begin{aligned}
1 + \frac{\hat{h}_{22}(t)e^{-4ik^2t}}{k^2} =& 1 + \int_0^t 2k\lambda\overline{g_0(\tau)}\left(\frac{h_{11}(\tau)}{k} + \frac{\hat{h}_{11}(\tau)e^{-4ik^2\tau}}{k}\right) + i\lambda\left|g_0(\tau)^2\right|d\tau \\
&+ O\left(\frac{1}{k}\right) + O\left(\frac{e^{-4ik^2t}}{k^3}\right), \\
\frac{\hat{h}_{22}(t)e^{-4ik^2t}}{k^2} =& \lambda\int_0^t 2\overline{g_0(\tau)}h_{11}(\tau) + i\left|g_0(\tau)^2\right|d\tau + \int_0^t 2\lambda\overline{g_0(\tau)}\hat{h}_{11}(\tau)e^{-4ik^2\tau}d\tau \\
&+ O\left(\frac{1}{k}\right) + O\left(\frac{e^{-4ik^2t}}{k^3}\right), \\
=& \lambda\int_0^t 2\overline{g_0(\tau)}h_{11}(\tau) + i\left|g_0(\tau)^2\right|d\tau \\
&+ \frac{2i\lambda}{4k^2}\left(\overline{g_0(t)}\hat{h}_{11}(t)e^{-4ik^2t} - \overline{g_0(0)}\hat{h}_{11}(0) - \int_0^t e^{-4ik^2\tau}d\left(\overline{g_0(\tau)}\hat{h}_{11}(\tau)\right)\right) \\
&+ O\left(\frac{1}{k}\right) + O\left(\frac{e^{-4ik^2t}}{k^3}\right).
\end{aligned}$$

From this

$$2\overline{g_0(\tau)}h_{11}(\tau) + i\left|g_0(\tau)^2\right| = 0 \quad \Rightarrow \quad h_{11}(t) = \frac{g_0(t)}{2i},$$

and

$$\hat{h}_{22}(t) = \frac{i\lambda}{2}\left(\overline{g_0(t)}\hat{h}_{11}(t)\right).$$

- $O(1/k) + O(e^{-4ik^2t}/k)$ in (4.7a):

$$\begin{aligned}
\frac{h_{11}(t)}{k} + \frac{\hat{h}_{11}(t)e^{-4ik^2t}}{k} =& \int_0^t e^{-4ik^2(t-\tau)} \left(-i\lambda \left| g_0^2 \right| \left(\frac{h_{11}}{k} + \frac{\hat{h}_{11}e^{-4ik^2\tau}}{k} \right) \right) d\tau \\
&+ \int_0^t e^{-4ik^2(t-\tau)} \left(2kg_0 + ig_1 \right) \left(1 + \frac{h_{21}}{k} + \frac{\hat{h}_{22}e^{-4ik^2\tau}}{k^2} \right) d\tau \\
&+ O\left(\frac{1}{k^2} \right) + O\left(\frac{e^{-4ik^2t}}{k^2} \right), \\
\frac{h_{11}(t)}{k} + \frac{\hat{h}_{11}(t)e^{-4ik^2t}}{k} =& e^{-4ik^2t} \int_0^t -i\lambda \left| g_0^2 \right| \frac{\hat{h}_{11}(t)}{k} d\tau \\
&+ \int_0^t e^{-4ik^2(t-\tau)} \left(2kg_0 \left(1 + \frac{\hat{h}_{22}e^{-4ik^2\tau}}{k^2} \right) \right) d\tau \\
&+ O\left(\frac{1}{k^2} \right) + O\left(\frac{e^{-4ik^2t}}{k^2} \right), \\
\frac{h_{11}(t)}{k} + \frac{\hat{h}_{11}(t)e^{-4ik^2t}}{k} =& \frac{g_0(t) - g_0(0)e^{-4ik^2t}}{2ik} \\
&+ e^{-4ik^2t} \int_0^t \left(-i\lambda \left| g_0^2 \right| \frac{\hat{h}_{11}(t)}{k} + 2g_0 \frac{\hat{h}_{22}}{k} \right) d\tau \\
&+ O\left(\frac{1}{k^2} \right) + O\left(\frac{e^{-4ik^2t}}{k^2} \right), \\
\frac{h_{11}(t)}{k} + \frac{\hat{h}_{11}(t)e^{-4ik^2t}}{k} =& \frac{g_0(t)}{2ik} + \frac{ig_0(0)e^{-4ik^2t}}{2k} + O\left(\frac{1}{k^2} \right) + O\left(\frac{e^{-4ik^2t}}{k^2} \right).
\end{aligned}$$

It follows that for $\Phi_1(t,k)$,

$$\begin{aligned}
h_{11}(t) &= \frac{g_0(t)}{2i}, \\
\hat{h}_{11}(t) &= \frac{ig_0(0)}{2}, \\
h_{12}(t) &= \frac{g_1(t)}{4} - \frac{i\lambda g_0(t)}{4} \int_0^t \overline{g_0(\tau)} g_1(\tau) - \overline{g_1(\tau)} g_0(\tau) d\tau, \\
\hat{h}_{12}(t) &= -\frac{g_1(0)}{4} - \frac{i\lambda g_0(0)}{4} \int_0^t \overline{g_0(\tau)} g_1(\tau) - \overline{g_1(\tau)} g_0(\tau) d\tau,
\end{aligned}$$

and for $\Phi_2(t,k)$,

$$
\begin{aligned}
h_{21}(t) &= \frac{\lambda}{2}\int_0^t \overline{g_0(\tau)}g_1(\tau) - \overline{g_1(\tau)}g_0(\tau)d\tau,\\
\hat{h}_{22}(t) &= \frac{\lambda\overline{g_0(t)}g_0(0)}{4i},\\
\hat{h}_{23}(t) &= \frac{i\lambda}{8}\left(\overline{g_1(t)}g_0(0) - \overline{g_0(t)}g_1(0) - i\lambda g_0(0)\overline{g_0(t)}\int_0^t \overline{g_0(\tau)}g_1(\tau) - \overline{g_1(\tau)}g_0(\tau)d\tau\right).
\end{aligned}
$$

As a result, we have

$$
\begin{aligned}
A(k,T) =& \overline{\Phi_2(T,\overline{k})}\\
=& 1 - \frac{\lambda}{2k}\int_0^T G(t)dt + \frac{i\lambda e^{4ik^2T}}{4k^2}\overline{g_0(0)}g_0(T)\\
&+ \frac{-\frac{i\lambda}{8}\left(G(T) - i\lambda g_0(T)\overline{g_0(0)}\int_0^T G(\tau)d\tau\right)e^{4ik^2T}}{k^3}\\
&+ O\left(\frac{1}{k^3}\right) + O\left(\frac{e^{-4ik^2t}}{k^4}\right),\\
B(k,T) =& -e^{4ik^2T}\Phi_1(T,k)\\
=& -\frac{g_0(T)e^{4ik^2T}}{2ik} - \frac{ig_0(0)}{2k} - \frac{\left(g_1(T) - i\lambda g_0(T)\int_0^T G(\tau)d\tau\right)e^{4ik^2T}}{4k^2}\\
&+ \frac{g_1(0) + i\lambda g_0(0)\int_0^T G(\tau)d\tau}{4k^2}\\
&+ O\left(\frac{1}{k^3}\right) + O\left(\frac{e^{-4ik^2t}}{k^3}\right),
\end{aligned}
$$

where

$$G(t) = \overline{g_0(t)}g_1(t) - \overline{g_1(t)}g_0(t).$$

4.4.3 Large k asymptotics of $A(k,\infty), B(k,\infty)$

We use the alternative set of equations for $A(k,\infty) = \tilde{\Phi}_2(0,k)$ and $B(k,\infty) = \tilde{\Phi}_1(0,k)$, which are defined using the linear Volterra integral equations (4.8a) and (4.8b). Following similar

steps to the calculations for $a(k)$ and $b(k)$, we have the expansions for $A(k,\infty), B(k,\infty)$,

$$A(k,\infty) = \tilde{\Phi}_2(0,k) = 1 - \frac{\lambda}{2k}\int_0^\infty G(t)dt + O\left(\frac{1}{k^2}\right),$$
$$B(k,\infty) = \tilde{\Phi}_1(0,k) = \frac{g_0(0)}{2ik} + \frac{g_1(0) + i\lambda g_0(0)\int_0^\infty G(\tau)d\tau}{4k^2} + O\left(\frac{1}{k^3}\right),$$

where

$$G(t) = \overline{g_0(t)}g_1(t) - \overline{g_1(t)}g_0(t).$$

These expansions are consistent with $A(k,T), B(k,T)$ by taking $T \to \infty$ after dropping all terms containing e^{4ik^2T}. For $T = \infty$, the expansions are only valid in $\mathrm{Re}\,(ik^2) \le 0$.

4.4.4 Compatibility conditions and the expansions for the global relation

If we expand the global relation at $k = \infty$, the compatibility conditions of the NLS equation at $x = 0, t = 0$ are obtained. In the case $T = \infty$, we get

$$\begin{aligned}
\text{the global relation} \qquad & a(k)B(k,\infty) - b(k)A(k,\infty) = 0, \\
O(1/k) \qquad & \frac{g_0(0)}{2ik} - \frac{q_0(0)}{2ik} = 0, \\
O(1/k^2) \qquad & \frac{g_1(0)}{4k^2} - \frac{q_0'(0)}{4k^2} = 0.
\end{aligned}$$

Though the expansions for a, b, A, B depend both on $q_0(0), g_0(0), g_1(0)$ and on the integrals of q_0, g_0, g_1, it turns out that the latter cancel in the expansion of the global relation. Furthermore, if $a, A \neq 0$, the global relation is rearranged as $b/a = B/A$

$$B/A \approx \frac{g_0(0)}{2ik} + \frac{g_1(0)}{4k^2} + O\left(\frac{1}{k^3}\right), \quad b/a \approx \frac{q_0(0)}{2ik} + \frac{q_0'(0)}{4k^2} + O\left(\frac{1}{k^3}\right).$$

The integral of q_0, g_0 and g_1 do not appear in the expansions of B/A and b/a as well. For the UTM, the global relation is strictly satisfied throughout the calculation, but the solution does not require infinitely many compatibility conditions at the corner $x = t = 0$. When the compatibility condition is violated at certain order of $1/k^n$, the coefficients of the next order term is infinite to balance the it. This can be shown by an explicit example in the linear case.

Example 3. *Using the UTM, the solution formula for the LS equation,*

$$iq_t + q_{xx} = 0,$$

on the half-line with the initial condition $q_0(x) = e^{-x}$ *and the homogeneous Dirichlet boundary condition* $g_0(t) = 0$ *is*

$$q(x,t) = \frac{1}{2\pi}\int_{-\infty}^{\infty} \frac{e^{ikx-ik^2t}}{1+ik}dk - \frac{1}{2\pi}\int_{\partial D^+} \frac{e^{ikx-ik^2t}}{1-ik}dk,$$

where ∂D^+ *is the boundary of the first quadrant, positively oriented. The Neumann data is then computed by,*

$$g_1(t) = q_x(0,t) = \frac{1-i}{\sqrt{2\pi t}} - \frac{1}{\pi}\int_{-\infty}^{\infty} \frac{e^{-ik^2t}}{1+k^2}dk.$$

with asymptotics

$$q_x(0,t) \approx O(t^{-1/2}) \quad \text{as } t \to 0,$$
$$q_x(0,t) \approx O(t^{-3/2}) \quad \text{as } t \to \infty.$$

Therefore, $g_1(t) = q_x(0,t)$ *is unbounded near* $t = 0$*. On the other hand, the global relation for* $T = \infty$ *is*

$$\hat{q}_0(k) = i\tilde{g}_1(k), \quad Re\,(k) \le 0, Im\,(k) \le 0,$$

with

$$\hat{q}_0(k) = \int_0^{\infty} e^{-ikx}e^{-x}dx = \frac{1}{1+ik},$$
$$i\tilde{g}_1(k) = i\int_0^{\infty} e^{ik^2t}q_x(0,t)dt = i\int_0^{\infty} \frac{e^{ik^2t}}{\pi}\int_{-\infty}^{\infty} e^{-is^2t}\frac{s^2}{1+s^2}dsdt = \frac{1}{1+ik}.$$

The global relation is indeed still satisfied and the leading order expansion of $B(k,\infty) = i\tilde{g}_1(k) + k\tilde{g}_0(k)$ *is given by*

$$B(k,\infty) = \frac{\sqrt{2\pi}\left(q_x(0,t)\sqrt{t}\right)|_{t=0}}{(i-1)k} + O(1/k^2).$$

On the other hand, if $\lim_{t\to 0}\partial_x^n q(0,t)$ *is known to be bounded, then the global relation implies that the initial and boundary values are compatible with respect to the LS equation up to the* n*-th order derivative.*

4.4.5 Using large k expansions for computing $q(x,t)$ for small x,t

For problems on the whole line, if the initial condition is in Schwartz class, the reflection coefficients is also in Schwartz class [10]. Therefore no modification for the associated RHP is required when x,t are small since the jump matrix there decays rapidly to the identity matrix when $|k|$ becomes large. However, this is not true for the RHP (4.19) from problems on the half-line or even for integrals that arise in the linear case.

Example 4. *Consider the NLS equation with the homogeneous Neumann boundary condition $g_1(t) = 0$ and initial condition $q_0(x) = e^{-x^2} + isech^2(x)$. This is a linearizable boundary condition so that we can solve for the spectral functions $B(k,\infty)$, $A(k,\infty)$ using symmetries of the global relation $k \to -k$. The associated RHP (4.47) for $\Phi(x,t,k)$ is formulated with the jump condition on the cross $k \in \mathbb{R} \cup i\mathbb{R}$ in Figure 4.1,*

$$\Phi_+(k;x,t) = \Phi_-(k;x,t)J(k;x,t). \tag{4.46}$$

The jump matrices are the same as in (4.20) except that (4.21c) is replaced by

$$\Gamma(k) = \frac{\lambda\overline{b(-\overline{k})}}{a(k)\Delta_1(k)}, \ \ arg\ k \in [0,\pi],$$

where

$$\Delta_1(k) = a(k)\overline{a(-\overline{k})} - \lambda b(k)\overline{b(-\overline{k})}, \ \ arg\ k \in [0,\pi].$$

The functions $\gamma(k)$ and $\Gamma(k)$ in are $O(1/k)$ as $k \to \infty$ as shown in Figure 4.10.

With the large k expansions, we can use them to set up RHPs with jump matrices that tend to the identity matrix faster. Using the results from the previous sections, we define

$$\gamma_0(k) = \frac{q_0(0)}{2i\left(k-\hat{k}\right)}, \quad \Gamma_0(k) = \frac{\lambda\overline{q_0(0)}}{2i\left(k-\hat{k}\right)},$$

and

$$\gamma(k) = \gamma_0(k) + \gamma_r(k), \quad \Gamma(k) = \Gamma_0(k) + \Gamma_r(k),$$

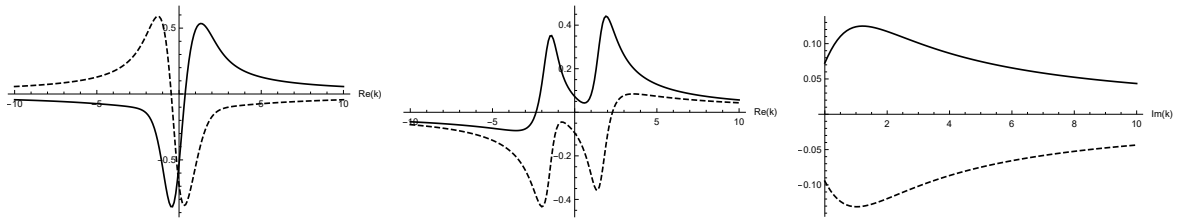

Figure 4.10: The plots of $\gamma(k), \Gamma(k)$ along the jump contour. Left: $\gamma(k)$ on the real axis. Middle: $\Gamma(k)$ on the real axis. Right: $\Gamma(k)$ on the positive imaginary axis. The real parts are plotted with solid curves and the imaginary parts are plotted with dashed curves. The initial condition is $q_0(x) = e^{-x^2} + i\ \mathrm{sech}^2(x)$ and the boundary condition is $g_1(t) = 0$.

so that $\gamma_0(k)$ and $\Gamma_0(k)$ have the same large k behavior as $\gamma(k)$ and $\Gamma(k)$ to the leading order. To avoid introducing unnecessary residue conditions, we choose $\hat{k} = 1 - 2i$. After separating the $O(1/k)$ terms, we get a RHP which has the jump matrix approaches the identity matrix with $O(1/k^2)$ as $k \to \infty$ and the contour is shown in Figure 4.11. The RHP for $\Phi(x, t, k)$ is formulated with a jump condition on the eight rays starting from the origin $\{r = \rho e^{is} | \rho \in [0, +\infty),\ s = 0, \pi/4, 2\pi/4, 3\pi/4, 4\pi/4, 5\pi/4, 6\pi/4, 7\pi/4\}$. The contour is shown in Figure 4.11 and $\Phi(x, t, k)$ satisfies

$$\Phi_+(k; x, t) = \Phi_-(k; x, t) V(k; x, t), \tag{4.47}$$

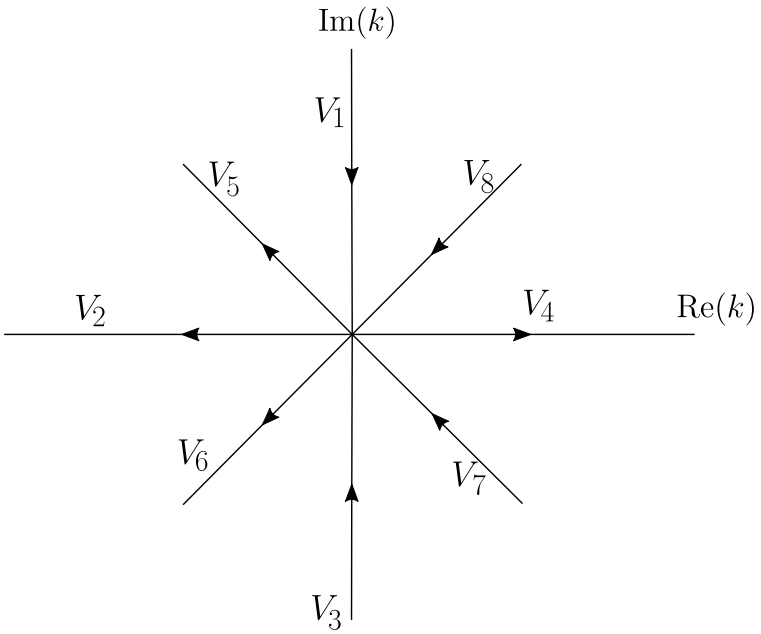

Figure 4.11: The contour of RHP (4.47). The jumps on V_5, V_6, V_7, V_8 are introduced to improve the rate at which the jump matrices on V_1, V_2, V_3, V_4 approach the identity matrix.

with jump matrices

$$V(k;x,t) = \begin{cases} V_4(k;x,t), & \arg\, k = 0, \\ V_1(k;x,t), & \arg\, k = \frac{\pi}{2}, \\ V_2(k;x,t), & \arg\, k = \pi, \\ V_3(k;x,t), & \arg\, k = \frac{3\pi}{2}, \\ V_5(k;x,t), & \arg\, k = \frac{3\pi}{4}, \\ V_6(k;x,t), & \arg\, k = \frac{5\pi}{4}, \\ V_7(k;x,t), & \arg\, k = \frac{7\pi}{4}, \\ V_8(k;x,t), & \arg\, k = \frac{\pi}{4}, \end{cases} \tag{4.48}$$

where

$$V_1(k;x,t)=\begin{bmatrix}1 & 0\\ -\Gamma_r(k)e^{2i\theta(k;x,t)} & 1\end{bmatrix},\quad V_3(k;x,t)=\begin{bmatrix}1 & -\lambda\overline{\Gamma_r(\bar{k})}e^{-2i\theta(k;x,t)}\\ 0 & 1\end{bmatrix},$$

$$V_4(k;x,t)=\begin{bmatrix}1+\lambda\overline{\gamma_r(\bar{k})}\gamma_r(k) & \gamma_r(k)e^{-2i\theta(k;x,t)}\\ \lambda\overline{\gamma_r(\bar{k})}e^{2i\theta(k;x,t)} & 1\end{bmatrix},$$

$$V_2(k;x,t)=\begin{bmatrix}1 & -\left(\lambda\overline{\Gamma_r(\bar{k})}+\gamma_r(k)\right)e^{-2i\theta(k;x,t)}\\ -\left(\lambda\overline{\gamma_r(\bar{k})}+\Gamma_r(k)\right)e^{2i\theta(k;x,t)} & 1+\left(\lambda\overline{\Gamma_r(\bar{k})}+\gamma_r(k)\right)\left(\lambda\overline{\gamma_r(\bar{k})}+\Gamma_r(k)\right)\end{bmatrix},$$

$$V_5(k;x,t)=\begin{bmatrix}1 & -\left(\lambda\overline{\gamma_0(\bar{k})}+\Gamma_0(k)\right)e^{-2i\theta(k;x,t)}\\ 0 & 1\end{bmatrix},$$

$$V_6(k;x,t)=\begin{bmatrix}1 & 0\\ -\left(\lambda\overline{\Gamma_0(\bar{k})}+\gamma_0(k)\right)e^{2i\theta(k;x,t)} & 1\end{bmatrix},$$

$$V_7(k;x,t)=\begin{bmatrix}1 & -\left(\lambda\overline{\Gamma_0(\bar{k})}+\gamma_0(k)\right)e^{-2i\theta(k;x,t)}\\ 0 & 1\end{bmatrix},$$

$$V_8(k;x,t)=\begin{bmatrix}1 & 0\\ -\left(\Gamma_0(k)+\lambda\overline{\gamma_0(\bar{k})}\right)e^{2i\theta(k;x,t)} & 1\end{bmatrix}.$$

Figure (4.12) shows the log-linear plot of the absolute error computed for computing $q(0.5,0)$ with different numbers of collocation points N. The dashed line is computed with the undeformed RHP (4.19) and the solid line is computed with the RHP (4.47). In the computation, the segments of contours are truncated when the jump matrix is close to the identity matrix $\|V_m(k)-I\|_2<10^{-8}$, $m=1,2,..,8.$ or when the contour reaches a large circle centered at the origin with radius 50. In Figure (4.12), the dashed curve is the error computed using the undeformed contour and the solid curve is the error computed using the contour in Figure 4.11. Both curves decay exponentially when N is not too large. Since the jump matrix of RHP (4.47) has faster decay, the flattening in the solid curve appears later than the dashed curve. It is possible to perform the asymptotic analysis for higher order terms in the previous section and remove more terms so that the decay of the jump matrix

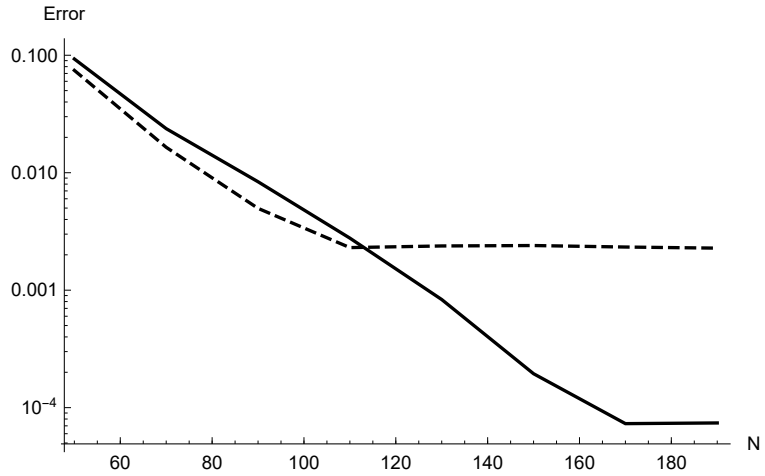

Figure 4.12: The absolute error for computing $q(0.5, 0)$ with different number of collocation points N. The dashed line is computed using the undeformed contour in Figure 4.1. The solid line is computed using the contour in Figure 4.11. The flattening in both curves is due to the truncation error.

is faster than $O(1/k^2)$, though the calculation starts to become tedious quickly.

Remark 14. *For linearizable boundary conditions that can be mapped to a smooth solution of the whole-line problem, the original jump matrix J_2 in (4.19) actually decays exponentially to the identity matrix. Therefore there is no need to introduce modifications to V_2, V_5 and V_6 in (4.47). In this case, $\Gamma(k)$ is automatically analytically extended to the first quadrant by the analyticity of $b(k)$ and $a(k)$. Then it is possible to deform the jump contour J_1 and J_3 in (4.19) to the positive real line on top of J_4 and this new RHP is the same as the RHP in the whole-line problem with the initial values on the negative real line defined properly corresponding to the boundary condition using symmetry.*

Chapter 5
CONCLUSION AND FUTURE WORK

In this dissertation, I have introduced a hybrid analytical-numerical method, the NUTM for integrable IBVPs, as a generalization of the NIST.

- In Chapter 2, the NIST is applied to the SG equation on the whole line.
- In Chapter 3, the NUTM is applied to half-line problems for the heat equation, the LS equation and a third-order linear PDE.
- In Chapter 4, the NUTM is applied to half-line problems for the NLS equation.

For all linearizable cases and some special nonlinearizable cases, we have demonstrated the following features of the NUTM.

1. The method gives the solution at a given (x, t) **without time-stepping or spatial discretization**. This is achieved by using the integrability of the equation.
2. The method is **spectrally accurate** by using spectral methods in each of the step.
3. The method is **uniformly accurate** by using the method of (nonlinear) steepest descent.
4. The method only requires some decay and regularity assumptions on the initial and boundary data. No closed-form expressions for the scattering data are required.
5. The method does not artificially truncate the infinite physical domain.
6. The computations require only the numerical solution of linear problems.

There are many directions for future research including:

1. **Numerical methods for highly oscillatory integrals.** In Chapter 3, we have shown that for dispersive problems, the deformation of the contour is often restricted inside the region where the spectral functions are analytic. As a result, the oscillation is not completely converted into exponential decay. As this is the crux of the problem, any improvement on the computation of the oscillatory integral would improve the overall efficiency dramatically. A counterpart of this in the nonlinear cases is numerical methods for highly oscillatory SIEs from the RHPs. The decay assumptions on the initial and boundary functions can also be relaxed if there is no large deformation.

2. **Analytical and numerical methods for solving the nonlinear Volterra integral equations.** If the nonlinear Volterra integral equation from (4.17) can be solved efficiently, then the full set of spectral functions can be computed allowing us to solve the IBVPs with generic data. However, this is not sufficient to compute the inverse problem efficiently. In the example of the NLS equation on the half-line, in general the Dirichlet data and the Neumann data cannot have exponential decay at the same time. The numerical methods for highly oscillatory SIEs are still required.

3. **Generalization and application to other integrable problems.** Applying the NUTM to other integrable systems is nontrivial. Like the NIST for the SG equation, there are likely to be many details one need to work. Some integrable systems require the so-called DBAR formulation as a generalization of the RHP [1, 2]. One can apply the NUTM to problems with different boundary conditions: finite interval problems, periodic boundary conditions. For linear PDEs, we have only considered constant coefficients, one can also apply the NUTM to linear PDEs with variable coefficients. There is a lot of research on solving linear elliptic equations using the UTM that is not considered here [62].

BIBLIOGRAPHY

[1] M. J. Ablowitz and P. A. Clarkson. *Solitons, nonlinear evolution equations and inverse scattering*. Cambridge University Press, Cambridge, 1991.

[2] M. J. Ablowitz and A. S. Fokas. *Complex variables: introduction and applications*. Cambridge University Press, 2003.

[3] M. J. Ablowitz, B. M. Herbst, and C. Schober. On the numerical solution of the sine-Gordon equation: I. integrable discretizations and homoclinic manifolds. *Journal of Computational Physics*, 126:299–314, 1996.

[4] M. J. Ablowitz, B. M. Herbst, and C. Schober. On the numerical solution of the sine-gordon equation: II. performance of numerical schemes. *Journal of Computational Physics*, 131:354–367, 1997.

[5] M. J. Ablowitz, D. J. Kaup, A. C. Newell, and H. Segur. Method for solving the sine-Gordon equation. *Physical Review Letters*, 30:1262–1264, 1973.

[6] M. J. Ablowitz, D.J. Kaup, A.C. Newell, and H. Segur. The inverse scattering transform-fourier analysis for nonlinear problems. *Studies in Applied Mathematics*, 53(4):249–315, 1974.

[7] M.E. Alexander and J.L.L. Morris. Galerkin methods for some model equations for nonlinear dispersive waves. *Journal of Computational Physics*, 30:428–451, 1979.

[8] A. Barone, F. Esposito, C. J. Magee, and A. C. Scott. Theory and applications of the sine-Gordon equation. *La Rivista del Nuovo Cimento*, 1:227–267, 1971.

[9] Z. Battles and L. N. Trefethen. An extension of MATLAB to continouous functions and operators. *SIAM Jounal of Scientific Computing*, 25:1743–1770, 2004.

[10] R. Beals and R. Coifman. Scattering and inverse scattering for first order systems. *Communications in Pure and Applied Mathematics*, 37:39–90, 1984.

[11] D. Bilman and T. Trogdon. Benchmarking numerical methods for lattice equations with the toda lattice. *arXiv:1709.06659 [math.AP]*.

[12] D. Bilman and T. Trogdon. Numerical inverse scattering for the toda lattice. *Communications in Mathematical Physics*, 352:805–879, 2017.

[13] G. Biondini and A. Bui. On the nonlinear Schrodinger equation on the half line with homogeneous Robin boundary conditions. *Studies in Applied Mathematics*, 129:249–271, 2012.

[14] G. Boffetta and A.R. Osborne. Computation of the direct scattering transform for the nonlinear Schrodinger equation. *Journal of Computational Physics*, 102:252–264, 1992.

[15] T. Bothner. On the origins of Riemann-Hilbert problems in mathematics. *Nonlinearity*, 34, 2021.

[16] C. Bu. Forced cubic Schrodinger equation with Robin boundary data: continuous dependency result. *Journal of the Australian Mathematical Society Series B*, 41:301–311, 2000.

[17] R. Buckingham and P. D. Miller. Exact solutions of semiclassical non-characteristic Cauchy problems for the sine-Gordon equation. *Physica D.*, 237:2296–2341, 2008.

[18] R. Carroll and C. Bu. Solution of the forced NLS equation using PDE techniques. *Applicable Analysis*, 41:33–51, 1991.

[19] P. Cheng, S. Venakides, and X. Zhou. Long-time asymptotics for the pure radiation solution of the sine-Gordon equation. *Communications in Partial Differential Equations*, 24:1195–1262, 1999.

[20] F. P. J. de Barros, M. J. Colbrook, and A. S. Fokas. A hybrid analytical-numerical method for solving advection-dispersion problems on a half-line. *International Journal of Heat and Mass Transfer*, 139:482–491, 2019.

[21] B. Deconinck. *Lecture notes on nonlinear waves.*

[22] B. Deconinck and J. N. Kutz. Computing spectra of linear operators using the Floquet-Fourier-Hill mehod. *Jounal of Computational Physics*, 291:296–321, 2006.

[23] B. Deconinck, T. Trogdon, and V. Vasan. The method of Fokas for solving linear partial differential equations. *SIAM Review*, 56(1):159–186, 2014.

[24] B. Deconinck, T. Trogdon, and X. Yang. The numerical unified transform method for the nonlinear Schrodinger equation on the half-line. *in preparation.*

[25] B. Deconinck, T. Trogdon, and X. Yang. Numerical inverse scattering for the sine-Gordon equation. *Physica D.*, 399:159–172, 2019.

[26] B. Deconinck, T. Trogdon, and X. Yang. The numerical unified transform method for initial-boundary value problems on the half-line. *IMA Journal of Numerical Analysis*, 2020.

[27] P. Deift and X. Zhou. A steepest descent method for oscillatory Riemann-Hilbert problems. asymptotics for the mKdV equation. *Annals of Mathematics*, 137:295–368, 1993.

[28] F. Diacu. The solution of the n-body problem. *The Mathematical Intelligencer*, 18(3):66–70, 1996.

[29] R. K. Dodd and R. K. Bullough. Backlund transformations for the sine-Gordon equations. *Proceedings of the Royal Society of London A*, 351:499–523, 1976.

[30] N. Flyer and A. S. Fokas. A hybrid analytical-numerical method for solving evolution partial diffrerential equations. i. the half-line. *Proceedings of the Royal Society A*, 464:1823–1849, 2008.

[31] A. S. Fokas. A unified transform method for solving linear and certain nonlinear PDEs. *Proceedings of the Royal Society of London A*, 453:1411–1443, 1997.

[32] A. S. Fokas. Integrable nonlinear evolution equations on the half-line. *Communications in Mathematical Physics*, 230:1–39, 2002.

[33] A. S. Fokas. A new transform method for evolution partial differential equations. *IMA Journal of Applied Mathematics*, 67:559–590, 2002.

[34] A. S. Fokas. The nonlinear Schrodinger equation on the half-line. *Nonlinearity*, 18:1771–1882, 2005.

[35] A. S. Fokas. *A Unified Approach to Boundary Value Problems.* SIAM, Philadelphia, PA, 2008.

[36] A. S. Fokas, N. Flyer, S. A. Smitheman, and E.A. Spence. A semi-analytical numerical method for solving evolution and elliptic partial differential equations. *Journal of Computational and Applied Mathematics*, 227:59–74, 2009.

[37] A. S. Fokas and A. R. Its. The linearization of the initial-boundary value problem of the nonlinear Schrodinger equation. *SIAM Journal of Mathematical Analysis*, 27:738–764, 1996.

[38] A. S. Fokas and S. Kamvissis. Zero dispersion limit for integrable equations on the half-line with linearizable data. *Abstract and Applied Analysis*, 5:361–370, 2004.

[39] A. S. Fokas and J. Lenells. The unified method: I. nonlinearizable problems on the half-line. *Journal of Physical A: Mathematical and Theoretical*, 45:195201, 2012.

[40] A. S. Fokas and E. A. Spence. Synthesis, as opposed to separation, of variables. *SIAM Review*, 54(2):291–324, 2012.

[41] J. Frauendiener and C. Klein. Hyperelliptic theta-functions and spectral methods: KdV and KP solutions. *Letters in Mathematical Physics*, 76:249–267, 2006.

[42] A. Gibbs, D. Hewett, D. Huybrechs, and E. Parolin. Fast hybrid numerical-asymptotic boundary element methods for high frequency screen and aperture problems based on least-squares collocation. *SN Partial Differential Equations and Applications*, 1, 2020.

[43] T. Grava and C. Klein. Numerical solution of the small dispersion limit of Korteweg-de Vries and Whitham equations. *Communications on Pure and Applied Mathematics*, 60:1623–1664, 2007.

[44] B. Guo, P. J. Pascual, M. J. Rodriguez, and L. Vazques. Numerical solution of the sine-Gordon equation. *Applied Mathematics and computation*, 18:1–14, 1986.

[45] O. H. Hald. Numerical solution of the Gelfand-Levitan equation. *Linear Algebra and Its Applications*, 28:99–111, 1979.

[46] A. Himonas, D. Mantzavinos, and F. Yan. The nonlinear Schrodinger equation on the half-line with Neumann boundary conditions. *Applied Numerical Mathematics*, 141:2–18, 2019.

[47] L. Huang and J. Lenells. Construction of solutions and asymptotics for the sine-Gordon equation in the quarter plane. *Journal of Integrable Systems*, 3:1–92, 2018.

[48] D. Huybrechs and A. Gibbs. Pathfinder: a toolbox for oscillatory integrals by deforming into the complex plane. `https://github.com/AndrewGibbs/PathFinder`.

[49] A. Iserles, S. P. Norsett, and S. Olver. Highly oscillatory quadrature: The story so far. *Numerical Mathematics and Advanced Applications*, 2006.

[50] A. Its and D. Shepelsky. Initial boundary value problem for the focusing nonlinear Schrodinger equation with Robin boundary condition: half-line approach. *Proceedings of the Royal Society A*, 469:20120199, 2013.

[51] C. Jiang, J. Sun, H. Li, and Y. Wang. A fourth-order AVF method for the numerical integration of sine-Gordon equation. *Applied Mathematics and Computation*, 313:144–158, 2017.

[52] K. Kalimeris. Explicit soliton asymptotics for the nonlinear Schrodinger equation on the half-line. *Journal of Nonlinear Mathematical Physics*, 17:445–452, 2010.

[53] D. J. Kaup. Method for solving the sine-Gordon equation in laboratory coordinates. *Studies in Applied Mathematics*, 54:165–179, 1975.

[54] E. Kesici, B. Pelloni, T. Pryer, and D. Smith. A numerical implementation of the unified Fokas transform for evolution problems on a finite interval. *European Journal of Applied Mathematics*, 29(3):543–567, 2018.

[55] J. Lenells. Absense of solitons for the defocusing NLS equation on the half-line. *Letter of Mathematical Physics*, 106:1235–1241, 2016.

[56] J. Lenells and A. S. Fokas. The unified method: II NLS on the half-line with t-periodic boundary conditions. *Journal of Physical A: Mathematical and Theoretical*, 45:195202, 2012.

[57] P. D. Miller. *Applied asymptotic analysis*. AMS, Providence, RI, 2006.

[58] S. Olver. RHPackage. `http://www.maths.usyd.edu.au/u/olver/projects/RHPackage.html`, 2010.

[59] S. Olver. A general framework for solveing Riemann-Hilbert problems numerically. *Numerische Mathematik*, 122:305–340, 2012.

[60] S. Olver and T. Trogdon. Nonlinear steepest descent and the numerical solution of Riemann-Hilbert problems. *Communications on Pure and Applied Mathematics*, 67:1353–1389, 2014.

[61] T. S. Papatheodorou and A. N. Kandili. Novel numerical techniques based on Fokas transforms, for the solution of initial boundary value problems. *Journal of computational and applied mathematics*, 227:75–82, 2009.

[62] B. Pelloni. Advances in the study of boundary value problems for nonlinear integrable PDEs. *Nonlinearity*, 28(2):1–38, 2015.

[63] J. S. Russell. Report on waves. *In Report of the fourteenth meeting of the British Association for the Advancement of Science, York, September 1844*, pages 311–390, 2018.

[64] H. S. Shukla and M. Tamsir. Numerical solution of nonlinear sine-Gordon equation by using the modified cubic B-spline differential quadrature method. *Beni-Suef University Journal of Basic and Applied Sciences*, 7(4):359–366, 2018.

[65] T. R. Taha and M. J. Ablowitz. Analytical and numerical aspects of certain nonlinear evolution equations. II. numerical, nonlinear Schrodinger equation. *Journal of Computational Physics*, 55(2):203–230, 1984.

[66] F. Tisseur and K. Meerbergen. The quadratic eigenvalue problem. *SIAM Review*, 43:235–286, 2001.

[67] L. N. Trefethen. Is Gauss quadrature better than Clenshaw-Curtis? *SIAM Review*, 50:67–87, 2008.

[68] T. Trogdon. ISTPackage. `https://bitbucket.org/trogdon/istpackage`, 2013.

[69] T. Trogdon. On the application of GMRES to oscillatory singular integral equations. *BIT Numerical Mathematics*, 55:591–620, 2015.

[70] T. Trogdon. A unified numerical approach for the nonlinear Schrodinger equations. *In A.S. Fokas and B. Pelloni, editors, Unified Transform method for boundary value problems: applications and advances, Chapter 8, SIAM, Philadelphia, PA*, 2015.

[71] T. Trogdon and G. Biondini. Evolution partial differential equations with discontinuous data. *Quarterly of Applied Mathematics*, 77:689–726, 2019.

[72] T. Trogdon and S. Olver. Numerical inverse scattering for the focusing and defocusing nonlinear Schrodinger equations. *Proceedings of the Royal Society of London A*, 469, 2012.

[73] T. Trogdon and S. Olver. *Riemann-Hilbert problems, their numerical solution and the computation of nonlinear special functions*. SIAM, 2015.

[74] T. Trogdon, S. Olver, and B. Deconinck. Numerical inverse scattering for the Korteweg-de Vries and modified Korteweg-de Vries equations. *Physica D.*, 241(11):1003–1025, 2012.

[75] J. V. Uspensky. On the convergence of quadrature formulas related to an infinite interval. *Transactions of the American Mathematical Society*, 30:542–559, 1928.

[76] A. C. Vliengenhart. On finite difference methods for the Korteweg-de Vries equation. *Journal of Engineering Mathematics*, 5:137–155, 1971.

[77] J. Yang. *Nonlinear Waves in Integrable and Nonintegrable Systems*. SIAM, 2010.

[78] N. J. Zabusky and M. D. Kruskal. Interaction of solitons in a collisionless plasma and the recurrence of initial states. *Physical Review Letters*, 15(6):240–243, 1965.

[79] C. Zheng. Numerical solution to the sine-Gordon equation define on the whole real axis. *SIAM Jounal of Scientific Computing*, 29:2494–2506, 2007.

[80] X. Zhou. Inverse scattering transform for systems with rational dependence. *Jounal of Differential Equations*, 115:277–303, 1995.

Appendix A

THE PROOF OF UNIFORM CONVERGENCE OF THE NUMERICAL UNIFIED TRANSFORM METHOD APPLIED TO THE HEAT EQUATION

In this appendix, we prove the uniform convergence for Clenshaw-Curtis quadrature applied to the contour integrals for the heat equation in Section 3.3.2. We use the following result to estimate the error of Clenshaw-Curtis quadrature. The constant K for the integrals $I_1,\ I_2$ and B_0 is given in Theorem 4 and Theorem 5.

Theorem 3 (See [70], for example)**.** *Let $u(k;x,t)$ be so that for $m = 0,1,\ldots,M$, $\partial_k^m u(k;x,t)$ are absolutely continuous for fixed x,t and satisfy $\sup_{k\in[-1,1]}\left|\partial_k^{M+1}u(k;x,t)\right| \le K$ for all x,t. Define $i(u(\cdot;x,t)) = \int u(k;x,t)dk$ and $i_n(u(\cdot;x,t))$ to be the approximation of $i(u(\cdot;x,t))$ obtained with Clenshaw-Curtis quadrature. Then $i_n(u(\cdot;x,t))$ converges to $i(u(\cdot;x,t))$ uniformly in x,t. More precisely, there exists $N>0$ such that for $n>N$,*

$$\sup_{x,t}|i(u(\cdot;x,t)) - i_n(u(\cdot;x,t))| \le \frac{32K}{15M(2n+1-M)^M}.$$

In Theorem 4 and Theorem 5, we estimate the upper bound K for each part of the integral in (3.7). The uniform convergence is considered in the domain bounded away from the $t=0$ and $x=0$. For $c>0$, we define the region,

$$\Omega_c = \{(x,t):\ x\ge c,\ t\ge c\}.$$

Theorem 4 (Uniform convergence of I_1 and I_2 in (3.7) for the heat equation)**.** *For any $\delta,\epsilon,c>0$, assume $q_0\in C^\infty_\delta$ and let I_1^ϵ be the truncation of the integral* [1]

$$I_1 = \frac{1}{2\pi}\int_{\mathcal{C}_1^I} e^{ikx-\omega(k)t}\hat{q}_0(k)dk, \tag{A.1}$$

[1]The truncation depends on the prescribed tolerance ϵ. As $\hat{q}_0$ is bounded on the contour, we can use the exponential to get a good choice for the trunction. See the proof for how the truncation is done.

such that

$$\sup_{(x,t)\in\Omega_c} |I_1 - I_1^\epsilon| < C_1(q_0,\delta,c)\epsilon, \quad C_1(q_0,\delta,c) > 0.$$

Then Clenshaw-Curtis quadrature applied to I_1^ϵ *converges uniformly on* Ω_c. *Hence* $\mathcal{C}_1^I = \{a + ih : a \in \mathbb{R}\}$ *and* $h = \min(x/2t, \delta)$ *is as defined in Section 3.3.2. Similarly, with the same assumptions, let* I_2^ϵ *be the truncation of the integral*

$$I_2 = -\frac{1}{2\pi}\int_{\mathcal{C}_2^I} e^{ikx-k^2t}\hat{q}_0(-k)dk, \tag{A.2}$$

such that

$$\sup_{(x,t)\in\Omega_c} |I_2 - I_2^\epsilon| < C_2(q_0,\delta,c)\epsilon, \quad C_2(q_0,\delta,c) > 0.$$

Then Clenshaw-Curtis quadrature applied to I_2^ϵ *converges uniformly on* Ω_c. *Hence* $\mathcal{C}_2^I = \{a + ix/2t : a \in \mathbb{R}\}$.

Theorem 5 (Uniform convergence of B_0 in (3.7) for the heat equation)**.** *For any* $\gamma, \epsilon, c > 0$, *assume* $g_0 \in C_\gamma^\infty$ *and let* B_0^ϵ *be the truncation of the integral* [2]

$$B_0 = \frac{1}{\pi}\int_{\mathcal{C}_{0,a}^B} e^{ikx-k^2t}2ik\tilde{g}_0(k^2,t)dk + \frac{1}{2\pi}\int_{\mathcal{C}_{0,b}^B+\mathcal{C}_{0.c}^B} e^{ikx-k^2t}2ik\tilde{g}_0(k^2,t)dk, \tag{A.3}$$

such that

$$\sup_{(x,t)\in\Omega_c} |B_0 - B_0^\epsilon| < C(g_0,\gamma,c)\epsilon, \quad C(g_0,\gamma,c) > 0.$$

Then Clenshaw-Curtis quadrature applied to B_0^ϵ *converges uniformly on* Ω_c. *The contour is defined in Section 3.3.2 where* $\mathcal{C}_{0,a}^B = \{La + ix/2t : a \in [0,1], e^{-L^2t} = \epsilon\}$ *is the horizontal segment of the contour and* $\mathcal{C}_{0,b}^B = \{L + ix/2t + L_2e^{i\pi/4}a : a \in [0,\infty), e^{-L_2x} = \epsilon\}$, $\mathcal{C}_{0,c}^B = \{-L + ix/2t + L_2e^{-i\pi/4}a : a \in (-\infty,0], e^{-L_2x} = \epsilon\}$ *are the oblique segments of the contour with given tolerance* $\epsilon > 0$.

Proof of Theorem 4. For given tolerance $\epsilon > 0$, I_1 is truncated to I_1^ϵ of length $2L$ with $e^{-L^2t} = \epsilon$. We introduce the change of variables $k = La + ih$. The integral with $a > 1$ is cut

[2] As with Theorem 2, the truncation procedure is described in the proof.

off,

$$\begin{aligned}
I_1 =& \frac{Le^{-hx}}{2\pi}\int_{-\infty}^{\infty} e^{iLax-(La+ih)^2t}\hat{q}_0(La+ih)da \\
=& \frac{Le^{-hx}}{2\pi}\int_{-1}^{1} e^{iLax-(La+ih)^2t}\hat{q}_0(La+ih)da + \frac{Le^{-hx}}{2\pi}\int_{|a|>1} e^{iLax-(La+ih)^2t}\hat{q}_0(La+ih)da \\
=& I_1^{\epsilon} + \frac{Le^{-hx}}{2\pi}\int_{|a|>1} e^{iLax-(La+ih)^2t}\hat{q}_0(La+ih)da.
\end{aligned}$$

The second integral is dropped and the induced truncation error is bounded by

$$\begin{aligned}
\left|\frac{Le^{-hx}}{2\pi}\int_{|a|>1} e^{iLax-(La+ih)^2t}\hat{q}_0(La+ih)da\right| \leq& \frac{Le^{-hx}}{2\pi}\int_{|a|>1}\left|e^{iLax-(La+ih)^2t}\hat{q}_0(La+ih)\right|da \\
\leq& \frac{Le^{-hx}}{2\pi}\int_{|a|>1} e^{-L^2ta^2+h^2t}\left|\hat{q}_0(La+ih)\right|da \\
\leq& \|\hat{q}_0(\cdot+ih)\|_\infty \frac{Le^{-h(x-ht)}}{2\pi}\epsilon\int_{|a|>1} ae^{-L^2t(a^2-1)}da \\
\leq& \|\hat{q}_0(\cdot+ih)\|_\infty \frac{Le^{-h(x-ht)}}{2\pi}\epsilon\int_0^{\infty} e^{-L^2ts}ds \\
\leq& \|\hat{q}_0(\cdot+ih)\|_\infty \frac{Le^{-h^2t}}{2\pi}\frac{\epsilon}{(-\ln\epsilon)}.
\end{aligned}$$

Since t is bounded from below, L is bounded from above. The truncation error is therefore $\mathcal{O}(\epsilon)$, uniformly in $(x,t)\in\Omega_c$.

Uniform convergence to I_1^{ϵ} requires the derivative of the integrand in I_1^{ϵ} to satisfy

$$\sup_{a\in[-1,1]}\frac{Le^{-hx}}{2\pi}\left|\partial_a^2\left(e^{iLax-(La+ih)^2t}\hat{q}_0(La+ih)\right)\right| \leq M,$$

for all x,t. Notice that the derivatives of the exponential only introduce polynomial terms and $\hat{q}_0(k)$ is bounded and analytic in $\{k:\mathrm{Im}\,(k)\leq\delta\}$ which implies that $\partial_k\hat{q}_0(k)$ and $\partial_k^2\hat{q}_0(k)$ are bounded on the contour. It suffices to show

$$\begin{aligned}
\sup_{a\in[-1,1]}\left|\partial_a^2\left(\frac{Le^{-hx}}{2\pi}\cdot e^{iLax-(La+ih)^2t}\hat{q}_0(La+ih)\right)\right| \leq& \sup_{a\in[-1,1]}\left|\frac{Le^{-hx}}{2\pi}\cdot e^{iLax-(La+ih)^2t}P(a,Lx,L^2t,Lht)\right| \\
=& \sup_{a\in[-1,1]}\frac{Le^{-hx}}{2\pi}\cdot e^{-L^2ta^2+h^2t}\left|P(a,Lx,L^2t,Lht)\right|,
\end{aligned}$$

where P is a polynomial with positive coefficients.

When $h = x/2t \le \delta$,

$$\sup_{a\in[-1,1]} \frac{Le^{-hx}}{2\pi} \cdot e^{-L^2ta^2+h^2t} \left|P(a, Lx, L^2t, Lht)\right| = \sup_{a\in[-1,1]} \frac{Le^{-x^2/4t-L^2ta^2}}{2\pi} \left|P(a, Lx, L^2t, Lx/2)\right|$$
$$\le \frac{e^{-x^2/4t}}{2\pi} Q(x^2/4t) \le M_1 < \infty,$$

where Q is a polynomial with positive coefficients and we have used that L^2t is constant.

When $h = \delta < x/2t$,

$$\sup_{a\in[-1,1]} \frac{Le^{-hx}}{2\pi} \cdot e^{-L^2ta^2+h^2t} \left|P(a, Lx, L^2t, Lht)\right| \le \sup_{a\in[-1,1]} e^{-\delta x/2-L^2ta^2} \left|P(a, Lx, L^2t, Lx/2)\right|$$
$$\le \sup_{a\in[-1,1]} e^{-\delta x/2} Q_2(x) \le M_2 < \infty,$$

where Q_2 is a polynomial with positive coeffcients. As a result, the second derivative of the integrand of (A.1) is uniformly bounded by $M = \max(M_1, M_2)$ independent of x, t. Together with the smoothness of the integrand, uniform convergence is obtained using Theorem 1. We skip the calculation for I_2 as it follows the calculation for I_1. □

Proof of Theorem 5. First, we prove the uniform convergence for the integral along $\mathcal{C}^B_{0,a}$. Introduce the change of variables $k = La + ix/2t$.

$$\begin{aligned} B_0|_{\mathcal{C}^B_{0,a}} =& \frac{1}{2\pi} \int_{\mathcal{C}^B_{0,a}} e^{ikx-k^2t} 2k\tilde{g}_0(k^2, t)dk \\ =& \frac{Le^{-x^2/2t}}{2\pi} \int_{-1}^{1} e^{iLax-(La+ix/2t)^2t} 2(La + ix/2t)\tilde{g}_0((La + ix/2t)^2, t)da \\ =& \frac{Le^{-x^2/4t}}{\pi} \int_{-1}^{1} e^{-L^2ta^2} (La + ix/2t) \int_0^t e^{(La+ix/2t)^2s} g(s)dsda. \end{aligned}$$

Using Theorem 1, uniform convergence requires the boundedness of the second derivative of the integrand

$$B_a = \sup_{a\in[0,1]} \frac{Le^{-x^2/4t}}{\pi} \left|\partial_a^2 e^{-L^2ta^2} (La + ix/2t) \int_0^t e^{(La+ix/2t)^2s-\gamma s} g(s)e^{\gamma s}ds\right| \le M,$$

for all $(x, t) \in \Omega_c$. Since $\|ge^{\gamma(\cdot)}\|_\infty < \infty$, after a lengthy computation,

$$B_a \le \sup_{a\in[0,1]} \frac{\|ge^{\gamma(\cdot)}\|_\infty}{\left|-4a^2t^2 + 4\gamma t^2 - 4iatx + x^2\right|^3} \left(e^{-a^2t-x^2/4t} P_1 + e^{-\gamma t-x^2/2t} P_2\right),$$

where P_1, P_2 are polynomials in x, t and a, with positive coefficients, and the growth for large x, t is controlled by the exponential and the denominator in front of P_1, P_2. As a result $B_a \leq M$ and the integral on $\mathcal{C}^B_{0,a}$ is computed with uniform accuracy.

Lastly, we show the uniform convergence for the integral along the oblique segment $\mathcal{C}^B_{0,b}$. The proof for the integral along $\mathcal{C}^B_{0,c}$ follows directly by symmetry. We introduce the change of variables $k = L + ix/2t + L_2(1+i)a$. The integral with $a > 1$ is separated,

$$\begin{aligned} B_0|_{\mathcal{C}^B_{0,b}} =& \frac{L_2(1+i)}{\pi}\left(\int_0^1 + \int_1^\infty\right) e^{ikx-k^2t} k\tilde{g}_0(k^2,t)\Big|_{k=L+ix/2t+L_2(1+i)a} da \\ =& B_0^\epsilon|_{\mathcal{C}^B_{0,b}} + \frac{L_2(1+i)}{\pi}\int_1^\infty e^{ikx-k^2t} k\tilde{g}_0(k^2,t)\Big|_{k=L+ix/2t+L_2(1+i)a} da. \end{aligned}$$

The second integral is dropped and the induced truncation error is bounded by

$$\begin{aligned} \left|B_0|_{\mathcal{C}^B_{0,b}} - B_0^\epsilon|_{\mathcal{C}^B_{0,b}}\right| \leq& \frac{L_2 e^{-L^2t-x^2/(4t)}}{\pi}\int_1^\infty \left|e^{-2LL_2ta}(Lt + L_2ta + \frac{x}{2t})\tilde{g}_0((L+ix/2t+L_2(1+i)a)^2,t)\right| da \\ \leq& \frac{L_2 e^{-x^2/(4t)}\|g_0 e^{\gamma(\cdot)}\|_\infty}{\pi}\int_1^\infty \left|\left(Lt + L_2ta + \frac{x}{2t}\right)\frac{\left(e^{-L_2xa-x^2/(4t)-\gamma t} - e^{-L^2t-2LL_2ta}\right)}{(L-x/(2t))(2aL_2+L+x/(2t)) - \gamma}\right| da \\ \leq& e^{-x^2/(4t)}\|g_0 e^{\gamma(\cdot)}\|_\infty \left(e^{-L_2x-\gamma t}P_3 + e^{-L^2t-2LL_2t}P_4\right), \end{aligned}$$

where P_3, P_4 are polynomials of x, t with positive coefficients. Since the decaying exponentials dominate the growth of the polynomial, the truncation error is $\mathcal{O}(\epsilon)$, uniformly in $(x,t) \in \Omega_c$ with $e^{-L_2x} = \epsilon$ and $e^{-L^2t} = \epsilon$. Using Theorem 1, uniform convergence requires the boundedness of the second derivative of the integrand

$$B_b = \sup_{a\in[0,1]} \frac{L_2 e^{i\pi/4}}{2\pi}\left|\partial_a^2\left(e^{ikx-k^2t}2k\tilde{g}_0(k^2,t)\Big|_{k=L+ix/2t+L_2e^{i\pi/4}a}\right)\right| \leq M_b,$$

for all x, t. After computing the derivatives,

$$B_b \leq \sup_{a\in[0,1]} \frac{\|g_0 e^{\gamma(\cdot)}\|_\infty}{|4\gamma t^2 - (2Lt + (2+2i)aL_2t + ix)^2|^3}\left(e^{-L^2t-2aLL_2t-x^2/(4t)}P_5 + e^{-\gamma t - aL_2x - x^2/(2t)}P_6\right),$$

where P_5, P_6 are polynomials of x, t, a with positive coefficients. The poles are removable since the integrand is analytic in k. In this case, the exponentials dominate the growth of the polynomial. Hence, $B_b \leq M$. The second derivative of the integrand of (A.1) is uniformly

bounded by M, independent of x, t. Together with the smoothness of the integrand, uniform convergence is obtained using Theorem 1.

□